


5-2019

Self-Assembled Nanoantenna Enhance Optical Activity and Transport in Scalable Thin Films and Interfaces

Keith Richard Berry Jr.
University of Arkansas, Fayetteville

Follow this and additional works at: <https://scholarworks.uark.edu/etd>

 Part of the [Biochemical and Biomolecular Engineering Commons](#), [Bioresource and Agricultural Engineering Commons](#), [Nanoscience and Nanotechnology Commons](#), [Polymer Science Commons](#), and the [Thermodynamics Commons](#)

Recommended Citation

Berry, Keith Richard Jr., "Self-Assembled Nanoantenna Enhance Optical Activity and Transport in Scalable Thin Films and Interfaces" (2019). *Theses and Dissertations*. 3208.
<https://scholarworks.uark.edu/etd/3208>

This Dissertation is brought to you for free and open access by ScholarWorks@UARK. It has been accepted for inclusion in Theses and Dissertations by an authorized administrator of ScholarWorks@UARK. For more information, please contact ccmiddle@uark.edu.

Self-Assembled Nanoantenna Enhance Optical
Activity and Transport in Scalable Thin Films and Interfaces

A dissertation submitted in partial fulfillment
of the requirements for the degree of
Doctor of Philosophy in Chemical Engineering

by

Keith R. Berry Jr
University of Arkansas
Bachelor of Science in Chemical Engineering, 2014

May 2019
University of Arkansas

This dissertation is approved for recommendation to the Graduate Council.

D. Keith Roper, Ph.D.
Dissertation Director

David M. Ford, Ph.D.
Committee Member

David Huitink, Ph.D.
Committee Member

Robert H. Coridan, Ph.D.
Committee Member

Jerry A. Havens, Ph.D.
Committee Member

ABSTRACT

Continued population growth and the decrease of existing energy platforms demands long-term solutions for development and implementation of scalable plasmonic metamaterials for energy and agricultural applications. Self-assembled nanoantenna into random and ordered arrangements are advanced herein for optical and thermal enhancements in scalable thin film. An analytical approach to estimating the thermal dynamics of random arrangements of nanoantenna resulted in estimates within 30% across a range of geometric parameters, nanoantenna-containing media, and thermal parameters. Multimodal thermal dynamics of polymer thin films containing gold nanoparticles (AuNPs) were observed through the natural log of the dimensionless temperature driving force plotted versus time and were observed and studied across a range of variables including film thickness, laser power, nanoparticle diameter, respective pixel location, and laser spot size. Large area arrays of nanoantenna were fabricated through a modified directed self-assembly process, which resulted in >2 mm x 2 mm areas with $\sim 100\%$ density of filled cavities containing 150 nm gold nanoparticles. Optical extinction for ordered arrangements of nanoantenna was estimated within 2% using rapid semi-analytic coupled-dipole approximation (rsa-CDA) simulations when contained within patterned PDMS and transferred onto glass substrates. Two biocompatible transfer approaches were developed and implemented to transfer ordered arrangements of nanoantenna to the surface of a leaf: laser induction and resinous adhesion. Dark-field microscopic imaging confirmed the ordering was maintained through the resinous adhesion transfer process. Further development of the fabrication of ordered nanoantenna and transfer onto leaf surfaces supports the design and implementation of crop-based sensors for real-time monitoring of vital crop data for improving crop production and health.

© 2019 by Keith R. Berry Jr.
All Rights Reserved

ACKNOWLEDGEMENTS

This work would not have been possible without the guidance, mentorship, and support I received from many people throughout my graduate career. I would first like to thank my advisor, Dr. Keith Roper, for his knowledge, guidance, and mentorship throughout this process. I would also like to thank Dr. Marty Matlock for the opportunity to participate in an REU program that introduced me to research and Dr. Roper. Without this opportunity, I may have never made the decision to attend graduate school. I also thank my committee members, Drs. David Ford, Robert Coridan, David Huitink, and Jerry Havens, for their participation and support of my work.

I have greatly benefited from interactions and collaborations with current and former graduate students: Vinith Bejugam, Roy French, Ricardo Romo, Jeremy Dunklin, Gregory Forcherio, Aaron Russell, Philip Blake, Xingfei Wei, and Aida Sheibani. I have also had the opportunity to mentor and work alongside many excellent undergraduate students: Megan Lanier, Tyler Howard, Caitlyn Chambers, Ty Austin, Alex O'Brien, Manoj Seeram, Collin Campbell, Kyle Key, Jasia Porchay, Megan Mitchell, Loc Huynh, Michelle Dopp, and Matthew Bizer. I learned a great deal from these individuals and others I have inevitably failed to mention.

I thank all of the faculty and staff in the Ralph E. Martin Department of Chemical Engineering and the Nanoscience and Engineering Departments at the University of Arkansas. I am also grateful for the support of the STEM Arkansas Space Grant Consortium, First-year Engineering Program, Nanotechnology Laboratory Class, National Science Foundation, the Center for Advanced Surface Engineering (CASE) under the National Science Foundation, the Arkansas EPSCoR Program, and Walton Family Charitable Support Foundation.

Lastly I would like to thank my family, church family, and numerous life-long friends for their support in my personal, academic, and professional development.

DEDICATION

I dedicate this dissertation to my amazing wife, Shanna. Over the past five years, she has sacrificed much in order for me to complete my degree. I would not be where I am without her and am thankful I can now support her as she pursues her dream.

TABLE OF CONTENTS

1. Introduction.....	1
1.1 Motivation.....	1
1.1.1 Scalable Plasmonic Metamaterials	1
1.1.2 Agricultural Sustainability	2
1.2 Background.....	3
1.2.1 Plasmonic Nanoantenna in Polymer Thin Films	3
1.2.2 Thermal Dynamics of Plasmonic Metamaterials.....	3
1.2.3 Coupling of Plasmonic Nanoantenna in Ordered Structures	4
1.2.4 Nanoimprinted Sensors on Biological Surfaces	5
1.3 Key Advances	6
1.4 Organization.....	6
1.5 References.....	7
2. Thermal Dynamics of Plasmonic Nanoparticle Composites.....	17
2.1 Introduction.....	18
2.2 Materials & Methods	20
2.2.1 Materials	20
2.2.2 Thermal equipment and data analysis.....	21
2.2.3 Fabrication of AuNP-containing samples	22
2.2.4 Dissipation rates and dynamic thermal response	26
2.3 Results & Discussion	28
2.3.1 Overall thermal dissipation rate and dynamic thermal response	28
2.3.2 Dynamic thermal responses of AuNP-containing samples.....	29

2.3.3 Thermal dissipation rates of AuNP-containing samples.....	31
2.3.4 Measured vs. estimated total dissipation rates of AuNP-containing samples	33
2.3.5 A new analytic heuristic for thermal dissipation rates from AuNP-containing samples.....	35
2.4 Conclusions.....	35
2.5 Author Information	36
2.6 Acknowledgements.....	37
2.7 References.....	37
3. Dynamic and Equilibrium Thermal Dynamic Modes Amplify Thermal Dissipation in Gold Nanoparticle-Polydimethylsiloxane Thin Films	43
3.1 Introduction.....	44
3.2 Materials and Methods.....	46
3.2.1 Film Fabrication and AuNP Addition.....	46
3.2.2 Optical Analysis.....	47
3.2.3 Thermal Characterization.....	47
3.2.4 Numerical Methods for Quantitative & Qualitative Analysis.	48
3.3 Results and Discussion.	50
3.3.1 Presence of Amplified Thermal Dissipation.....	50
3.3.2 Dynamic and Equilibrium Thermal Dynamic Modes.....	52
3.3.3 Amplified Thermal Excitation.	60
3.4 Conclusions.....	63
3.5 Author Information	63
3.6 Acknowledgements.....	64

3.7 References.....	65
4. Controlled Gold Nanoparticle Placement into Patterned Polydimethylsiloxane Thin Films via Directed Self-Assembly	68
4.1 Introduction.....	69
4.2 Materials and Methods.....	71
4.2.1 Fabrication of 2-D array stamps.	71
4.2.2 Solution Preparation.....	72
4.2.3 Stage Preparation.	72
4.2.4 Gold Nanoparticle Deposition.	74
4.2.5 Optical Characterization.	74
4.2.6 Rapid Semi-Analytical Coupled Dipole Approximation (rsa-CDA) Simulations.....	75
4.2.7 Discrete Dipole Approximation (DDA) and CDA Simulations.	75
4.2.8 Extinction per NP Calculations.....	76
4.3 Results and Discussion	76
4.3.1 Current Self-Assembly Approaches.	76
4.3.2 Developing Uniform, Large Area AuNP Ordered Arrays.	80
4.3.3 Optical Properties of AuNP Ordered Arrays.	83
4.3.4 Experimental vs. Simulated Optical Properties.	86
4.4 Conclusions.....	88
4.5 Author Information	89
4.6 Acknowledgements.....	89
4.7 References.....	90

5. Transfer Printing Ordered Gold Nanoparticles onto a Leaf Surface via Laser

Induction and Resinous Adhesion	94
5.1. Introduction.....	95
5.2. Materials and Methods.....	97
5.2.1 Fabrication of AuNP Array.....	97
5.2.2 Nanoparticle Printing via Laser Induction with and without Cyanoacrylate.....	98
5.2.3 Nanoparticle Printing via Resinous Adhesion	100
5.3. Results and Discussion	101
5.3.1 Comparison of Nanoparticle Printing with Arrayed NP Transfer	101
5.3.2 Apocynum cannabinum Leaf Properties.....	105
5.3.3 Chemical and Biochemical Contributors to NP Transfer	106
5.3.4 AuNPs Transfer to Apocynum cannabinum Leaf Surface	109
5.4. Conclusions.....	114
5.5 Author Information	115
5.6 Acknowledgements.....	115
5.7 References.....	116
6. Conclusions.....	120
6.1 Summary.....	120
6.2 Future Work.....	121
6.3 References.....	122

LIST OF PUBLISHED PAPERS

Chapter 2:

Berry Jr, K. R., Dunklin, J. R., Blake, P. A. & Roper, D. K. Thermal dynamics of plasmonic nanoparticle composites. *J. Phys. Chem. C* **119**, (2015). (*published*)

Chapter 3:

Berry Jr, K. R., Howard, T. V., & Roper, D. K. Dynamic and Equilibrium Thermal Dynamic Modes Amplify Thermal Dissipation in Gold Nanoparticle-Polydimethylsiloxane Thin Films. *J. Therm. Anal. Calorim.* (*to be submitted*).

Chapter 4:

Berry Jr, K. R., Romo, R. L., Mitchell, M., Bejugam, V. & Roper, D. K. Controlled Gold Nanoparticle Placement into Patterned Polydimethylsiloxane Thin Films via Directed Self-Assembly. *J. Nanomaterials* (*submitted*).

Chapter 5:

Berry Jr, K. R., Dopp, M. A. & Roper, D. K. Transfer Printing Ordered Gold Nanoparticles onto a Leaf Surface via Laser Induction and Resinous Adhesion. *ACS Omega* (*submitted*).

LIST OF FIGURES

Figure 2.1 Dynamic thermal response, UD/kWL , estimated using Equation (6) for AuNP-containing composites made primarily of PDMS (Sample 1, circles) or silica (Sample 2, squares; Sample 3, triangles; and Sample 4, diamonds). Dynamic thermal response is plotted vs. internal dissipation rate.	30
Figure 2.2 Measured (filled symbols) and estimated (open symbols) values of total dissipation rate for: PDMS film embedded with uniform 16-nm AuNP (Sample 1o; red circle) or heterogeneous reduced AuNP (Sample 1r; black circle); SiO ₂ capillaries of short (Sample 2, squares) or long (Sample 3, triangles) dimensions on whose inner surfaces AuNP were annealed, either empty (2a, light green square; 3a, black triangle) or filled with water (2w, dark green square; 3w blue triangle); and SiO ₂ capillaries filled aqueous AuNP suspension (Sample 4; orange diamonds).	32
Figure 3.1. Images of the PDMS films containing 16 nm AuNPs showing corresponding concentrations and thicknesses.	46
Figure 3.2. Optical setup of laser irradiation system with 532 nm light source. Laser light passed through a manual shutter and 10° ground glass diffuser to ensure a gaussian beam profile. New beam profile was then focused to an approximate 1.2 mm focal point 10 mm away from the last lens. Resulting thermal response from AuNP-PDMS films were captured via infrared (IR) camera.	47
Figure 3.3. Qualitative observation of amplified heat transfer, as shown through the ΔT one second before and after shutoff shown in (a) and the spatial gradient of the change of temperature from (a) shown in (b).	51
Figure 3.4. Rate of change of $\ln(\theta)$ according to time ($\Delta \ln(\theta)/\Delta t$), with slopes taken at 0-3 s (dynamic thermal mode) and 15-40 s (equilibrium thermal mode). (a) $\ln(\theta)$ versus time with slopes (black lines) plotted below quantitatively showing amplified temperature change. (b) $\Delta \ln(\theta)/\Delta t$ inside the heat spot for 0-3 and 15-40 s plotted against concentration for 16 nm AuNPs at 13.5 mW (red) and 25 mW (blue), and 76 nm AuNP for dynamic and equilibrium thermal modes. (c) $\Delta \ln(\theta)/\Delta t$ for pixels adjacent to the heat spot. (d) $\Delta \ln(\theta)/\Delta t$ for pixel outside the heat spot.	54
Figure 3.5. $\ln(\theta)$ graphed against time for pixels that were chosen in a controlled manner (a) against pixels chosen randomly (b). Triangle in each figure show divergence or separation in concentration highlighting importance of pixel selection when evaluating thermal effects in nanocomposite samples. (a) $\ln(\theta)$ versus time for controlled adjacent pixels and (b) $\ln(\theta)$ versus time for randomly selected.	57
Figure 3.6. $\Delta \ln(\theta)/\Delta t$ for films that have a similar thickness for different concentrations, powers, and AuNP size. (a) Slopes given at 0-3 and 15-40 s with films that are approximately 1.05 mm. Pixels measured away from the heat spot are lighter in color. (b) $\Delta \ln(\theta)/\Delta t$ for films of similar thickness (1.40 mm), power (25 mW), and concentration (0.0075%) according to time of 0-3 and 15-40 s.	58

Figure 3.7. $\Delta \ln(\theta)/\Delta t$ for 16 nm AuNP films of varying thickness and concentration. Thicknesses range from 0.93 to 1.45 mm with concentrations varying from 0.001% to 0.015%.	60
Figure 3.8. Comparison of measured against theoretically back calculated temperatures for analyzed pixels. (a) Temperature curve against time with measured temperature (red) and theoretical (green) with inset of $\ln(\theta)$ graph demonstrating calculation of theoretical value. Percent difference of theoretical and measured temperature values shown with increasing concentrations for 16 nm AuNP films at 13.5 mW (b), 16 nm AuNP at 25 mW (c), and 76 nm AuNP at 25 mW (d).	62
Figure 4.1 Schematic of directed self-assembly stage setup used for (a) high evaporation and (b) low evaporation experiments. (c) Shows the location on the syringe pump where the cage is attached. (d) Shows an example of a drop of AuNPs pinned by the fixed superstrate at the beginning of a high evaporation self-assembly experiment. (e) Shows the superstrate used for the low evaporation self-assembly experiments.	73
Figure 4.2 Controlled deposition via NP diameter, deposition rate, and evaporation rate resulted in uniform, large-area (>2 mm x 2 mm) arrays of ~100% ordering. As the evaporation and deposition rates decreased and NP size increased, the uniformity, density, and ordering improved as shown in 100x images (scale bar: 30 μm) and 20x insets (scale bar: 1000 μm).	82
Figure 4.3 Extinction spectra for the six arrays shown in Figure 1 normalizing the valley before the SLR peak to 0.01 A.U. Colored triangles represent the peak locations for both LSPR and SLR features in spectra.	84
Figure 4.4 Extinction per NP calculations for measured (filled triangles with colors corresponding to spectra in Figure 2) and simulated (hollow symbols) data of 100 and 150 nm AuNP ordered arrays.	86
Figure 4.5 Measured extinction and rsa-CDA simulated extinction efficiency for an ordered array of 150 nm AuNPs in PDMS and transferred to glass.	88
Figure 5.1 Two processes to transfer arrayed nanoparticles onto a leaf surface: (i) laser induction and (ii) resinous adhesion. Laser induction was conducted with and without cyanoacrylate.	98
Figure 5.2 Citrate-coated AuNPs dispersed in Triton X-100 exhibited FTIR spectra indicating the hydrophobic alkyl arm of the Triton X-100 approaches the Au surface while the hydrophilic poly(ethylene) glycol arm interspersed in the citrate coat.	106
Figure 5.3 AuNPs transferred onto the surfaces of an Apocynum cannabinum leaf via (1) laser induction without cyanoacrylate (a-c, scale bars: 3, 3, and 100 μm , respectively) and with cyanoacrylate (d-e, scale bars: 3 μm and 2.5 mm, respectively); and (2) resinous adhesion (f, scale bar: 3 μm). Panel (b) shows sparsely ordered AuNPs on and within the stomata; (d) shows a small area of ordered AuNPs next to a cyanoacrylate cluster; and (e) shows the discoloration of the leaf after the cyanoacrylate-assisted laser induction transfer.	109

Figure 5.4 Spectral characterization of ordered arrays in PDMS (blue line), transferred on glass with laser (green line), transferred on glass with Shellac (orange line), and ordered Shellac transferred on glass (gray line). 100x dark-field microscope images corresponding to the spectra are shown to the right of the plot (scale bar: 3 μm)..... 113

LIST OF TABLES

Table 2.1. Composition, geometry, arrangement, measured overall thermal equilibration time, and irradiation parameters for four AuNP nanocomposite samples.	22
Table 4.1 Characteristics and outcomes of current self-assembly processes compared with the self-assembly process introduced in this work.	79
Table 5.1 Characteristics and outcomes of nanoparticle printing compared with the nanoparticle array transfer methods introduced in this work.	104
Table 5.2 Primary constituents of cutin and epicuticular wax on a leaf surface, superglue, citrate capping agent, surfactant, and shellac that facilitate adhesion of AuNPs to a leaf surface.	107

NOMENCLATURE

AFN	Aerodynamically Focused Nanoparticle
AuNP	Gold Nanoparticle
Au-PDMS	Gold Nanoparticle-Polydimethylsiloxane
Au-WS ₂	Gold Decorated Tungsten Disulfide
Au-WS ₂ -PDMS	Gold Decorated Tungsten Disulfide-Polydimethylsiloxane
CDA	Coupled-Dipole Approximation
CLR	Coupled Lattice Resonance
DDA	Discrete Dipole Approximation
DPN	Dip-Pen Nanolithography
EBL	Electron Beam Lithography
EM	Electromagnetic
FEA	Finite Element Analysis
FDTD	Finite Difference Time Domain
HER	Hydrogen Evolution Reaction
IPA	Isopropanol
IR	Infrared
LSPR	Localized Surface Plasmon Resonance
MEMS	Microelectromechanical Systems
MoS ₂	Molybdenum Disulfide
NTP	Nanotribological Printing
PDMS	Polydimethylsiloxane
PL	Photoluminescence

PLD	Pulsed Laser Deposition
rAuNP	Reduced Gold Nanoparticle
ROI	Region of Interest
RI	Refractive Index
rsa-CDA	Rapid Semi-Analytic Coupled-Dipole Approximation
r_{w-s}	Wigner-Seitz Radius
SEM	Scanning Electron Microscopy
SLR	Surface Lattice Resonance
ΔT	Temperature Change
TCA	Gold (III) Chloride
TMD	Transition Metal Dichalcogenides
UV-vis	Ultraviolet-visible
WS ₂	Tungsten Disulfide
1D	One-dimensional
2D	Two-dimensional
3D	Three-dimensional

1. INTRODUCTION

1.1 Motivation

1.1.1 Scalable Plasmonic Metamaterials

Scalable processes for fabricating materials that take advantage of interactions with light to produce optical and thermal energy enhancements remain a necessary focus as the human population continues to increase and the existing energy platforms decrease. In particular, transparent dielectric materials containing embedded plasmonic nanoantennas, i.e. nanoparticles (NPs) or nanomaterials that can propagate, receive, and/or transmit electromagnetic waves, are of increasing interest for electronics, catalysis, water desalination, and medical applications due to the ability to utilize the electromagnetically-active NPs to produce enhancements in energy and mass transport systems.¹⁻¹⁷ Metallic nanoantennas, for instance, exhibit localized surface plasmon resonances (LSPR) when exposed to an external electromagnetic (EM) field such as incident light at the metals resonant frequency.¹⁸⁻²⁰ Random dispersions of these metallic nanoantennas assembled in polymer thin films produce significant thermal property and efficiency enhancements compared to bare polymer thin films.²¹⁻²⁹ Additional optical and efficiency enhancements are observed when these metallic nanoantennas are assembled into organized structures, e.g. ordered arrays, through the LSPRs of each individual particle coupling with the light diffracted from the ordered arrangement resulting in a surface lattice resonance (SLR), i.e. Fano resonance or coupled lattice resonance (CLR).^{20,30-36} These additional optical and efficiency enhancements appear as a secondary feature within the extinction spectra and can be tuned by varying the lattice spacing, nanoantenna geometry, nanoantenna material, incident EM field intensity, and the refractive index (RI).^{34,35,37-42} This work focuses on scalable fabrication techniques for producing polymer thin films with gold (Au) NPs self-assembled into random and ordered arrangements and showing the

optical and thermal enhancements of randomly assembled AuNPs and optical enhancements of AuNPs self-assembled into ordered square lattices.

1.1.2 Agricultural Sustainability

Real-time monitoring of vital crop information (i.e. photosynthetic properties, nutrient intake, and responses to pesticides) are of increasing importance for further agricultural development to meet higher sustainable food source demands due to rising human populations. Existing sensors based on surface plasmon resonance, enzyme interaction, spectral activity, and transducing electric field effect allow for non-invasive monitoring but are limited by sensitivity, specificity, throughput, stability, and portability.⁴³ The development of a facile and biocompatible sensor, e.g. a two dimensional (2D) ordered nanoantenna array, would provide critical insight for maintaining the agricultural requirements as well as overcome the limitations of existing sensor technology through selective, energetic near-field responses with adaptive far-field signals.⁴⁴ Recent advances in sensor technology, i.e. flexible electronics and wearable sensors, have been developed for real-time monitoring of health applications with few also being used to monitor basic plant responses.^{45–54} Many of the advances in flexible electronics and wearable sensors has predominantly relied on advances in techniques for printing nanomaterial structures where the nanomaterial is either directly printed on a surface or transferred from one surface to another.^{45–47} Existing printing methods include electron beam lithography (EBL), nanotribological printing (NTP), aerodynamically focused nanoparticle (AFN) printing, dip-pen nanolithography (DPN), tape nanolithography, direct laser writing, microcontact printing, and stamp-assisted printing.^{48,49,52,53,55–62} Extreme conditions, e.g. high temperature, high vacuum, strong solvents, and strong adhesives, limit implementation of these approaches for sustainable agricultural

applications. This work also introduces two novel printing methods for transferring ordered arrays of AuNPs onto the surface of a leaf: (1) laser induction and (2) resinous adhesion.

1.2 Background

1.2.1 Plasmonic Nanoantenna in Polymer Thin Films

Fabrication methods ranging from *in situ* reduction,^{15,23,63} direct dispersion of preformed nanoantenna,^{63,64} self-assembly,^{61,65–67} lithography,^{68,69} drop-casting,^{70,71} sol-gel,^{72–74} pulsed laser deposition (PLD),^{75,76} and electroless plating and thermal annealing^{28,77–80} have been employed to produce nanocomposite media. These nanofabrication processes enable rapid and cost-effective nanocomposite fabrication by adjustments to material properties for two- (2D) and three-dimensional (3D) nanostructure creation. The addition of various types of nanoantennas, e.g. metallic,^{63,81–85} magnetic,^{86–90} and semiconductor,^{91–93} into polydimethylsiloxane (PDMS) films using direct dispersion, *in situ* reduction, and self-assembly methods has increased in order to fully characterize the nanoantenna properties without significant impact from the substrate through the use of optically and thermally inert polymers like PDMS. Plasmonic nanoantennas embedded in polymer thin films have continued to increase for applications like biomedical sensors, microelectromechanical systems (MEMS), catalysis, and thermal therapeutics.

1.2.2 Thermal Dynamics of Plasmonic Metamaterials

Various methods for optothermal modeling of equilibrium and dynamic temperatures and fluxes in plasmon-heated materials and systems have been explored. Such models range from one-dimensional (1-D) analytical to 3-D computational methods.^{14,94–96} Thermal dynamics in continuous media heated by conventional bulk or resistive sources differ from those in resonantly

induced nanocomposites. In conventional heaters, thermal sources drive heat flux in a direction opposite to a developing temperature gradient while 3-D distributions of plasmonic nanoantennas in a host dielectric originate heat at point sources.⁹⁷ This heat origination at point sources can improve its dissipation relative to surface or linear sources. Finite element analysis (FEA) via COMSOL has been used to show thermoplasmonic Mie absorption, Fourier heat conduction, Rayleigh convection, and Stefan-Boltzmann radiation relations can accurately estimate thermoplasmonic dissipation.⁸² An analytical model that extends previously reported thermal parameters and heat transfer equations and factors in film geometry and nanoantenna content was developed to estimate the thermal dissipation rates and overall thermal dynamics of Au-PDMS films with a range of AuNP concentrations and film thicknesses.⁹⁸ Understanding the thermal dynamics of plasmonic nanoantenna could yield fruitful advances in developing devices for a range of applications including energetics, photovoltaics, tumor ablation, and thermal therapies.

1.2.3 Coupling of Plasmonic Nanoantenna in Ordered Structures

Nanoantenna exhibit LSPR through conduction-electron oscillations when an external EM field is applied and can be coupled through the LSPR of individual particles when the nanoantenna are assembled in ordered square lattices resulting in SLR enhancements across a broader portion of the visible spectrum.^{18–20,30–36} SLR features exhibit tunability via lattice spacing, nanoantenna geometry, incident EM field intensity, and the RI for varying optical, thermal, and electronic applications.^{34,35,37–42} Simulations of extinction spectra of metallic nanoantenna containing LSPR and/or SLR spectral features, e.g. plasmon hybridization, coupled dipole approximation (CDA), rapid semi-analytic CDA (rsa-CDA), finite-difference time-domain (FDTD), and Fano theory, have been shown to closely estimate both features compared to measured extinction

spectra.^{31,33,36,99–101} The coupling of plasmonic nanoantennas in ordered structures present viable opportunities for developing unique devices that utilize the optical and thermal enhancements for energy related applications.

1.2.4 Nanoimprinted Sensors on Biological Surfaces

Many types of sensors have been developed and transferred to biological surfaces like that of human skin or plant leaves for applications ranging from real-time health monitoring of biometrics, muscular stress and strain, and exposure to ultraviolet (UV) radiation to real-time monitoring of nutrient uptake, utilization and efficiency of a plant or row crop.^{46,48,49,102} Methods such as EBL, AFN, NTP, and DPN have been used to develop nanomaterials that could be transferred onto different substrates but require high temperature, high vacuum, and strong solvents, which are incompatible with sensitive biological surfaces like that of a leaf.^{55–59} Recent advances in printing techniques have produced possible options like tape nanolithography, direct laser writing, microcontact printing, and stamp-assisted printing.^{52,53,60–62} Tape nanolithography offers the most biocompatible option of the recent advances because the desired nanomaterial is deposited on a donor substrate and subsequently removed via direct taping and peeling leaving the patterned nanomaterial directly on the tape.^{52,53} This patterned nanomaterial-containing tape can then be transferred to biological surfaces like human skin or plant leaves and used to measure stress, strain, reflectance, transmission, and relative humidity.^{48,53}

1.3 Key Advances

The significant advances made in this work are:

1. Developed analytical approach to estimating the thermal dynamics of random arrangements of AuNPs within different media.
2. Characterized the multimodal thermal dynamics of random arrangements of AuNPs within polymer films across a range of different variables.
3. Developed a reproducible approach to fabricating large-area ordered arrays of AuNPs in pre-patterned PDMS films.
4. Matched measured extinction spectra peak locations for ordered arrays of AuNPs in PDMS and transferred onto glass with rsa-CDA simulations within 2%.
5. Developed a reproducible printing process to transfer ordered arrays of AuNPs onto the surface of a leaf.

1.4 Organization

Chapters 2 through 5 are publications that cover the approaches and key results pertaining to the five key advances outlined above. Chapter 2 derives and applies an analytical approach to estimating the thermal dynamics of random arrangements of AuNPs in colloidal suspensions, deposited on glass, and embedded in polymer thin films. Chapter 3 studies the multimodal thermal dynamics of AuNPs embedded in polymer thin films with respect to film thickness, laser power, NP diameter, respective pixel location, and laser spot size. Chapter 4 describes the development of a reproducible and scalable approach to fabricating large area ordered arrays of AuNPs along with the subsequent optical characterization and comparison to simulated optical properties. Chapter 5 presents two new nanoparticle printing techniques that were used to transfer ordered

arrays of AuNPs onto the surface of a leaf as a first step toward the development of a sensor for real-time monitoring of vital crop information. Each of these papers discuss fabrication and characterization methods for scalable nanocomposite media for enhancing the optical activity and transport within thin films and across various interfaces. Chapter 6 summarizes the work and outlines future research opportunities within this field of study.

1.5 References

- (1) Cho, E. S.; Coates, N. E.; Forster, J. D.; Ruminski, A. M.; Russ, B.; Sahu, A.; Su, N. C.; Yang, F.; Urban, J. J. Engineering Synergy: Energy and Mass Transport in Hybrid Nanomaterials. *Adv. Mater.* **2015**, *27* (38), 5744–5752. <https://doi.org/10.1002/adma.201500130>.
- (2) Corry, B. Designing Carbon Nanotube Membranes for Efficient Water Desalination. *J. Phys. Chem. B* **2008**. <https://doi.org/10.1021/jp709845u>.
- (3) Gensler, R.; Gröppel, P.; Muhrer, V.; Müller, N. Application of Nanoparticles in Polymers for Electronics and Electrical Engineering. In *Particle and Particle Systems Characterization*; 2002. [https://doi.org/10.1002/1521-4117\(200211\)19:5<293::AID-PPSC293>3.0.CO;2-N](https://doi.org/10.1002/1521-4117(200211)19:5<293::AID-PPSC293>3.0.CO;2-N).
- (4) Ghosh, S.; Ghosh, D.; Bag, P. K.; Bhattacharya, S. C.; Saha, A. Aqueous Synthesis of ZnTe/Dendrimer Nanocomposites and Their Antimicrobial Activity: Implications in Therapeutics. *Nanoscale* **2011**, *3* (3), 1139. <https://doi.org/10.1039/c0nr00610f>.
- (5) Goyal, R. K.; Tiwari, A.; Mulik, U.; Negi, Y. Novel High Performance Al₂O₃/Poly(Ether Ether Ketone) Nanocomposites for Electronics Applications. *Compos. Sci. Technol.* **2007**, *67* (9), 1802–1812. <https://doi.org/10.1016/j.compscitech.2006.10.020>.
- (6) Humplik, T.; Lee, J.; O'Hern, S. C.; Fellman, B. A.; Baig, M. A.; Hassan, S. F.; Atieh, M. A.; Rahman, F.; Laoui, T.; Karnik, R.; et al. Nanostructured Materials for Water Desalination. *Nanotechnology*. 2011. <https://doi.org/10.1088/0957-4484/22/29/292001>.
- (7) Karttunen, M.; Ruuskanen, P.; Pitk??nen, V.; Albers, W. M. Electrically Conductive Metal Polymer Nanocomposites for Electronics Applications. *J. Electron. Mater.* **2008**, *37* (7), 951–954. <https://doi.org/10.1007/s11664-008-0451-2>.
- (8) Kovalenko, V. V.; Rumyantseva, M. N.; Gaskov, A. M.; Makshina, E. V.; Yushchenko, V. V.; Ivanova, I. I.; Ponzoni, A.; Faglia, G.; Comini, E. SnO₂/Fe₂O₃ Nanocomposites: Ethanol-Sensing Performance and Catalytic Activity for Oxidation of Ethanol. *Inorg. Mater.* **2006**, *42* (10), 1088–1093. <https://doi.org/10.1134/S0020168506100074>.

- (9) Neoh, K. G.; Kang, E. T. Functionalization of Inorganic Nanoparticles with Polymers for Stealth Biomedical Applications. *Polym. Chem.* **2011**, *2* (4), 747–759. <https://doi.org/10.1039/C0PY00266F>.
- (10) Owens, D. E.; Eby, J. K.; Jian, Y.; Peppas, N. A. Temperature-Responsive Polymer–gold Nanocomposites as Intelligent Therapeutic Systems. *J. Biomed. Mater. Res. Part A* **2007**, *83A* (3), 692–695. <https://doi.org/10.1002/jbm.a.31284>.
- (11) Qi, X.; Tan, C.; Wei, J.; Zhang, H. Synthesis of Graphene-Conjugated Polymer Nanocomposites for Electronic Device Applications. *Nanoscale* **2013**, *5* (4), 1440–1451. <https://doi.org/10.1039/c2nr33145d>.
- (12) Sassaroli, E.; Li, K. C. P.; O’Neill, B. E. Numerical Investigation of Heating of a Gold Nanoparticle and the Surrounding Microenvironment by Nanosecond Laser Pulses for Nanomedicine Applications. *Phys. Med. Biol.* **2009**, *54* (18), 5541–5560. <https://doi.org/10.1088/0031-9155/54/18/013>.
- (13) Scott, A.; Gupta, R.; Kulkarni, G. U. A Simple Water-Based Synthesis of Au Nanoparticle/PDMS Composites for Water Purification and Targeted Drug Release. *Macromol. Chem. Phys.* **2010**, *211* (15), 1640–1647. <https://doi.org/10.1002/macp.201000079>.
- (14) Steigerwalt, E. S.; Deluga, G. A.; Lukehart, C. M. Pt-Ru/Carbon Fiber Nanocomposites: Synthesis, Characterization, and Performance as Anode Catalysts of Direct Methanol Fuel Cells. A Search for Exceptional Performance. *J. Phys. Chem. B* **2002**, *106* (4), 760–766. <https://doi.org/10.1021/jp012707t>.
- (15) Subramanian, V.; Wolf, E. E.; Kamat, P. V. Catalysis with TiO₂/Gold Nanocomposites. Effect of Metal Particle Size on the Fermi Level Equilibration. *J. Am. Chem. Soc.* **2004**, *126* (15), 4943–4950. <https://doi.org/10.1021/ja0315199>.
- (16) Volokitin, A. I.; Persson, B. N. J. Radiative Heat Transfer between Nanostructures. *Phys. Rev. B* **2001**, *63* (20), 205404. <https://doi.org/10.1103/PhysRevB.63.205404>.
- (17) Yi, D. K.; Lee, S. S.; Ying, J. Y. Synthesis and Applications of Magnetic Nanocomposite Catalysts. *Chem. Mater.* **2006**. <https://doi.org/10.1021/cm052885p>.
- (18) Amendola, V.; Pilot, R.; Frasconi, M.; Maragò, O. M.; Iatì, M. A. Surface Plasmon Resonance in Gold Nanoparticles: A Review. *J. Phys. Condens. Matter* **2017**, *29* (20). <https://doi.org/10.1088/1361-648X/aa60f3>.
- (19) Dunklin, J. R.; Bodinger, C.; Forcherio, G. T.; Roper, D. K. Plasmonic Extinction in Gold Nanoparticle-Polymer Films as Film Thickness and Nanoparticle Separation Decrease below Resonant Wavelength. *J. Nanophotonics* **2017**, *11* (1). <https://doi.org/10.1117/1.JNP.11.016002>.

- (20) Kravets, V. G.; Kabashin, A. V.; Barnes, W. L.; Grigorenko, A. N. Plasmonic Surface Lattice Resonances: A Review of Properties and Applications. *Chem. Rev.* **2018**, *118* (12), 5912–5951. <https://doi.org/10.1021/acs.chemrev.8b00243>.
- (21) Berry, K. R.; Russell, A. G.; Blake, P. T.; Roper, D. K. Gold Nanoparticles Reduced in Situ and Dispersed in Polymer Thin Films: Optical and Thermal Properties. *Nanotechnology* **2012**, *23* (37), 11. <https://doi.org/10.1088/0957-4484/23/37/375703>.
- (22) Bozlar, M.; He, D.; Bai, J.; Chalopin, Y.; Mingo, N.; Volz, S. Carbon Nanotube Microarchitectures for Enhanced Thermal Conduction at Ultralow Mass Fraction in Polymer Composites. *Adv. Mater.* **2010**, *22* (14), 1654–1658. <https://doi.org/10.1002/adma.200901955>.
- (23) Dunklin, J. R.; Forcherio, G. T.; Berry, K. R.; Roper, D. K. Asymmetric Reduction of Gold Nanoparticles into Polydimethylsiloxane Thin Films. *ACS Appl. Mater. Interfaces* **2013**, *5*, 8457–8466. <https://doi.org/10.1021/am4018785>.
- (24) Li, T.-L.; Hsu, S. L.-C. Enhanced Thermal Conductivity of Polyimide Films via a Hybrid of Micro-and Nano-Sized Boron Nitride. *J. Phys. Chem. B* **2010**, *114* (20), 6825–6829.
- (25) Lin, W.; Moon, K. S.; Wong, C. P. A Combined Process of in Situ Functionalization and Microwave Treatment to Achieve Ultrasmall Thermal Expansion of Aligned Carbon Nanotube-Polymer Nanocomposites: Toward Applications as Thermal Interface Materials. *Adv. Mater.* **2009**, *21* (23), 2421–2424. <https://doi.org/10.1002/adma.200803548>.
- (26) Urban, A. S.; Carretero-Palacios, S.; Lutich, A. A.; Lohmüller, T.; Feldmann, J.; Jäckel, F. Optical Trapping and Manipulation of Plasmonic Nanoparticles: Fundamentals, Applications, and Perspectives. *Nanoscale* **2014**, *6* (9), 4458. <https://doi.org/10.1039/c3nr06617g>.
- (27) Chen, M.; Wu, Y.; Song, W.; Mo, Y.; Lin, X.; He, Q.; Guo, B. Plasmonic Nanoparticle-Embedded Poly(p-Phenylene Benzobisoxazole) Nanofibrous Composite Films for Solar Steam Generation. *Nanoscale* **2018**, *10* (13), 6186–6193. <https://doi.org/10.1039/C8NR01017J>.
- (28) Ahn, W.; Roper, D. K. Transformed Gold Island Film Improves Light-to-Heat Transduction of Nanoparticles on Silica Capillaries. *J. Phys. Chem. C* **2008**, *112* (32), 12214–12218. <https://doi.org/10.1021/jp802497v>.
- (29) Forcherio, G. T.; Roper, D. K. Optical Attenuation of Plasmonic Nanocomposites within Photonic Devices. *Appl. Opt.* **2013**, *53* (25), 6417–6427. <https://doi.org/10.1364/AO.52.006417>.
- (30) Bejugam, V. Opto-Thermal Characterization of Plasmon and Coupled Lattice Resonances in 2-D Metamaterial Arrays. *Theses Diss.* **2018**, 2868.

- (31) DeJarnette, D.; Norman, J.; Roper, D. K. Attribution of Fano Resonant Features to Plasmonic Particle Size, Lattice Constant, and Dielectric Wavenumber in Square Nanoparticle Lattices. *Photonics Res.* **2014**. <https://doi.org/10.1364/PRJ.2.000015>.
- (32) Forcherio, G. T.; Blake, P.; Seeram, M.; DeJarnette, D.; Roper, D. K. Coupled Dipole Plasmonics of Nanoantennas in Discontinuous, Complex Dielectric Environments. *J. Quant. Spectrosc. Radiat. Transf.* **2015**. <https://doi.org/10.1016/j.jqsrt.2015.07.017>.
- (33) Francescato, Y.; Giannini, V.; Maier, S. A. Plasmonic Systems Unveiled by Fano Resonances. *ACS Nano* **2012**. <https://doi.org/10.1021/nn2050533>.
- (34) Guo, R.; Hakala, T. K.; Törmä, P. Geometry Dependence of Surface Lattice Resonances in Plasmonic Nanoparticle Arrays. *Phys. Rev. B* **2017**, *95* (15), 1–11. <https://doi.org/10.1103/PhysRevB.95.155423>.
- (35) Humphrey, A. D.; Barnes, W. L. Plasmonic Surface Lattice Resonances on Arrays of Different Lattice Symmetry. *Phys. Rev. B - Condens. Matter Mater. Phys.* **2014**, *90* (7), 1–8. <https://doi.org/10.1103/PhysRevB.90.075404>.
- (36) Väkeväinen, A. I.; Moerland, R. J.; Rekola, H. T.; Eskelinen, A. P.; Martikainen, J. P.; Kim, D. H.; Törmä, P. Plasmonic Surface Lattice Resonances at the Strong Coupling Regime. *Nano Lett.* **2014**, *14* (4), 1721–1727. <https://doi.org/10.1021/nl4035219>.
- (37) Auguie, B.; Bendaña, X. M.; Barnes, W. L.; García De Abajo, F. J. Diffractive Arrays of Gold Nanoparticles near an Interface: Critical Role of the Substrate. *Phys. Rev. B - Condens. Matter Mater. Phys.* **2010**, *82*, 155447. <https://doi.org/10.1103/PhysRevB.82.155447>.
- (38) Blake, P.; Kühne, S.; Forcherio, G. T.; Roper, D. K. Diffraction in Nanoparticle Lattices Increases Sensitivity of Localized Surface Plasmon Resonance to Refractive Index Changes. *J. Nanophotonics* **2014**, *8* (1), 083084. <https://doi.org/10.1117/1.JNP.8.083084>.
- (39) DeJarnette, D.; Jang, G. G.; Blake, P.; Roper, D. K. Polarization Angle Affects Energy of Plasmonic Features in Fano Resonant Regular Lattices. *J. Opt.* **2014**, *16* (10), 105006. <https://doi.org/10.1088/2040-8978/16/10/105006>.
- (40) Fano, U. Effects of Configuration Interaction on Intensities and Phase Shifts. *Phys. Rev.* **1961**, *124* (6), 1866–1878. <https://doi.org/10.1103/PhysRev.124.1866>.
- (41) Flidj, N.; Laurent, G.; Aubard, J.; Lvi, G.; Hohenau, A.; Krenn, J. R.; Aussenegg, F. R. Grating-Induced Plasmon Mode in Gold Nanoparticle Arrays. *J. Chem. Phys.* **2005**, *123* (22), 221103. <https://doi.org/10.1063/1.2140699>.
- (42) Forcherio, G. T.; Blake, P.; DeJarnette, D.; Roper, D. K. Nanoring Structure, Spacing, and Local Dielectric Sensitivity for Plasmonic Resonances in Fano Resonant Square Lattices. *Opt. Express* **2014**, *22* (15), 17791. <https://doi.org/10.1364/OE.22.017791>.

- (43) Roper, D. K.; Ahn, W.; Taylor, B.; D'Asen, Y. Enhanced Spectral Sensing by Electromagnetic Coupling with Localized Surface Plasmons on Subwavelength Structures. *IEEE Sens. J.* **2010**, *10* (3), 531–540.
- (44) Blake, P.; Obermann, J.; Harbin, B.; Roper, D. K. Enhanced Nanoparticle Response from Coupled Dipole Excitation for Plasmon Sensors. *IEEE Sens. J.* **2011**, *11* (12), 3332–3340. <https://doi.org/10.1109/JSEN.2011.2158417>.
- (45) Andrich, P.; Li, J.; Liu, X.; Heremans, F. J.; Nealey, P. F.; Awschalom, D. D. Microscale-Resolution Thermal Mapping Using a Flexible Platform of Patterned Quantum Sensors. *Nano Lett.* **2018**, *18* (8), 4684–4690. <https://doi.org/10.1021/acs.nanolett.8b00895>.
- (46) Ketelsen, B.; Yesilmen, M.; Schlicke, H.; Noei, H.; Su, C.-H.; Liao, Y.-C.; Vossmeier, T. Fabrication of Strain Gauges via Contact Printing : A Simple Route to Healthcare Sensors Based on Cross-Linked Gold Nanoparticles. *ACS Appl. Mater. Interfaces* **2018**, *10*, 37374–37385. <https://doi.org/10.1021/acsami.8b12057>.
- (47) Mcalpine, M. C.; Ahmad, H.; Wang, D.; Heath, J. R. Highly Ordered Nanowire Arrays on Plastic Substrates for Ultrasensitive Flexible Chemical Sensors. *Nat. Mater.* **2007**, *6* (5), 379–384. <https://doi.org/10.1038/nmat1891>.
- (48) Oren, S.; Ceylan, H.; Schnable, P. S.; Dong, L. High-Resolution Patterning and Transferring of Graphene-Based Nanomaterials onto Tape toward Roll-to-Roll Production of Tape-Based Wearable Sensors. *Adv. Mater. Technol.* **2017**, *2* (12), 1–14. <https://doi.org/10.1002/admt.201700223>.
- (49) Shi, Y.; Manco, M.; Moyal, D.; Huppert, G.; Araki, H.; Banks, A.; Joshi, H.; McKenzie, R.; Seewald, A.; Griffin, G.; et al. Soft, Stretchable, Epidermal Sensor with Integrated Electronics and Photochemistry for Measuring Personal UV Exposures. *PLoS One* **2018**, *13* (1), 1–15. <https://doi.org/10.1371/journal.pone.0190233>.
- (50) Song, E.; Lee, Y. K.; Li, R.; Li, J.; Jin, X.; Yu, K. J.; Xie, Z.; Fang, H.; Zhong, Y.; Du, H.; et al. Transferred, Ultrathin Oxide Bilayers as Biofluid Barriers for Flexible Electronic Implants. *Adv. Funct. Mater.* **2018**, *28* (12), 1–10. <https://doi.org/10.1002/adfm.201702284>.
- (51) Wang, D.; Zhang, Y.; Lu, X.; Ma, Z.; Xie, C.; Zheng, Z. Chemical Formation of Soft Metal Electrodes for Flexible and Wearable Electronics. *Chem. Soc. Rev.* **2018**, *47* (12), 4611–4641. <https://doi.org/10.1039/c7cs00192d>.
- (52) Wang, L.; Chen, P.; Wang, Y. C.; Liu, G. S.; Liu, C.; Xie, X.; Li, J. Z.; Yang, B. R. Tape-Based Photodetector: Transfer Process and Persistent Photoconductivity. *ACS Appl. Mater. Interfaces* **2018**, *10* (19), 16596–16604. <https://doi.org/10.1021/acsami.8b02233>.
- (53) Wang, Q.; Han, W.; Wang, Y.; Lu, M.; Dong, L. Tape Nanolithography: A Rapid and Simple Method for Fabricating Flexible, Wearable Nanophotonic Devices. *Microsystems Nanoeng.* **2018**, *4* (1), 31. <https://doi.org/10.1038/s41378-018-0031-4>.

- (54) Yu, K. J.; Yan, Z.; Han, M.; Rogers, J. A. Inorganic Semiconducting Materials for Flexible and Stretchable Electronics. *npj Flex. Electron.* **2017**, *1* (1), 4. [https://doi.org/10.1016/S0140-6736\(76\)90345-7](https://doi.org/10.1016/S0140-6736(76)90345-7).
- (55) Bautista, G.; Dreser, C.; Zang, X.; Kern, D. P.; Kauranen, M.; Fleischer, M. Collective Effects in Second-Harmonic Generation from Plasmonic Oligomers. *Nano Lett.* **2018**, *18* (4), 2571–2580. <https://doi.org/10.1021/acs.nanolett.8b00308>.
- (56) Dawood, F.; Wang, J.; Schulze, P. A.; Sheehan, C. J.; Buck, M. R.; Dennis, A. M.; Majumder, S.; Krishnamurthy, S.; Ticknor, M.; Staude, I.; et al. The Role of Liquid Ink Transport in the Direct Placement of Quantum Dot Emitters onto Sub-Micrometer Antennas by Dip-Pen Nanolithography. *Small* **2018**, *14* (31), 1–10. <https://doi.org/10.1002/sml.201801503>.
- (57) Khare, H. S.; Gosvami, N. N.; Lahouij, I.; Milne, Z.; McClimon, J. B.; Carpick, R. W. Nanotribological Printing: A Nanoscale Additive Manufacturing Method. *Nano Lett.* **2018**, *acs.nanolett.8b02505*. <https://doi.org/10.1021/acs.nanolett.8b02505>.
- (58) Lee, G. Y.; Park, J. II; Kim, C. S.; Yoon, H. S.; Yang, J.; Ahn, S. H. Aerodynamically Focused Nanoparticle (AFN) Printing: Novel Direct Printing Technique of Solvent-Free and Inorganic Nanoparticles. *ACS Appl. Mater. Interfaces* **2014**, *6* (19), 16466–16471. <https://doi.org/10.1021/am504304g>.
- (59) Wu, T.; Lin, Y. W. Surface-Enhanced Raman Scattering Active Gold Nanoparticle/Nanohole Arrays Fabricated through Electron Beam Lithography. *Appl. Surf. Sci.* **2018**, *435*, 1143–1149. <https://doi.org/10.1016/j.apsusc.2017.11.213>.
- (60) Bagheri, S.; Weber, K.; Gissibl, T.; Weiss, T.; Neubrech, F.; Giessen, H. Fabrication of Square-Centimeter Plasmonic Nanoantenna Arrays by Femtosecond Direct Laser Writing Lithography: Effects of Collective Excitations on SEIRA Enhancement. *ACS Photonics* **2015**, *2* (6), 779–786. <https://doi.org/10.1021/acsphotonics.5b00141>.
- (61) Cerf, A.; Vieu, C. Transfer Printing of Sub-100 Nm Nanoparticles by Soft Lithography with Solvent Mediation. *Colloids Surfaces A Physicochem. Eng. Asp.* **2009**, *342* (1–3), 136–140. <https://doi.org/10.1016/j.colsurfa.2009.04.019>.
- (62) Chen, Y.; Li, X.; Bi, Z.; Li, G.; He, X.; Gao, X. Stamp-Assisted Printing of Nanotextured Electrodes for High-Performance Flexible Planar Micro-Supercapacitors. *Chem. Eng. J.* **2018**, *353* (July), 499–506. <https://doi.org/10.1016/j.cej.2018.07.158>.
- (63) Berry Jr, K. R.; Russell, A. G.; Blake, P. A.; Keith Roper, D. Gold Nanoparticles Reduced *in Situ* and Dispersed in Polymer Thin Films: Optical and Thermal Properties. *Nanotechnology* **2012**, *23* (37), 375703. <https://doi.org/10.1088/0957-4484/23/37/375703>.
- (64) Kosuga, A.; Yamamoto, Y.; Miyai, M.; Matsuzawa, M. A High Performance Photothermal Film with Spherical Shell-Type Metallic Nanocomposites for Solar Thermoelectric Conversion. *Nanoscale* **2015**, *7* (17), 1–2. <https://doi.org/10.1039/c5nr00943j>.

- (65) Liu, S.; Zhu, T.; Hu, R.; Liu, Z. Evaporation-Induced Self-Assembly of Gold Nanoparticles into a Highly Organized Two-Dimensional Array. *Phys. Chem. Chem. Phys.* **2002**, *4* (24), 6059–6062. <https://doi.org/10.1039/b208520h>.
- (66) McMillan, R. A.; Paavola, C. D.; Howard, J.; Chan, S. L.; Zaluzec, N. J.; Trent, J. D. Ordered Nanoparticle Arrays Formed on Engineered Chaperonin Protein Templates. *Nat. Mater.* **2002**, *1* (4), 247–252. <https://doi.org/10.1038/nmat775>.
- (67) Li, Y. J.; Huang, W. J.; Sun, S. G. A Universal Approach for the Self-Assembly of Hydrophilic Nanoparticles into Ordered Monolayer Films at a Toluene/Water Interface. *Angew. Chemie - Int. Ed.* **2006**, *45* (16), 2537–2539. <https://doi.org/10.1002/anie.200504595>.
- (68) Barcelo, S. J.; Lam, S.-T.; Gibson, G. A.; Sheng, X.; Henze, D. Nanosphere Lithography Based Technique for Fabrication of Large Area Well Ordered Metal Particle Arrays. **2012**, 83232L–83232L–7. <https://doi.org/10.1117/12.916600>.
- (69) Hung, A. M.; Micheel, C. M.; Bozano, L. D.; Osterbur, L. W.; Wallraff, G. M.; Cha, J. N. Large-Area Spatially Ordered Arrays of Gold Nanoparticles Directed by Lithographically Confined DNA Origami. *Nat. Nanotechnol.* **2010**, *5* (2), 121–126. <https://doi.org/10.1038/nnano.2009.450>.
- (70) Eslamian, M.; Zabihi, F. Ultrasonic Substrate Vibration-Assisted Drop Casting (SVADC) for the Fabrication of Photovoltaic Solar Cell Arrays and Thin-Film Devices. *Nanoscale Res. Lett.* **2015**, *10* (1), 1–5. <https://doi.org/10.1186/s11671-015-1168-9>.
- (71) Liu, Y.; Zhao, X.; Cai, B.; Pei, T.; Tong, Y.; Tang, Q.; Liu, Y. Controllable Fabrication of Oriented Micro/Nanowire Arrays of Dibenzo-Tetrathiafulvalene by a Multiple Drop-Casting Method. *Nanoscale* **2014**, *6* (3), 1323–1328. <https://doi.org/10.1039/C3NR05680E>.
- (72) Mo, C. B.; Cha, S. I.; Kim, K. T.; Lee, K. H.; Hong, S. H. Fabrication of Carbon Nanotube Reinforced Alumina Matrix Nanocomposite by Sol-Gel Process. *Mater. Sci. Eng. A* **2005**, *395* (1–2), 124–128. <https://doi.org/10.1016/j.msea.2004.12.031>.
- (73) Pan, J.; Zhang, H.; Chen, W.; Pan, M. Nafion-Zirconia Nanocomposite Membranes Formed via in Situ Sol-Gel Process. *Int. J. Hydrogen Energy* **2010**, *35* (7), 2796–2801. <https://doi.org/10.1016/j.ijhydene.2009.05.110>.
- (74) Ma, J.-Z.; Hu, J.; Zhang, Z.-J. Polyacrylate/Silica Nanocomposite Materials Prepared by Sol-gel Process. *Eur. Polym. J.* **2007**, *43* (10), 4169–4177. <https://doi.org/10.1016/j.eurpolymj.2007.06.051>.
- (75) Matsubara, M.; Azuma, H.; Asahi, R. Fabrication of Nanocomposite Thermoelectric Materials by a Pulsed Laser Deposition Method. In *Journal of Electronic Materials*; 2011; Vol. 40, pp 1176–1180. <https://doi.org/10.1007/s11664-011-1575-3>.

- (76) Kim, D. H.; Sun, X.; Kim, T. C.; Eun, Y. J.; Lee, T.; Jeong, S. G.; Ross, C. a. Magnetic Phase Formation in Self-Assembled Epitaxial BiFeO₃-MgO and BiFeO₃-MgAl₂O₄ Nanocomposite Films Grown by Combinatorial Pulsed Laser Deposition. *ACS Appl. Mater. Interfaces* **2016**, *8* (4), 2673–2679. <https://doi.org/10.1021/acsami.5b10676>.
- (77) Russell, A. G.; McKnight, M. D.; Sharp, A. C.; Hestekin, J. A.; Roper, D. K. Gold Nanoparticles Allow Optoplasmonic Evaporation from Open Silica Cells with a Logarithmic Approach to Steady-State Thermal Profiles. *J. Phys. Chem. C* **2010**, *114* (22), 10132–10139. <https://doi.org/10.1021/jp101762n>.
- (78) Russell, A. G.; McKnight, M. D.; Hestekin, J. A.; Roper, D. K. Thermodynamics of Optoplasmonic Heating in Fluid-Filled Gold-Nanoparticle-Plated Capillaries. *Langmuir* **2011**, *27* (12), 7799–7805. <https://doi.org/10.1021/la200078j>.
- (79) Lisunova, M.; Wei, X.; DeJarnette, D.; Forcherio, G. T.; Berry, K. R.; Blake, P.; Roper, D. K. Photothermal Response of the Plasmonic Nanoconglomerates in Films Assembled by Electroless Plating. *RSC Adv.* **2014**, *4* (40), 20894–20901. <https://doi.org/10.1039/C4RA03351E>.
- (80) Clemenson, S.; David, L.; Espuche, E. Structure and Morphology of Nanocomposite Films Prepared from Polyvinyl Alcohol and Silver Nitrate: Influence of Thermal Treatment. *J. Polym. Sci. Part A Polym. Chem.* **2007**, *45*, 2657–2672. <https://doi.org/10.1002/pola>.
- (81) Ryu, D.; Loh, K. J.; Ireland, R.; Karimzada, M.; Yaghmaie, F.; Gusman, A. M. In Situ Reduction of Gold Nanoparticles in PDMS Matrices and Applications for Large Strain Sensing. *Smart Struct. Syst.* **2011**, *8* (5), 471–486. <https://doi.org/10.12989/sss.2011.8.5.471>.
- (82) Dunklin, J. R.; Forcherio, G. T.; Berry, K. R.; Roper, D. K. Gold Nanoparticle-Polydimethylsiloxane Thin Films Enhance Thermoplasmonic Dissipation by Internal Reflection. *J. Phys. Chem. C* **2014**, *118* (14), 7523–7531. <https://doi.org/10.1021/jp4112124>.
- (83) Nour, M.; Berean, K.; Chrimes, A.; Zoolfakar, A. S.; Latham, K.; McSweeney, C.; Field, M. R.; Sriram, S.; Kalantar-zadeh, K.; Ou, J. Z. Silver Nanoparticle/PDMS Nanocomposite Catalytic Membranes for H₂S Gas Removal. *J. Memb. Sci.* **2014**, *470*, 346–355. <https://doi.org/10.1016/j.memsci.2014.07.047>.
- (84) Goyal, A.; Kumar, A.; Patra, P. K.; Mahendra, S.; Tabatabaei, S.; Alvarez, P. J. J.; John, G.; Ajayan, P. M. In Situ Synthesis of Metal Nanoparticle Embedded Free Standing Multifunctional PDMS Films. *Macromol. Rapid Commun.* **2009**, *30* (13), 1116–1122. <https://doi.org/10.1002/marc.200900174>.
- (85) SadAbadi, H.; Badilescu, S.; Packirisamy, M.; Wüthrich, R. Integration of Gold Nanoparticles in PDMS Microfluidics for Lab-on-a-Chip Plasmonic Biosensing of Growth Hormones. *Biosens. Bioelectron.* **2013**, *44* (1), 77–84. <https://doi.org/10.1016/j.bios.2013.01.016>.

- (86) Kim, J. A.; Lee, S. H.; Park, H.; Kim, J. H.; Park, T. H. Microheater Based on Magnetic Nanoparticle Embedded PDMS. *Nanotechnology* **2010**, *21*, 165102. <https://doi.org/10.1088/0957-4484/21/16/165102>.
- (87) Schlemmer, C.; Betz, W.; Berchtold, B.; Rhe, J.; Santer, S. The Design of Thin Polymer Membranes Filled with Magnetic Particles on a Microstructured Silicon Surface. *Nanotechnology* **2009**, *20* (25), 255301. <https://doi.org/10.1088/0957-4484/20/25/255301>.
- (88) Pirmoradi, F.; Cheng, L.; Chiao, M. A Magnetic Poly(Dimethylesiloxane) Composite Membrane Incorporated with Uniformly Dispersed, Coated Iron Oxide Nanoparticles. *J. Micromechanics Microengineering* **2010**, *20* (1). <https://doi.org/10.1088/0960-1317/20/1/015032>.
- (89) Yu, X.; Wen, C.-Y.; Zhang, Z.-L.; Pang, D.-W. Control of Magnetic Field Distribution by Using Nickel Powder@PDMS Pillars in Microchannels. *RSC Adv.* **2014**, *4* (34), 17660. <https://doi.org/10.1039/c3ra47902a>.
- (90) Duong, B.; Khurshid, H.; Gangopadhyay, P.; Devkota, J.; Stojak, K.; Srikanth, H.; Tetard, L.; Norwood, R. A.; Peyghambarian, N.; Phan, M. H.; et al. Enhanced Magnetism in Highly Ordered Magnetite Nanoparticle-Filled Nanohole Arrays. *Small* **2014**, *10* (14), 2840–2848. <https://doi.org/10.1002/sml.201303809>.
- (91) Kallweit, C.; Bremer, M.; Smazna, D.; Karrock, T.; Adelung, R.; Gerken, M. Photoresponsive Hierarchical ZnO-PDMS Surfaces with Azobenzene-Polydopamine Coated Nanoparticles for Reversible Wettability Tuning. *Vacuum* **2017**, *146*, 386–395. <https://doi.org/10.1016/j.vacuum.2017.03.023>.
- (92) Albiss, B. A.; AL-Akhras, M. A.; Obaidat, I. Ultraviolet Photodetector Based on ZnO Nanorods Grown on a Flexible PDMS Substrate. *Int. J. Environ. Anal. Chem.* **2015**, *95* (4), 339–348. <https://doi.org/10.1080/03067319.2015.1016010>.
- (93) Belovickis, J.; Macutkevicius, J.; Svirskas, V.; Samulionis, V.; Banys, J.; Shenderova, O.; Borjanovic, V. Dielectric PDMS Nanocomposites with ZnO Nanoparticles. *Ferroelectrics* **2015**, *479* (1), 82–89. <https://doi.org/10.1080/00150193.2015.1012016>.
- (94) Almusallam, A. S.; Sholl, D. S. Brownian Dynamics Study of Polymer-Stabilized Nanoparticles. *Nanotechnology* **2005**, *16* (7), S409-15. <https://doi.org/10.1088/0957-4484/16/7/015>.
- (95) Dallas, P.; Georgakilas, V.; Niarchos, D.; Komninou, P.; Kehagias, T.; Petridis, D. Synthesis, Characterization and Thermal Properties of Polymer/Magnetite Nanocomposites. *Nanotechnology* **2006**, *17* (8), 2046–2053. <https://doi.org/10.1088/0957-4484/17/8/043>.
- (96) Agarwal, S.; Khan, M. M. K.; Gupta, R. K. Thermal Conductivity of Polymer Nanocomposites Made with Carbon Nanofibers. *Polym. Eng. Sci.* **2008**, *48* (12), 2474–2481. <https://doi.org/10.1002/pen.21205>.

- (97) Ghajar, Y. A. C. and A. J. *Heat and Mass Transfer: Fundamentals and Applications*, 4th ed.; The McGraw-Hill Companies: New York, 2011.
- (98) Berry, K. R.; Dunklin, J. R.; Blake, P. A.; Roper, D. K. Thermal Dynamics of Plasmonic Nanoparticle Composites. *J. Phys. Chem. C* **2015**, *119* (19), 10550–10557. <https://doi.org/10.1021/jp512701v>.
- (99) Baur, S.; Sanders, S.; Manjavacas, A. Hybridization of Lattice Resonances. *ACS Nano* **2018**, *12* (2), 1618–1629. <https://doi.org/10.1021/acsnano.7b08206>.
- (100) Khlopin, D.; Laux, F.; Wardley, W. P.; Martin, J.; Wurtz, G. A.; Plain, J.; Bonod, N.; Zayats, A. V.; Dickson, W.; Gérard, D. Lattice Modes and Plasmonic Linewidth Engineering in Gold and Aluminum Nanoparticle Arrays. *J. Opt. Soc. Am. B* **2017**, *34* (3), 691. <https://doi.org/10.1364/JOSAB.34.000691>.
- (101) Matricardi, C.; Hanske, C.; Garcia-Pomar, J. L.; Langer, J.; Mihi, A.; Liz-Marzán, L. M. Gold Nanoparticle Plasmonic Superlattices as Surface Enhanced Raman Spectroscopy Substrates. *ACS Nano* **2018**. <https://doi.org/10.1021/acsnano.8b04073>.
- (102) Zhu, J. X.; Zhou, W. L.; Wang, Z. Q.; Xu, H. Y.; Lin, Y.; Liu, W. Z.; Ma, J. G.; Liu, Y. C. Flexible, Transferable and Conformal Egg Albumen Based Resistive Switching Memory Devices. *RSC Adv.* **2017**, *7* (51), 32114–32119. <https://doi.org/10.1039/c7ra05237e>.

2. THERMAL DYNAMICS OF PLASMONIC NANOPARTICLE COMPOSITES

Keith R. Berry Jr.,¹ Jeremy R. Dunklin,¹ Phillip A. Blake,¹ and D. Keith Roper^{1,2,}*

¹Ralph E. Martin Department of Chemical Engineering, University of Arkansas, Fayetteville, AR 72701

²MicroElectronics-Photonics Graduate Program, University of Arkansas, Fayetteville, AR 72701

KEYWORDS: plasmonics, metamaterials, polymers, nanocomposites, thermal response

ABSTRACT

Thermal response rates of plasmonic nanocomposite materials limit their capacity for adaptive control and scalable implementation. This work examines thermal dynamics in insulating and conductive dielectrics containing two- and three-dimensional disordered distributions of plasmonic gold nanoparticles (AuNP). It is shown that a balance of micro- and macro-scale internal and external dissipation rates can model overall thermal dynamics and dissipation rates measured for widely varying composite materials to within a few percent using independent geometric and thermodynamic parameters. The independent estimates are within 2.6% of values measured for isolated colloid AuNP suspensions; between 0.15 to 13.4% for randomly-sized AuNP embedded in polymer films; and within 5.4 to 30.0% for AuNP deposited on conductive ceramics. Estimated thermal dynamics for AuNP embedded in thin polymer film are higher than AuNP in fluid or on ceramic substrates. This modeling approach could guide design and deployment of thermally responsive plasmonic energy materials, sensors, and therapeutics for heat-sensitive applications.

2.1 Introduction

Transparent dielectric materials containing plasmonic nanoparticles (NPs) are of increasing interest for fluid^{1,2} and solid sensing,³⁻⁸ electronics,⁹⁻¹² catalysis,¹³⁻¹⁶ water desalination,^{17,18} medical applications,¹⁹⁻²³ and microelectromechanical systems (MEMS).^{24,25} New routes to synthesize nanocomposite media²⁶⁻²⁸ and evolving approaches that describe their optical²⁹⁻³² and thermal properties^{26-31,33-39} and energetics⁴⁰ have expanded their utility. Optothermal descriptions of equilibrium and dynamic temperatures and fluxes in plasmon-heated materials and systems range from one-dimensional (1-D) analytical^{41,42} to 3-D computational methods.⁴³⁻⁴⁵ Yet limiting thermal response rates of available thermoplasmonic materials constrain their adaptive control and scalable implementation. A description of thermal dynamics based on widely applicable geometric and thermodynamic metrics is needed to design plasmonic nanocomposites with improved response for scalable incorporation into complex structures that could include heat-labile biophysical systems.

Thermal dynamics in resonantly-induced nanocomposites differ from those in continuous media heated by conventional bulk or resistive sources. In conventional heaters, micro- to macro-scale bulk, surface, or linear thermal sources drive heat flux in a direction opposite to a developing temperature gradient.⁴⁶ Conversely, 3-D distributions of plasmonic NPs in a host dielectric originate heat at point sources, which can improve its dissipation relative to surface or linear sources. Resonant induction of plasmons on NPs induces adsorptive thermal dissipation, as well as re-radiation, from nano-sized metal/dielectric interfaces.⁴⁷ Concurrently, geometric scattering from wavelength-scale inclusions and surface reflection may occur in nanocomposite materials containing NPs.^{48,49} Re-radiated, scattered, and reflected incident photons can supplement plasmon induction to accelerate thermal response and increase heat flux and equilibrium temperature in

nanocomposites beyond values absent these optical effects.⁵⁰ Despite widespread consideration of pseudo-equilibrium temperatures and thermal fluxes in resonantly irradiated nanoparticle-containing media, evaluation of the consistency of thermal dynamics with microscopic continuum description of thermal transport in these media has been limited.

Mathematical description of dynamic thermal response in nanocomposite materials ranges from analytical solutions^{41,42} to 3-D numerical analysis.^{43–45} Compact analytical models in particular provide rapid, intuitive insight into thermophysical behavior of nanocomposite materials.^{39–42,45,51,52} An analytic 1-D continuum description of optoplasmonic heating by NP in fluids and solids has been used to characterize external dissipation rates in micro- to nano-scale thermoplasmonic samples and systems in which internal equilibration is rapid.^{29,30,53–60} Resistance to internal dissipation becomes non-negligible, however, in thermally resistive polymers embedded with plasmonic nanoparticles. For such nanocomposite media, the validated expression for external dissipation must be concatenated with an expression for internal dissipation. However, an intuitive, analytic approach that evaluates relative contributions of both internal and external dissipation to overall thermal dynamics of nanocomposite media has not been previously examined.

This work shows measured values of overall thermal dissipation of transparent ceramic and polymer dielectrics that are embedded with 2- and 3-D disordered distributions of plasmonic NPs compare favorably with *a priori* predictions from a new, series-resistance model that accounts for internal as well as external dissipation rates. The NP-containing materials are considered in thermal isolation as well as in closed and open systems, some of which include phase change. A dynamic thermal response that balances internal microscale and external macroscale thermal dissipation rates is introduced. It is calculable independent of measured thermal dynamics using

thermodynamic and geometric metrics for each particular material and system. It is shown that the estimated dynamic thermal response of NPs distributed in polymer films is 8-fold higher than for isolated NPs on surfaces. Materials with predictable, high dynamic thermal response are better incorporated into complex devices, improve adaptive control, and enhance use with thermally-labile (e.g., biological) media. Accounting for both internal and external dissipation rates using intrinsic thermodynamic and geometric properties allows enhanced thermal dissipation rates to be distinguished in particular types of nanocomposite media. This approach could be broadly useful to guide intuition, design, and development of responsive plasmonic energy materials, sensors, MEMS, and therapeutics for heat-sensitive applications.

2.2 Materials & Methods

2.2.1 Materials

Polydimethylsiloxane (PDMS; Sylgard® 184 silicone elastomer kit #4019862) was purchased from Dow Corning (Midland, MI). Hydrogen tetrachloroaurate (III) (TCA; $\text{HAuCl}_4 \cdot 3\text{H}_2\text{O}$, G4022) was purchased from Sigma-Aldrich (St. Louis, MO). Organic spherical gold nanoparticles (oAuNPs) (20-NS-20-50, 16 nm) were purchased from Nanopartz (Loveland, CO). Distilled, de-ionized water (Milli-Q, Billerica, MA) was degassed (DDD) for use in preparing aqueous solutions.

2.2.2 Thermal equipment and data analysis

532 nm green solid state laser (MXL-H-532) was purchased from CNI (Changchun, China). Power meter (PM310D), shutter (SH05), and shutter controller (SC10) were purchased from Thorlabs (Newton, NJ). Infrared thermal imaging camera (ICI 7320, P-Series) with a pixel resolution of 320 x 240 was purchased from Infrared Cameras Inc. (Beaumont, TX).

As previously detailed, thermal data was collected from PDMS films and SiO₂ capillaries aligned vertically with a resonant laser using an infrared (IR) thermal imaging camera. The laser spot was centered in each sample.²⁹ Transmitted laser power up to 150 mW, obtained by adjusting a neutral density filter, was recorded before, during, and after each experiment using a power meter. The experiments consisted of 3 to 5-min resonant laser irradiation followed by cooling to baseline temperature. A programmable shutter opened and closed to control laser irradiation. The thermal imaging camera was programmed to record temperatures in- and outside the field of view during pre-equilibration, heating, and cooling. Thermal data from SiO₂ capillaries containing aqueous AuNP suspensions was obtained using a thermocouple.

Thermal time decays were computed as detailed previously.^{53–55} Thermal data was analyzed using MATLAB. To standardize results from films with different AuNP content, a cutoff time of 30 seconds was selected to calculate the thermal time decays. A sensitivity analysis of upper and lower relative variance at 30 +/- 10 seconds respectively showed modest increase/decrease of measured thermal time decay within 4 to 20 %. These variations were due primarily to drift in ambient temperature during cooling: as the time increased the change in temperature decreased. Calculations at 10 different positions in the laser spot confirmed reproducibility of the calculated values.

2.2.3 Fabrication of AuNP-containing samples

PDMS films with uniformly-sized, organic-coated (o) AuNPs

Table 2.1. Composition, geometry, arrangement, measured overall thermal equilibration time, and irradiation parameters for four AuNP nanocomposite samples.

	Sample 1 ²⁹	Sample 2 ⁵⁴	Sample 3 ⁵⁵	Sample 4 ⁵³
Description	Random (r) and uniform (o) AuNP in polymer	Random AuNP on SiO ₂	Random AuNP on SiO ₂ (elongated geometry)	Uniform AuNP in H ₂ O
Inner dimensions LxWxD (mm)	5.0 x 5.0 x 0.68	10 x 4.0 x 0.2	14 x 4.0 x 0.2	15.9 x 4.0 x 0.2
AuNP arrangement	3-D distribution	2-D distribution	2-D distribution	3-D suspension
AuNP type	AuNP (r) reduced from HAuCl ₄	NPs annealed from Au island film	NPs annealed from Au island film	20 nm Au colloid suspended in H ₂ O
	16 nm organic coated (o) AuNP			
Gold content (mass %)	Reduced (r): 0.007 to 0.190	H ₂ O: 0.0071	H ₂ O: 0.0108	0.0092
	Organic (o): 0.002 to 0.005	Air: 0.0018	Air: 0.0091	
Dielectric around AuNP	PDMS (r)	H ₂ O/SiO ₂	H ₂ O/SiO ₂	H ₂ O (colloid)
	PDMS (o)	Air/SiO ₂	Air/SiO ₂	
Measured overall thermal equilibration time, τ_T (s)	Reduced (r): 14.8 to 21.5	H ₂ O: 8.39 ± 1.05	H ₂ O: 15.56 ± 1.58	86.3 ± 8.61
	Organic (o): 14.8 to 16.4	Air: 4.79 ± 0.39	Air: 6.53 ± 0.41	
Laser wavelength (nm)	532	514	514.5	514
Laser power (mW)	100	4 to 18.4	50 to 150	170
Laser spot size (mm)	≤ 2	1.5	2.4	3
Irradiation time (s)	180	30 to 240	240	320

As was previously detailed, oAuNP-PDMS films were fabricated as follows.²⁹ The base polymer and curing agent were mixed in a ratio of 10:1 for a total of 1.0g. Suspended oAuNPs diluted in ethanol to 10^{13} NP/mL were added into 1.0 g of PDMS film solution. The oAuNPs-PDMS film solution was degassed and placed in an oven for 6 min at 70 °C to remove ethanol. The mixture was then degassed and mixed for an additional 10 min. Afterwards, the film was distributed evenly onto a glass curing surface and cured on a hot plate at 150 °C for 10 min. The resulting oAuNP-PDMS film was sectioned into 5.0 x 5.0 mm (width x length) squares with an approximate thickness of 0.65 mm. Spectroscopy and images confirm that AuNP dispersed by this and the following method result in random 3D distributions.^{29,30,49,50}

The composition, geometry, arrangement of AuNPs, and overall thermal equilibration times measured for these films are summarized in Table 2.1 (Sample 1o). The films were irradiated at 532 nm at a power of 100 mW until temperature stabilized. A programmable shutter was activated to cease irradiation, whereupon thermal equilibration times were measured to decrease from 16.4 to 14.8 s as Au content increased from 0.002 to 0.005 mass percent.

PDMS films with randomly-sized, reduced (r) NP

Briefly, rAuNP-PDMS films were fabricated similar to oAuNP-PDMS by first mixing the base polymer and curing agent in a ratio of 10:1 and adding diluted HAuCl₄ solution at eight different gold concentrations.²⁹ Ten μ L of each respective diluted HAuCl₄ solution was added to 2.0 g PDMS film solution, mixed, and heated at 70 °C to remove water. After further degassing and mixing, the films were distributed, thermally cured, and sectioned using the method discussed for oAuNP-PDMS.

Table 2.1 shows data for these films (Sample 1r). After irradiation at 532 nm at a power of 100 mW, thermal equilibration times were measured to decrease from 21.5 to 14.8 s as Au content increased from 0.007 to 0.19 mass percent. The decreases coincided with increases in mass-averaged composite thermal diffusivities for the respective samples. Mass-averaged composite thermal diffusivities represents an upper limit estimate of nanocomposite thermal conductivity. Employing bulk polymer values to estimate nanocomposite thermal diffusivity values reduced linearity and increased variability between predicted and measured values.

AuNPs on SiO₂

Briefly, AuNPs were thermally annealed from Au island films that had been electroless-plated onto silica capillaries.⁵⁴ Internal walls of SiO₂ capillaries were sensitized with tin solution for one min, activated by ammoniacal AgNO₃ for 30 s, then galvanically replaced by Au reduced from Na₃[Au(SO₃)₂] for 30 s. Sensitization, activation, and replacement were repeated three times at alternating ends of the capillary to provide uniform plating. AuNPs were formed by heating the Au island film at successively higher temperatures of 250, 350, and 500 °C with heating and cooling times of 15, 15, and 25 min, respectively. Table 2.1 shows data for the Au-coated capillaries (Sample 2) with inner dimensions of 0.2 x 4.0 x 10.0 mm (D x W x L) and a wall thickness of 0.2 mm.

A second set of thermally annealed EL gold plated films on longer silica capillaries (Sample 3) was fabricated by a slight modification of this approach.⁵⁵ Sensitization, activation and galvanic replacement steps were repeated in 1 min, 30 s, and 30 s intervals for total exposure times of 3 min, 2 min, and 4 min, respectively. AuNPs were annealed from the gold films plated on the

capillaries at successive temperatures of 250 and 750 °C at heating ramp times of 1 h and 30 min with exposure times of 3 h and 30 min, respectively. Inner dimensions of the longer capillaries were 0.2 x 4.0 x 14.0 mm (D x W x L) with a wall thickness of 0.2 mm.

Thermal equilibration times for each capillary were examined under empty conditions (i.e., air-filled; 2a and 3a) as well as filled with water (2w and 3w) to evaluate effects of increased thermal mass, conductivity, and heat capacity in a comparable geometry. Irradiation was at a resonant wavelength of 514 nm at powers from 4 to 18.4 mW for Sample 2. This yielded thermal equilibration times of ~4.8 and ~8.4 s for empty and water-filled capillaries shown in Table 2.1, respectively. Increasing thermal mass by including water in the capillary lengthened the thermal response time. Irradiation of Sample 3 at 514.5 nm at powers between 50 and 150 mW resulted in predictably longer thermal equilibration times of ~6.5 and ~15.6 s for these empty and water-filled capillaries, respectively.

AuNP suspension

Briefly, 20 nm diameter Au colloid purchased from Sigma (G 1652, St. Louis, MO) was concentrated to ~0.01% w/v Au at 12000 rpm for 15-20 min, then resuspended in DDD water.⁵³ The suspension was placed in a glass capillary tube with inner dimensions of 0.2 x 4.0 x 15.9 mm (D x W x L) and a wall thickness of 0.2 mm. It was sealed in place using 5 Minute Epoxy. Irradiating the capillary isolated at vacuum conditions with a 514 nm laser at 170 mW resulted in an external thermal time constant of ~86 s. Measured thermal equilibration times for Sample 4, shown in Table 2.1, were higher than for other samples due to elimination of convection,

minimization of conduction, and suspension of the AuNP in an aqueous matrix with a high heat capacity.

2.2.4 Dissipation rates and dynamic thermal response

The overall dynamic thermal response of a plasmonic system to resonant irradiation is a result of its external dissipation, $\tau_{ext} = \Sigma m_i C_{p,i}/U$, relative to its intrinsic internal dissipation, $\tau_{int} = L_c^2/\alpha$, where subscript i represents each respective component in the sample, m_i is its mass, $C_{p,i}$ is its heat capacity, L_c is a characteristic thermal length of the sample (for 3D AuNP distributions, $L_c = D$, sample thickness; for 2D AuNP distributions, $L_c =$ the average distance from the plane of AuNP to each major sample surface), α is the mass-averaged thermal diffusivity calculated on a percent mass basis, and U is defined as⁵⁵

$$U \equiv \frac{k_c A_c}{L_c} + h_{conv} A_s + A_s \varepsilon \sigma (T^2 + T_{amb}^2)(T + T_{amb}) \quad (1)$$

where k_c is the thermal conductivity of the heat-conductive material, A_c is the contact area perpendicular to conduction, L_c is the characteristic length for conduction to the environment, h_{conv} is the heat transfer coefficient for convection, A_s is the surface area of the film, ε is the emissivity of the material, σ is the Stefan-Boltzmann constant, and T_{amb} is the ambient temperature. T represents the dynamically changing surface temperature that occurred during heating or cooling of the sample. The value of T used for calculations in this work was the average surface temperature at hot equilibrium, T_{max} . This represented an upper limit for U since the hot equilibrium surface temperature occurred only at the start (end) of cooling (heating). Use of $T = (T_{max} + T_{amb})/2$ (or other intermediate values) reduced differences between measures and estimates of dissipation rate and thermal response.

Estimation of h_{conv} in microscopic plasmonic systems was recently examined.⁵⁰ For horizontal systems irradiated at the lower surface, like AuNP-PDMS polymer films, h_{conv} is estimated by^{46,50}

$$h_{conv} = \frac{k}{L_c} 0.27 Ra_L^{1/4} \quad (2)$$

where k is the thermal conductivity of the fluid, L_c is a characteristic length defined as the film area divided by the plate perimeter, and Ra_L is the Rayleigh number defined by $Ra_L = g\rho^2\beta C_p(T - T_{amb})L^3/k\mu$ where g is acceleration due to gravity, ρ , β , C_p , k , μ are the density, coefficient of thermal expansion, heat capacity, thermal conductivity, and viscosity of the fluid, respectively. It is noted that Raleigh numbers for the samples studied fall outside the range for which this correlation was obtained. Use of a second correlation for horizontal plates in which a coefficient of 0.54 replaced 0.27 resulted in estimates for thermal dissipation decreasing by as much as 53%.

For vertical systems irradiated from the side, like the AuNPs on SiO₂, h_{conv} is estimated by^{46,50}

$$h_{conv} = \frac{k}{L_c} \left[0.68 + \frac{0.67 Ra_L^{1/4}}{\left(\left(1 + \frac{0.492k}{\mu C_p} \right)^{9/16} \right)^{4/9}} \right] \quad (3)$$

where k , μ , C_p , and Ra_L are defined as in Equation (2) and L_c is defined as the height of the plate in the vertical direction.

External dissipation varies with sample composition and geometry as well as environment. Internal dissipation is determined by composition and geometry. Taking a ratio of external, $\tau_{ext} = \Sigma m_i C_{p,i} / U$, relative to internal, $\tau_{int} = L_c^2 / \alpha$, dissipation times, and accounting for geometry of the sample or system yields an expression for the characteristic time for external heat dissipation, τ_{ext} ,

$$\tau_{ext} \equiv \frac{1}{\alpha} \frac{k}{U} L \cdot W \cdot D \quad (4)$$

where α is the mass-averaged thermal diffusivity, k is the mass-averaged thermal conductivity calculated on the same mass percent basis, U is the overall heat transfer coefficient defined in

Equation (1), and D, W, L , are thickness, width, and length of the sample. See supporting information for details.

2.3 Results & Discussion

2.3.1 Overall thermal dissipation rate and dynamic thermal response

Total overall resistance, R_T , to thermal dissipation when internal and external dissipation occur at distinguishable rates may be described by a series relationship, $R_T = \sum_i R_i$ where subscript i denotes system components with varying thermal resistances R_i . Written terms of dissipation rates, with time constants being proportional to resistances, this relationship becomes

$$\frac{1}{\tau_T} = \frac{1}{\sum_i \tau_i} = \frac{1}{\tau_{int} + \tau_{ext}} = \frac{1}{\tau_{int}} \left[\frac{1}{1 + \frac{\tau_{ext}}{\tau_{int}}} \right] \quad (5)$$

where τ_{int} and τ_{ext} are the internal and external time constants for thermal dissipation as defined above. The right hand side of Equation (5) has been rearranged to indicate that for thermally conductive substrates that support NPs (i.e., ceramics) when $\tau_{int} \ll \tau_{ext}$, then $\tau_T \sim \tau_{ext}$.

Overall thermal dissipation in samples for which $\tau_{int} \ll \tau_{ext}$ can be analyzed by considering only external dissipation processes while neglecting effects of internal dissipation rate. External heat dissipation processes are described in Equation (1): conduction, convection, and radiation. This is the approach taken to date for fluidic and ceramic AuNP-containing materials. It has been validated for multiple geometries.^{53–55} However, when $\tau_{int} \sim \tau_{ext}$, the overall dissipation rate reduces to half the internal (external) dissipation rate, and the full expression in Equation (5) must be used to accurately compare measured dissipation rates to estimates of overall dissipation. This latter approach is introduced in this work to characterize plasmonic AuNP thermal dynamics and

dissipation rates on thermally resistive polymer substrates, conductive ceramic substrates, and fluid suspensions.

The dimensionless ratio τ_{ext}/τ_{int} in Equation (5) is characteristic of the overall dynamic thermal response of the system. It is a measure of the rate at which energy is dissipated from the nanoplasmonic system to its environment, relative to the rate that energy is dispersed via conduction or other means (e.g., via optical scattering, reflection, or re-radiation for plasmonically-heated systems) within the system. By using Equations (1)–(4), this ratio may be determined *a priori* from thermodynamic and geometric parameters of the system by taking the external heat dissipation rate, the reciprocal of (4), relative to the internal dissipation rate, $\tau_{int}^{-1} = \alpha/L_c^2$. This results in an estimate for dynamic thermal response given by

$$\frac{\tau_{int}}{\tau_{ext}} = \frac{U}{k} \frac{D}{WL} \quad (6)$$

2.3.2 Dynamic thermal responses of AuNP-containing samples

Figure 2.1 shows dynamic thermal responses estimated using Equation (6) for Samples 1 to 4 in Table 1 plotted against the rate of internal dissipation. The highest dynamic thermal responses were exhibited by plasmonically heated PDMS films in which uniform 16-nm AuNP (Sample 1o, red circles) or heterogeneous AuNP (1r, black circles) have been embedded. This occurred primarily due to lower thermal diffusivities in these samples than in short (Sample 2, squares) or long (Sample 3, triangles) silica capillaries whose inner surfaces were decorated by electroless deposited AuNP. Vacuum-insulated silica capillaries containing AuNP colloid suspended in water (Sample 4, diamonds) had the lowest dynamic thermal responses due to reduced convective heat transfer externally.

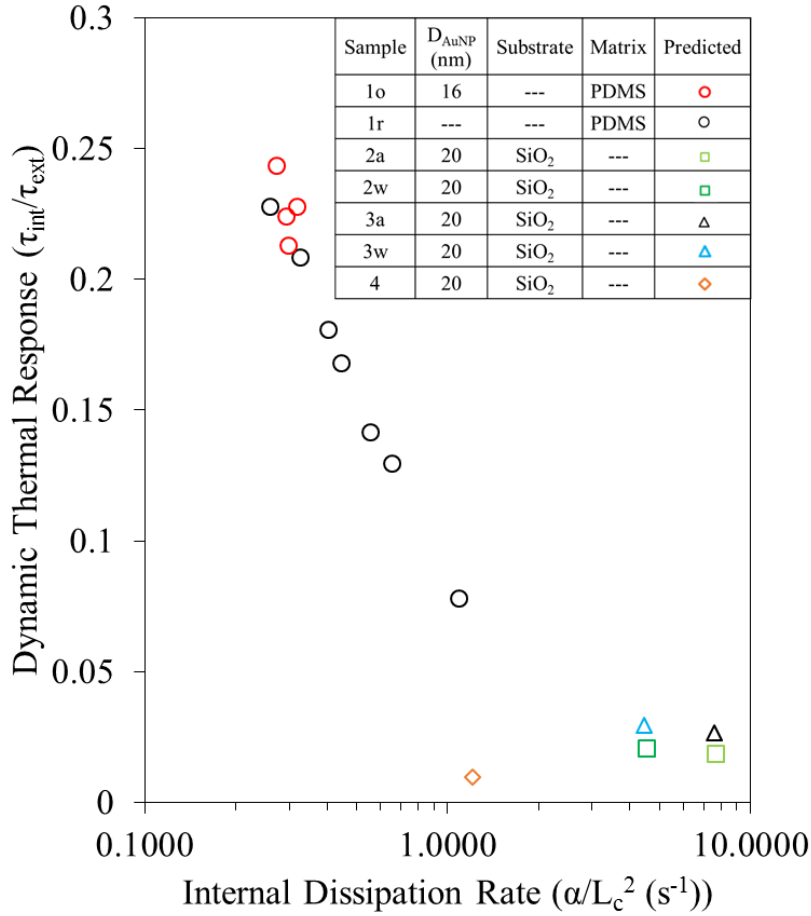


Figure 2.1 Dynamic thermal response, UD/kWL, estimated using Equation (6) for AuNP-containing composites made primarily of PDMS (Sample 1, circles) or silica (Sample 2, squares; Sample 3, triangles; and Sample 4, diamonds). Dynamic thermal response is plotted vs. internal dissipation rate.

Dynamic thermal responses of PDMS embedded with uniform or heterogeneous AuNP decreased from about 0.24 to 0.08 as the Au content in the samples was lowered. These values for dynamic thermal response were from three to 26 times higher than those for silica capillaries decorated with AuNP. Since for PDMS media embedded with AuNP, τ_{int} approaches τ_{ext} , use of the full expression in Equation (5), rather than the simple expression for external dissipation, $\tau_{ext} = \Sigma m_i C_{p,i} / U$, was required to fully characterize the thermal dynamics and overall dissipation rate of these samples. This represents the first instance that an analytic heuristic for internal and

external dissipation based on independently-measured thermodynamic and geometric parameters had been introduced to characterize overall thermal dynamics of nanocomposite media.

2.3.3 Thermal dissipation rates of AuNP-containing samples

Figure 2.2 compares the measured rate of total thermal dissipation, τ_T , (units of inverse seconds) for each sample (filled symbols) with corresponding rates estimated *independently* from thermodynamic and geometric parameters (hollow symbols) using Equations (1) through (5). Values of τ_T are plotted as a function of characteristic internal thermal dissipation rates, α/L_c^2 , for each sample. For measured data, error bars show +/- two standard deviations for replicate data; error bars not seen were too narrow to appear outside the symbols.

In general, measured and estimated values of the total dissipation rate increased with the mass-averaged thermal diffusivity (α) of the sample. As examples: total dissipation rate increased with increased Au content in Samples 1o and 1r; and total dissipation rate typically increased for conductive substrates (Samples 2a, 2w, 3a, 3w) relative to insulative substrates (Samples 1r, 1o). Faster internal thermal dissipation (i.e., lower τ_{int}) yielded more rapid system equilibration, (i.e., lower τ_T) as anticipated by Equation (5).

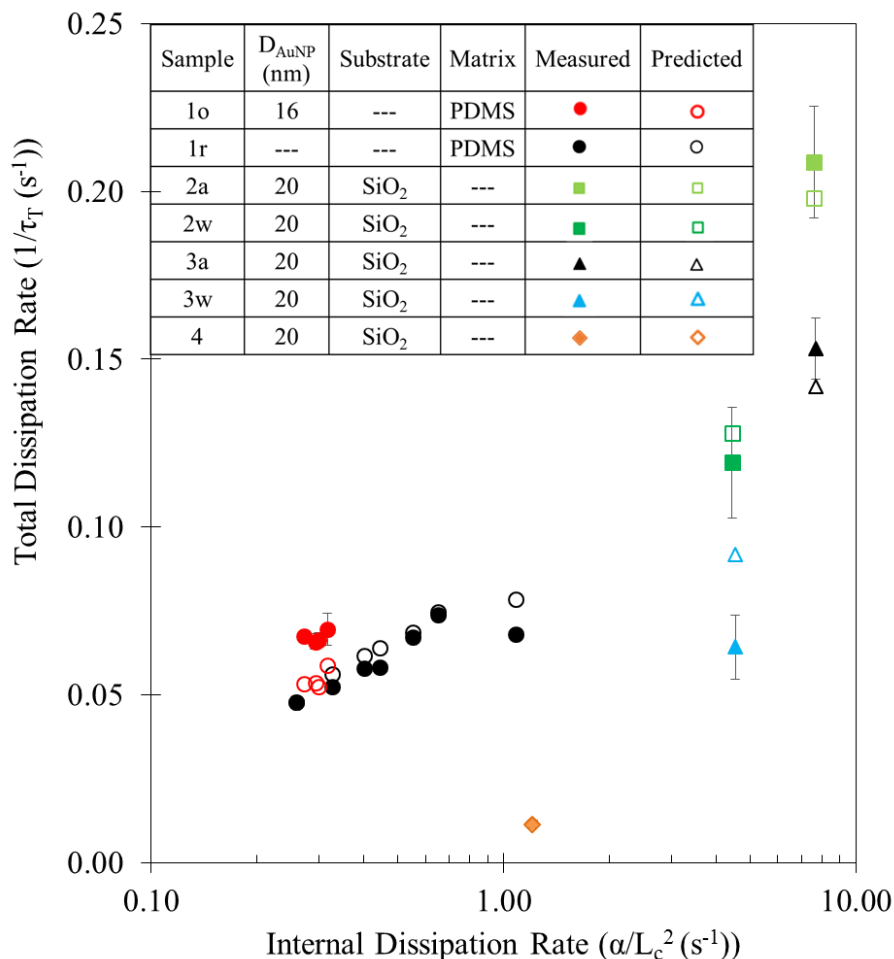


Figure 2.2 Measured (filled symbols) and estimated (open symbols) values of total dissipation rate for: PDMS film embedded with uniform 16-nm AuNP (Sample 1o; red circle) or heterogeneous reduced AuNP (Sample 1r; black circle); SiO₂ capillaries of short (Sample 2, squares) or long (Sample 3, triangles) dimensions on whose inner surfaces AuNP were annealed, either empty (2a, light green square; 3a, black triangle) or filled with water (2w, dark green square; 3w blue triangle); and SiO₂ capillaries filled aqueous AuNP suspension (Sample 4; orange diamonds).

For a particular material (SiO₂ or PDMS), the total dissipation rate was increased relative to internal thermal processes by the following: (1) decreasing thermal mass of the sample by replacing water (Samples 2w and 3w) with air (Samples 2a and 3a); (2) reducing sample elongation (Samples 2a, 2w vs. 3a, 3w); or (3) using uniform oAuNP (Sample 1o) rather than non-uniform rAuNP (Sample 1r). In contrast, minimizing external heat transfer by insulating capillary surfaces

from convection (Sample 4) dampened total dissipation rate relative to uninsulated Samples 1, 2, and 3.

More conductive materials (i.e., Samples 2a, 2w, 3a, 3w, and 4) exhibited values of total dissipation rate that were approximately 1% (Sample 4) to 3% (Sample 2a) of corresponding internal dissipation rates. As an example, the internal (external) dissipation rate estimated for Sample 2a was 7.603 s^{-1} (0.2034 s^{-1}), giving an estimate of 0.1981 s^{-1} for the total dissipation rate using Equation (5). This estimate was within 2.6 % of the measured total dissipation rate of 0.2088 s^{-1} . Conductive materials decorated with AuNP clearly exhibited $\tau_{\text{int}} \ll \tau_{\text{ext}}$ so that total dissipate rate was dominated by the external heat dissipation rate.

More insulating materials (i.e. Samples 1o and 1r) exhibited values of total dissipation rate that were approximately 8 to 20% of corresponding the internal dissipation rates. For example, the PDMS-based Sample 1r that contained the least gold (i.e., the left-most filled black circle in Figure 2.2) had an internal (external) dissipation rate of 0.2579 s^{-1} (0.0587 s^{-1}). This yielded an estimate of 0.0478 s^{-1} for total dissipation rate using Equation (5), which was nearly equal to the measured total dissipation rate of 0.0479 s^{-1} . Thus for insulative materials embedded with AuNP, both internal and external dissipation contribute to overall dissipation rates.

2.3.4 Measured vs. estimated total dissipation rates of AuNP-containing samples

Overall, correspondence between measured total dissipation rate (filled symbols) and independent *a priori* estimates from physical and geometric parameters (hollow symbols) in Figure 2.2 is noteworthy, considering the broad ranges of thermal diffusivities, geometric dimensions, and morphologies represented by these nanocomposite materials and systems. Samples 4, 2a, 3a,

and 1r exhibited the closest agreement. Estimates for total dissipation rates were within 2.6% of values measured for isolated colloid NP suspensions (Sample 4); within 5.4 to 8.0% for AuNP deposited on SiO₂ surrounded by air (Sample 2a and 3a); and within 0.15 to 13.4% of values measured for random NPs embedded in PDMS (Sample 1r).

This close agreement occurred despite the range of thermodynamic and geometric parameters represented by these materials. For example, the thermal diffusivity of silica-based Sample 3a ($6.9\text{e-}7 \text{ m}^2/\text{s}$) was seven-fold (1.3-fold) larger than the lowest (highest) Au-containing PDMS-based piece of the series in Sample 1r: $\sim 1.23\text{e-}7 \text{ m}^2/\text{s}$ ($5.17 \text{ e-}7 \text{ m}^2/\text{s}$). The longest dimension of Sample 4 (15.9 mm) was three-fold higher than that in Sample 1r (5 mm). Samples 2a and 3a consisted of randomly-sized AuNP annealed from Au island film that were distributed two-dimensionally on a conductive SiO₂ surface; whereas Sample 1r consisted of randomly-sized AuNP reduced from Au salt distributed three dimensionally throughout the bulk polymer. Sample 4 contained uniformly-sized, pre-formed AuNP dispersed in a colloidal fluid suspension.

Measured values for total dissipation rate for PDMS embedded with three-dimensional dispersions of pre-formed, uniform AuNP were, on average, 19% larger than estimates. The difference in measured dissipation rate relative to estimated rate was consistent in sign and comparable in magnitude with corresponding differences in measured surface power emission relative to estimated emission reported for PDMS thin films embedded with AuNP.⁵⁰ Reported power emission was attributable by finite element analysis to Mie absorption, Fourier heat conduction, Rayleigh convection, and Stefan-Boltzmann radiation. Examination is underway to elucidate the source of these differences.

2.3.5 A new analytic heuristic for thermal dissipation rates from AuNP-containing samples

This work introduced and validated an analytic heuristic that combined micro-scale internal and macro-scale external dissipation rates based on independently-measured thermodynamic and geometric parameters to characterize thermal dynamics (dynamic thermal response rates and overall dissipation rates) of conductive and insulating materials resonantly heated by plasmonic AuNP. The need for the expanded heuristic in insulating polymer nanocomposite media was confirmed. Its utility in estimating thermal dynamics was validated for broad variations in several sample features: sample composition (including gas, fluid, and solid components), geometry, and morphology; AuNP size, distribution, and arrangement (2-D or 3-D); thermophysical parameters (conductivity, heat capacity, density, diffusivity); and thermal environments (vacuum isolation, convective, conductive, and radiative) for microscopic, continuum systems. This systematic approach provides an intuitive, useful heuristic to design and tune active thermal activity in thermoplasmonic systems to obtain a desired thermal dissipation rate/equilibration time. This has value in development of responsive plasmonic energy materials, sensors, MEMS, and therapeutics in heat-sensitive applications.

2.4 Conclusions

Characterization of thermal dynamics in insulating polymer films embedded with AuNP requires consideration of both internal, bulk conductivity as well as external convection, conduction, and radiation to understand and estimate thermoplasmonic dynamics. Series summation of internal and external rate processes estimated independently using geometric and thermodynamic

parameters accurately represents overall measured thermal dissipation rates in materials that have a broad range of sample composition, geometry, and morphology; NP size, distribution, and arrangement; thermophysical parameters; and surrounding thermal environments. Total thermal dissipation rates from aqueous suspensions or insulating polymer media containing homogeneously dispersed, random-sized NPs may be estimated to within a few percent of measured values using this relationship. This intuitive, heuristic approach could be useful to design plasmonically-heated nanocomposite samples that balance external and internal dissipation rates in order to obtain desired thermal responses to support use of thermally responsive plasmonic materials in energy, sensing, and theranostics.

2.5 Author Information

Corresponding Author

*Corresponding author. E-mail: dkroper@uark.edu, phone: (801) 891-8921, fax: (703) 292-9051.

Author Contributions

K. Berry performed numerical analysis, and prepared text and figures for the manuscript. J. Dunklin provided guidance in heat transfer calculations and organization of the manuscript. P. Blake provided initial calculation guidance and mass-averaged calculation guidance for samples on SiO₂ cells. D.K. Roper derived the approach, directed the work, and refined compilation of the final document.

2.6 Acknowledgements

Funding Sources

NSF CBET-1134222, NSF ECCS-1006927, STEM Arkansas Space Grant Consortium, University of Arkansas Foundation, Walton Family Charitable Foundation

Acknowledgements

This work was supported in part by NSF CBET-1134222, NSF ECCS-1006927, the University of Arkansas Foundation, and the Walton Family Charitable Foundation. K. Berry acknowledges support from a STEM Arkansas Space Grant Consortium award. J. Dunklin acknowledges support from a NSF GRFP award. Any opinions, findings, and conclusions or recommendations expressed in this material are those of the authors and do not necessarily reflect the views of the National Science Foundation.

2.7 References

- (1) Massaro, A.; Spano, F.; Cingolani, R.; Athanassiou, A. Experimental Optical Characterization and Polymeric Layouts of Gold PDMS Nanocomposite Sensor for Liquid Detection. *IEEE Sens. J.* **2011**, *11* (9), 1780–1786. <https://doi.org/10.1109/JSEN.2011.2104414>.
- (2) Massaro, A.; Spano, F.; Cingolani, R.; Athanassiou, A. Pillar Type PDMS Nanocomposite Optical Sensors for Liquid Detection Systems. **2011**, *1*, 819–827.
- (3) Bao, M.; Chen, Y.; Li, F.; Ma, J.; Lv, T.; Tang, Y.; Chen, L.; Xu, Z.; Wang, T. Plate-like P–n Heterogeneous NiO/WO₃ Nanocomposites for High Performance Room Temperature NO₂ Sensors. *Nanoscale* **2014**, *6* (8), 4063. <https://doi.org/10.1039/c3nr05268k>.
- (4) Cui, F.; Zhang, X. Electrochemical Sensor for Epinephrine Based on a Glassy Carbon Electrode Modified with Graphene/Gold Nanocomposites. *J. Electroanal. Chem.* **2012**, *669*, 35–41. <https://doi.org/10.1016/j.jelechem.2012.01.021>.

- (5) Jiang, C.; Markutsya, S.; Pikus, Y.; Tsukruk, V. V. Freely Suspended Nanocomposite Membranes as Highly Sensitive Sensors. *Nat. Mater.* **2004**, *3* (10), 721–728. <https://doi.org/10.1038/nmat1212>.
- (6) Roper, D. K.; Ahn, W.; Taylor, B.; Asén, A. G. D. Enhanced Spectral Sensing by Electromagnetic Coupling With Localized Surface Plasmons on Subwavelength Structures. *IEEE Sens. J.* **2010**, *10* (3), 531–540. <https://doi.org/10.1109/JSEN.2009.2038451>.
- (7) Krasteva, N.; Besnard, I.; Guse, B.; Bauer, R. E.; Müllen, K.; Yasuda, A.; Vossmeier, T. Self-Assembled Gold Nanoparticle/Dendrimer Composite Films for Vapor Sensing Applications. *Nano Lett.* **2002**, *2* (5), 551–555. <https://doi.org/10.1021/nl020242s>.
- (8) Ryu, D.; Loh, K. J.; Ireland, R.; Karimzadeh, M.; Yaghmaie, F.; Gusman, A. M. In Situ Reduction of Gold Nanoparticles in PDMS Matrices and Applications for Large Strain Sensing. *Smart Struct. Syst.* **2011**, *8* (5), 471–486. <https://doi.org/10.12989/sss.2011.8.5.471>.
- (9) Gensler, R.; Gröppel, P.; Muhrer, V.; Müller, N. Application of Nanoparticles in Polymers for Electronics and Electrical Engineering. In *Particle and Particle Systems Characterization*; 2002. [https://doi.org/10.1002/1521-4117\(200211\)19:5<293::AID-PPSC293>3.0.CO;2-N](https://doi.org/10.1002/1521-4117(200211)19:5<293::AID-PPSC293>3.0.CO;2-N).
- (10) Goyal, R. K.; Tiwari, A.; Mulik, U.; Negi, Y. Novel High Performance Al₂O₃/Poly(Ether Ether Ketone) Nanocomposites for Electronics Applications. *Compos. Sci. Technol.* **2007**, *67* (9), 1802–1812. <https://doi.org/10.1016/j.compscitech.2006.10.020>.
- (11) Karttunen, M.; Ruuskanen, P.; Pitk?nen, V.; Albers, W. M. Electrically Conductive Metal Polymer Nanocomposites for Electronics Applications. *J. Electron. Mater.* **2008**, *37* (7), 951–954. <https://doi.org/10.1007/s11664-008-0451-2>.
- (12) Qi, X.; Tan, C.; Wei, J.; Zhang, H. Synthesis of Graphene-Conjugated Polymer Nanocomposites for Electronic Device Applications. *Nanoscale* **2013**, *5* (4), 1440–1451. <https://doi.org/10.1039/c2nr33145d>.
- (13) Kovalenko, V. V.; Rumyantseva, M. N.; Gaskov, A. M.; Makshina, E. V.; Yushchenko, V. V.; Ivanova, I. I.; Ponzoni, A.; Faglia, G.; Comini, E. SnO₂/Fe₂O₃ Nanocomposites: Ethanol-Sensing Performance and Catalytic Activity for Oxidation of Ethanol. *Inorg. Mater.* **2006**, *42* (10), 1088–1093. <https://doi.org/10.1134/S0020168506100074>.
- (14) Steigerwalt, E. S.; Deluga, G. A.; Lukehart, C. M. Pt-Ru/Carbon Fiber Nanocomposites: Synthesis, Characterization, and Performance as Anode Catalysts of Direct Methanol Fuel Cells. A Search for Exceptional Performance. *J. Phys. Chem. B* **2002**, *106* (4), 760–766. <https://doi.org/10.1021/jp012707t>.
- (15) Subramanian, V.; Wolf, E. E.; Kamat, P. V. Catalysis with TiO₂/Gold Nanocomposites. Effect of Metal Particle Size on the Fermi Level Equilibration. *J. Am. Chem. Soc.* **2004**, *126* (15), 4943–4950. <https://doi.org/10.1021/ja0315199>.

- (16) Yi, D. K.; Lee, S. S.; Ying, J. Y. Synthesis and Applications of Magnetic Nanocomposite Catalysts. *Chem. Mater.* **2006**. <https://doi.org/10.1021/cm052885p>.
- (17) Corry, B. Designing Carbon Nanotube Membranes for Efficient Water Desalination. *J. Phys. Chem. B* **2008**. <https://doi.org/10.1021/jp709845u>.
- (18) Humplik, T.; Lee, J.; O'Hern, S. C.; Fellman, B. A.; Baig, M. A.; Hassan, S. F.; Atieh, M. A.; Rahman, F.; Laoui, T.; Karnik, R.; et al. Nanostructured Materials for Water Desalination. *Nanotechnology*. 2011. <https://doi.org/10.1088/0957-4484/22/29/292001>.
- (19) Ghosh, S.; Ghosh, D.; Bag, P. K.; Bhattacharya, S. C.; Saha, A. Aqueous Synthesis of ZnTe/Dendrimer Nanocomposites and Their Antimicrobial Activity: Implications in Therapeutics. *Nanoscale* **2011**, 3 (3), 1139. <https://doi.org/10.1039/c0nr00610f>.
- (20) Neoh, K. G.; Kang, E. T. Functionalization of Inorganic Nanoparticles with Polymers for Stealth Biomedical Applications. *Polym. Chem.* **2011**, 2 (4), 747–759. <https://doi.org/10.1039/C0PY00266F>.
- (21) Owens, D. E.; Eby, J. K.; Jian, Y.; Peppas, N. A. Temperature-Responsive Polymer–gold Nanocomposites as Intelligent Therapeutic Systems. *J. Biomed. Mater. Res. Part A* **2007**, 83A (3), 692–695. <https://doi.org/10.1002/jbm.a.31284>.
- (22) Sassaroli, E.; Li, K. C. P.; O'Neill, B. E. Numerical Investigation of Heating of a Gold Nanoparticle and the Surrounding Microenvironment by Nanosecond Laser Pulses for Nanomedicine Applications. *Phys. Med. Biol.* **2009**, 54 (18), 5541–5560. <https://doi.org/10.1088/0031-9155/54/18/013>.
- (23) Scott, A.; Gupta, R.; Kulkarni, G. U. A Simple Water-Based Synthesis of Au Nanoparticle/PDMS Composites for Water Purification and Targeted Drug Release. *Macromol. Chem. Phys.* **2010**, 211 (15), 1640–1647. <https://doi.org/10.1002/macp.201000079>.
- (24) Prashanthi, K.; Naresh, M.; Seena, V.; Thundat, T.; Ramgopal Rao, V. A Novel Photoplastic Piezoelectric Nanocomposite for MEMS Applications. *J. Microelectromechanical Syst.* **2012**. <https://doi.org/10.1109/JMEMS.2011.2178118>.
- (25) Zhang, Q.; Xu, J. J.; Liu, Y.; Chen, H. Y. In-Situ Synthesis of Poly(Dimethylsiloxane)-Gold Nanoparticles Composite Films and Its Application in Microfluidic Systems. *Lab Chip* **2008**, 8 (2), 352–357. <https://doi.org/10.1039/b716295m>.
- (26) Cavallaro, G.; Donato, D. I.; Lazzara, G.; Milioto, S. Films of Halloysite Nanotubes Sandwiched between Two Layers of Biopolymer: From the Morphology to the Dielectric, Thermal, Transparency, and Wettability Properties. *J. Phys. Chem. C* **2011**, 115 (42), 20491–20498. <https://doi.org/10.1021/jp207261r>.
- (27) Zhou, M.; Bron, M.; Schuhmann, W. Controlled Synthesis of Gold Nanostructures by a Thermal Approach. *J. Nanosci. Nanotechnol.* **2008**, 8 (7), 3465–3472. <https://doi.org/10.1166/jnn.2008.172>.

- (28) Zillohu, A. U.; Abdelaziz, R.; Hedayati, M. K.; Emmeler, T.; Homaeigohar, S.; Elbahri, M. Plasmon-Mediated Embedding of Nanoparticles in a Polymer Matrix: Nanocomposites Patterning, Writing, and Defect Healing. *J. Phys. Chem. C* **2012**, *116* (32), 17204–17209. <https://doi.org/10.1021/jp3016358>.
- (29) Berry Jr, K. R.; Russell, A. G.; Blake, P. A.; Keith Roper, D. Gold Nanoparticles Reduced *in Situ* and Dispersed in Polymer Thin Films: Optical and Thermal Properties. *Nanotechnology* **2012**, *23* (37), 375703. <https://doi.org/10.1088/0957-4484/23/37/375703>.
- (30) Dunklin, J. R.; Forcherio, G. T.; Berry, K. R.; Roper, D. K. Asymmetric Reduction of Gold Nanoparticles into Thermoplasmonic Polydimethylsiloxane Thin Films. *ACS Appl. Mater. Interfaces* **2013**, *5* (17). <https://doi.org/10.1021/am4018785>.
- (31) Guillet, Y.; Rashidi-Huyeh, M.; Prot, D.; Palpant, B. Gold Nanoparticle Assemblies: Interplay between Thermal Effects and Optical Response. *Gold Bull.* **2008**. <https://doi.org/10.1007/BF03214892>.
- (32) Peter N. Njoki, I-Im S. Lim, Derrick Mott, Hye-Young Park, † Bilal Khan, Suprav Mishra, Ravishanker Sujakumar, Jin Luo, and C.-J. Z. Size Correlation of Optical and Spectroscopic Properties for Gold Nanoparticles. *J. Phys. Chem. C* **2007**, *111*, 14664–14669. <https://doi.org/10.1021/jp074902z>.
- (33) Borca-Tasciuc, T.; Borca-Tasciuc, D. A.; Chen, G. A Photo-Thermoelectric Technique for Anisotropic Thermal Diffusivity Characterization of Nanowire/Nanotube Composites. *Annu. IEEE Semicond. Therm. Meas. Manag. Symp.* **2005**, 283–291. <https://doi.org/10.1109/STHERM.2005.1412193>.
- (34) Cole, D. H.; Shull, K. R.; Baldo, P.; Rehn, L. Dynamic Properties of a Model Polymer/Metal Nanocomposite: Gold Particles in Poly(*Tert*-Butyl Acrylate). *Macromolecules* **1999**, *32* (3), 771–779. <https://doi.org/10.1021/ma981252b>.
- (35) Luo, J.; Maye, M. M.; Han, L.; Kariuki, N. N.; Jones, V. W.; Lin, Y.; Engelhard, M. H.; Zhong, C. J. Spectroscopic Characterizations of Molecularly Linked Gold Nanoparticle Assemblies upon Thermal Treatment. *Langmuir* **2004**. <https://doi.org/10.1021/la036163t>.
- (36) Palpant, B.; Guillet, Y.; Rashidi-Huyeh, M.; Prot, D. Gold Nanoparticle Assemblies: Thermal Behaviour under Optical Excitation. *Gold Bull.* **2008**. <https://doi.org/10.1007/BF03216588>.
- (37) Souier, T.; Samad, Y. A.; Lalia, B. S.; Hashaikeh, R.; Chiesa, M. Nanoscale Thermal Analysis of Multiphase Polymer Nanocomposites. *J. Phys. Chem. C* **2012**, *116* (15), 8849–8856. <https://doi.org/10.1021/jp301410e>.
- (38) Walsh, M. J.; Yoshida, K.; Gai, P. L.; Boyes, E. D. *In-Situ* Heating Studies of Gold Nanoparticles in an Aberration Corrected Transmission Electron Microscope. *J. Phys. Conf. Ser.* **2010**, *241*, 012058. <https://doi.org/10.1088/1742-6596/241/1/012058>.

- (39) Warshavski, O.; Minai, L.; Bisker, G.; Yelin, D. Effect of Single Femtosecond Pulses on Gold Nanoparticles. *J. Phys. Chem. C* **2011**, *115* (10), 3910–3917. <https://doi.org/10.1021/jp110348x>.
- (40) Wang, B.; Liu, M.; Wang, Y.; Chen, X. Structures and Energetics of Silver and Gold Nanoparticles. *J. Phys. Chem. C* **2011**, *115* (23), 11374–11381. <https://doi.org/10.1021/jp201023x>.
- (41) Almusallam, A. S.; Sholl, D. S. Brownian Dynamics Study of Polymer-Stabilized Nanoparticles. *Nanotechnology* **2005**, *16* (7). <https://doi.org/10.1088/0957-4484/16/7/015>.
- (42) Sassaroli, E.; O'Neill, B. E.; Li, K. C. P. Numerical Investigation of the Laser Heating of Gold Nanoparticles Including Thermal and Dielectric Changes in the Local Medium. In *2009 IEEE International Symposium on Biomedical Imaging: From Nano to Macro*; IEEE, 2009; pp 763–766. <https://doi.org/10.1109/ISBI.2009.5193161>.
- (43) Dallas, P.; Georgakilas, V.; Niarchos, D.; Komninou, P.; Kehagias, T.; Petridis, D. Synthesis, Characterization and Thermal Properties of Polymer/Magnetite Nanocomposites. *Nanotechnology* **2006**, *17* (8), 2046–2053. <https://doi.org/10.1088/0957-4484/17/8/043>.
- (44) Agarwal, S.; Khan, M. M. K.; Gupta, R. K. Thermal Conductivity of Polymer Nanocomposites Made with Carbon Nanofibers. *Polym. Eng. Sci.* **2008**, *48* (12), 2474–2481. <https://doi.org/10.1002/pen.21205>.
- (45) Baffou, G.; Quidant, R.; García de Abajo, F. J. Nanoscale Control of Optical Heating in Complex Plasmonic Systems. *ACS Nano* **2010**, *4* (2), 709–716. <https://doi.org/10.1021/nn901144d>.
- (46) Ghajar, Y. A. C. and A. J. *Heat and Mass Transfer: Fundamentals and Applications*, 4th ed.; The McGraw-Hill Companies: New York, 2011.
- (47) Mie, G. Contributions to the Optics of Turbid Media, Especially Colloidal Metal Solutions. *Ann. Phys.* **1908**. <https://doi.org/10.1002/andp.19083300302>.
- (48) Forcherio, G. T.; Roper, D. K. Optical Attenuation of Plasmonic Nanocomposites within Photonic Devices. *Appl. Opt.* **2013**, *52* (25), 6417–6427. <https://doi.org/10.1117/12.2062252>.
- (49) Dunklin, J. R.; Forcherio, G. T.; Roper, D. K. Geometric Optics of Gold Nanoparticle-Polydimethylsiloxane Thin Film Systems. *Opt. Mater. Express* **2014**. <https://doi.org/10.1364/OME.4.000375>.
- (50) Dunklin, J. R.; Forcherio, G. T.; Berry, K. R.; Roper, D. K. Gold Nanoparticle-Polydimethylsiloxane Thin Films Enhance Thermoplasmonic Dissipation by Internal Reflection. *J. Phys. Chem. C* **2014**, *118* (14). <https://doi.org/10.1021/jp4112124>.

- (51) Ahn, W.; Taylor, B.; Dall'Asén, A. G.; Roper, D. K. Electroless Gold Island Thin Films: Photoluminescence and Thermal Transformation to Nanoparticle Ensembles. *Langmuir* **2008**, *24* (8), 4174–4184. <https://doi.org/10.1021/la703064m>.
- (52) Baffou, G.; Quidant, R.; Girard, C. Thermoplasmonics Modeling: A Green's Function Approach. *Phys. Rev. B - Condens. Matter Mater. Phys.* **2010**. <https://doi.org/10.1103/PhysRevB.82.165424>.
- (53) Roper, D. K.; Ahn, W.; Hoepfner, M. Microscale Heat Transfer Transduced by Surface Plasmon Resonant Gold Nanoparticles. *J. Phys. Chem. C* **2007**, *111* (9), 3636–3641. <https://doi.org/10.1021/jp064341w>.
- (54) Ahn, W.; Roper, D. K. Transformed Gold Island Film Improves Light-to-Heat Transduction of Nanoparticles on Silica Capillaries. *J. Phys. Chem. C* **2008**, *112* (32), 12214–12218. <https://doi.org/10.1021/jp802497v>.
- (55) Russell, A. G.; McKnight, M. D.; Sharp, A. C.; Hestekin, J. A.; Roper, D. K. Gold Nanoparticles Allow Optoplasmonic Evaporation from Open Silica Cells with a Logarithmic Approach to Steady-State Thermal Profiles. *J. Phys. Chem. C* **2010**, *114* (22), 10132–10139. <https://doi.org/10.1021/jp101762n>.
- (56) Russell, A. G.; McKnight, M. D.; Hestekin, J. A.; Roper, D. K. Thermodynamics of Optoplasmonic Heating in Fluid-Filled Gold-Nanoparticle-Plated Capillaries. *Langmuir* **2011**, *27* (12), 7799–7805. <https://doi.org/10.1021/la200078j>.
- (57) Hoepfner, M. P.; Roper, D. K. Describing Temperature Increases in Plasmon-Resonant Nanoparticle Systems. *J. Therm. Anal. Calorim.* **2009**, *98* (1), 197–202. <https://doi.org/10.1007/s10973-009-0316-9>.
- (58) Pustovalov, V.; Astafyeva, L.; Jean, B. Computer Modeling of the Optical Properties and Heating of Spherical Gold and Silica-Gold Nanoparticles for Laser Combined Imaging and Photothermal Treatment. *Nanotechnology* **2009**, *20* (22), 225105. <https://doi.org/10.1088/0957-4484/20/22/225105>.
- (59) Garwe, F.; Bauerschäfer, U.; Csaki, A.; Steinbrück, A.; Ritter, K.; Bochmann, A.; Bergmann, J.; Weise, A.; Akimov, D.; Maubach, G.; et al. Optically Controlled Thermal Management on the Nanometer Length Scale. *Nanotechnology* **2008**, *19* (5), 055207. <https://doi.org/10.1088/0957-4484/19/05/055207>.
- (60) Zimovets, S. V.; Geshev, P. I. Nonstationary Heating of Two-Dimensional Metal Nanoparticles by Laser Radiation. *J. Eng. Phys. Thermophys.* **2008**, *81* (5), 976–984. <https://doi.org/10.1007/s10891-009-0114-z>.

**3. DYNAMIC AND EQUILIBRIUM THERMAL DYNAMIC MODES AMPLIFY
THERMAL DISSIPATION IN GOLD NANOPARTICLE-
POLYDIMETHYLSILOXANE THIN FILMS**

Keith R. Berry Jr.,^{1,†} Tyler V. Howard,^{2,†} D. K. Roper^{3,*}

¹ Ralph E. Martin Department of Chemical Engineering, University of Arkansas, Fayetteville, AR
72701

² Department of Chemistry and Physics, Southeast Missouri State University, Cape Girardeau, MO
63701

³ Department of Biological Engineering, Utah State University, Logan, UT 84322

† Authors contributed equally to manuscript

* Corresponding Author

ABSTRACT

Nanoscale plasmonic metamaterials have become a hot topic of interest in numerous multidisciplinary fields, ranging from biology with hyperthermia treatments, to optics for sensing and waveguides. Energy acquired from incident irradiation can be remitted as light or decay into phonons that propagate through the medium and result in increasing material temperatures. Previous work studied the equilibrium effects on the thermal dynamics of plasmonic metamaterials. This work studies not only the equilibrium thermal dynamics but also the effects of the dynamic portion of the material thermal dynamics on the initial cooling properties of nanocomposites at various film geometries, nanoparticle diameters and concentrations, laser irradiation powers, and position

within and adjacent to the laser spot. The dynamic cooling response of the films indicate an amplified thermal dissipation mechanism greater than bulk heat transfer means. Films of lower thicknesses containing 16 nm gold nanoparticles (AuNPs) irradiated at 13.5 mW laser power showed highest amplification and tunability of the dynamic thermal mode within and adjacent to the heat spot. Results of this work will benefit in the construction of thermal dynamic dissipation devices and the understanding of the cooling dynamics of nanocomposite materials.

3.1 Introduction

Plasmonic metamaterials containing various nanostructures have become a field of high interest and study in recent years, due to their ability to redistribute electromagnetic energy into different forms (i.e. remission, scattering, phonons, polaritons).¹⁻³ Energy from incident radiation couples with the electron cloud of the material, is reradiated and decays into phonons, before relaxing into the surrounding medium.^{4,5} These optical and thermal enhancement capabilities have been utilized in materials that facilitate increased performance in catalytic reactions,⁶ thermal ablation,⁷ sensing,⁸ and solar cells.^{9,10} Substrate composition,¹¹ nanoparticle composition^{12,13} and morphology,^{14,15} and intensity of incident light promote tunability of metamaterials containing plasmonic nanostructures.^{16,17}

Equilibrium thermal dynamic studies on the photothermal responses of plasmonic nanoparticles (NPs) have been highly characterized in various media like colloidal suspensions,⁶ polymers,¹ and ceramics.¹⁸ NPs dispersed in colloidal suspensions of various fluids (i.e. nanofluids) resulted in an increase in the thermal conductivity of the suspension,¹⁹ but the thermal response per NP decreased to near zero.²⁰ Numerical models for estimating and modeling the heat

dissipation have also been used to analyze nanofluids used in microchannels,²¹ while other models utilize the thermodynamic properties to predict the structure of materials.^{22,23} Heat exchangers and other thermodynamic components have recently been constructed using NP-containing materials in order to analyze the heat transfer properties of the materials and components.²⁴ These equilibrium thermal dynamics studies have yielded significant advances in furthering the underlying thermal responses of materials used for advancing the understanding of key thermal properties like the heating in a biological microscope.²⁵ While understanding the equilibrium thermal dynamics has been key to advancing technology and research that utilizes heat transfer, the understanding of the dynamic thermal dynamic mode is still lacking.

This work shows that the dynamic and equilibrium thermal dynamic modes of gold (Au) NPs randomly dispersed into polydimethylsiloxane (PDMS) thin films amplify the thermal dissipation within and adjacent to the heat spot during cooling after laser irradiation has ceased. A variable analysis of the film geometries, AuNP diameters and concentrations, laser irradiation powers, and the position of the pixel selected for analysis was performed to determine the variables that had the highest impact on the thermal dissipation. Observable amplification of the thermal dissipation beyond bulk polymer heat transfer were shown within the dynamic thermal mode with tunable thermal dynamics with respect to each of the aforementioned variables. Highest tunability was observed for 16 nm AuNPs in thinner polymer films at 13.5 mW laser irradiation and with the controlled selection of pixel locations within and adjacent to the heat spot. This work will serve to improve the understanding of dynamic and equilibrium thermal dynamic modes, yield higher accuracy in thermodynamic simulations, and enhance the design capabilities for solving engineering heat transfer problems.

3.2 Materials and Methods.

3.2.1 Film Fabrication and AuNP Addition.

Thin PDMS films containing AuNPs were fabricated using a recent method that increased NP content and eliminated observable gas/vapor entrapment and NP aggregation.²⁶ Briefly, dried, 16 nm poly(vinylpyrrolidone) (PVP)-coated AuNPs (Nanocomposix Inc., San Diego, CA) were dispersed into isopropanol (IPA) to 1 mg mL⁻¹ then dispersed into PDMS (Sylgard® 184 silicone elastomer kit #4019862, Dow Corning, Midland, MI) at 10¹¹-10¹² NP cm⁻³. Fabrication of AuNP-PDMS films were fabricated as followed: (1) PDMS monomer and crosslinker were mixed at a 10:1 ratio and degassed for 2 hours, (2) a volume of AuNP-IPA dispersion was added into the uncured PDMS and mixed for 1 hour, (3) a 1.5 g mass of AuNP-IPA-PDMS was poured into 25 x 25 x 1 mm polystyrene sample box and cured at 60 °C for 24 hours, and (4) sample box was wrapped in foil to prevent light-induced curing. The 16 nm AuNP containing films are shown in Figure 3.1 below. A similar procedure was followed for 76 nm AuNP-PDMS film synthesis with images of the resulting films shown in Figure S1 in Supporting Information.

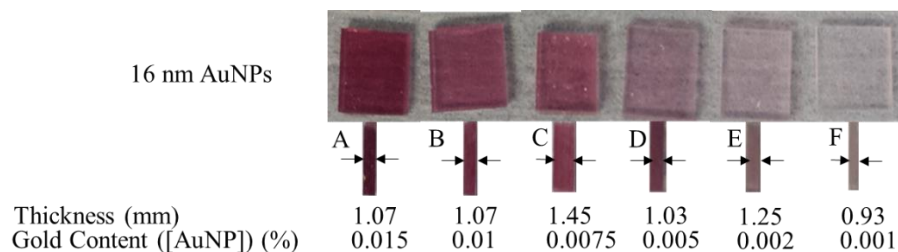


Figure 3.1. Images of the PDMS films containing 16 nm AuNPs showing corresponding concentrations and thicknesses.

3.2.2 Optical Analysis.

Spectra of the AuNP-PDMS films fabricated using the method above were captured using a spectrometer (AvaSpec-2048, Avantes, Broomfield, CO, USA). Optical properties (i.e., scattering, absorption, and extinction) of AuNP were derived via Mie theory (Mie Theory Calculator, nanoComposix, San Diego, CA, USA). Mie theory calculates the scattering, absorption and extinction of an isolated particle.

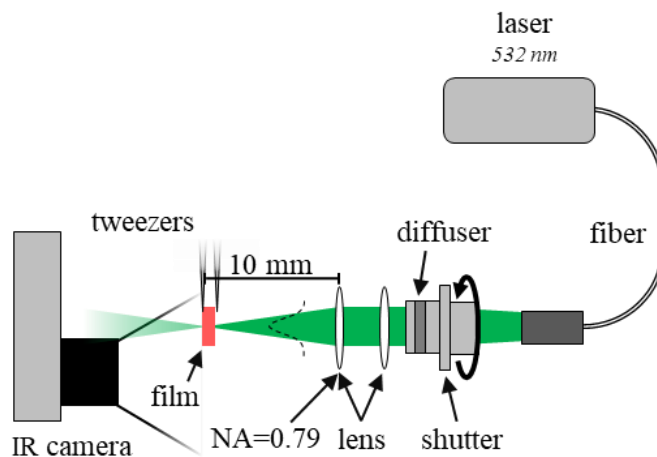


Figure 3.2. Optical setup of laser irradiation system with 532 nm light source. Laser light passed through a manual shutter and 10° ground glass diffuser to ensure a gaussian beam profile. New beam profile was then focused to an approximate 1.2 mm focal point 10 mm away from the last lens. Resulting thermal response from AuNP-PDMS films were captured via infrared (IR) camera.

3.2.3 Thermal Characterization.

AuNP-PDMS films fabricated using the above method were irradiated resonantly using a 532 nm laser (MXL-FN-532, CNI, Changchun, China) at 13.5 and 25 mW, as shown in Figure 3.2. Laser power was recorded using a power meter (PM310D, Thorlabs, Newton, NJ). Infrared images

of the AuNP-PDMS nanocomposites were captured at 5 images per second over 6 minutes (min): 0:10 min ambient conditions, 2:50 min laser irradiation, and 3:00 min cooling using an infrared thermal imaging camera (ICI 7320, Infrared Cameras Inc., Beaumont, TX). A laser shutter (SH05, Thorlabs, Newton, NJ) and shutter controller (SC10, Thorlabs, Newton, NJ) were used to open and close laser at each time interval. Each AuNP-PDMS film was mounted with tweezers to position the incident laser spot at the film top center. All power incident on the samples was contained within a laser spot with diameter of ≤ 3 mm. The thermal measurement apparatus was isolated from ambient light and forced convection by enclosure in an opaque chamber. Two or more replicates were measured.

3.2.4 Numerical Methods for Quantitative & Qualitative Analysis.

Thermal images captured during optothermal characterization were used to produce thermal micrographs on a pixel by pixel basis using MATLAB R2018a (Mathworks, Natick, MA). All subsequent analysis and image processing was performed using MATLAB. The thermal micrographs of immediate temperature changes were extracted from the raw thermal images and divided into pixelated, 0.212 cm/pixel for 16 nm AuNP at 13.5 mW and 0.116 cm/pixel for 16 and 76 nm AuNP at 25 mW, temperature heat maps. Observations of heat flow from the heat spot were shown as the change in temperature one second before ($T(I^-)$) and one second after ($T(I^+)$) laser shut off (i.e., $\Delta T = T(1^+) - T(1^-)$).

Spatial gradient of change in temperature (S) was constructed to display rate of thermal dissipation across the PDMS films. Gradients from the change in the temperature micrograph was calculated by taking half of the difference from adjacent cells, while cells on the edge was solely

the difference with the adjacent cell. Gradients were calculated in the x- (column) and y- (row) directions for each change in temperature graph and magnitude determined using Equation (1) shown below

$$S = \frac{\sqrt{\Delta T_x^2 + \Delta T_y^2}}{\max(\sqrt{\Delta T_x^2 + \Delta T_y^2})} \quad (1)$$

where ΔT_x is the gradient in the “x” direction, ΔT_y is the gradient in the “y” direction, and $\max(\dots)$ is the maximum magnitude of the gradient in a cell across all films.

Regions of interest consisting of: 3 x 3 pixels for 13.5 mW and 9 x 9 for 25 mW, were chosen for comparison of the thermodynamic properties across the film. Calculated thermal behavior for each film were determined via a dimensionless temperature driving force (theta), $\theta = (T_{\text{amb}} - T)/(T_{\text{amb}} - T_{\text{max}})$, at every pixel, where T was the measured time-varying temperature during the thermal trial. Values of maximum temperature (final 30 s of laser heating), T_{max} , and ambient temperature (first 5 s of trial for heating and last 5 s of trial for cooling), T_{amb} , were calculated at each pixel. Plotting the natural log of the driving force vs. time for a 45 s cooling period for the AuNP-PDMS films yielded the observed time constant for combined bulk heat transfer (thermal conduction, convection and radiation from film surface) at each pixel of each film.

Expected temperatures were calculated from linear relation of natural log of driving force vs. time for comparison with measured temperatures to determine effects of bulk heat transfer. Linear regression from the equilibrium portion of the natural log of theta plots were derived for observed theta values, and an expression of the driving force solved for the temperature (T). Predicted values based solely on bulk heat transfer were compared with measured values at a similar time and

percent difference taken between the two. Similar calculations were performed for each concentration and numerous regions on each film.

3.3 Results and Discussion.

3.3.1 Presence of Amplified Thermal Dissipation.

Nonlinear amplification of thermal dissipation was qualitatively observed through the change in temperature versus time and spatial gradient immediately after laser irradiation had ceased. The rate of thermal dissipation in the thermal micrographs for inside the heat spot was observed to decrease immediately after the laser was shut off, while the surrounding media showed no observable temperature change. Observations of this phenomena are shown in Figure 3.3, through pixel by pixel temperature differences in thermal micrographs one second before and after the laser was shut off in (a) and through the gradient of temperature differences from (a) using Equation (1) shown in (b). The heat spot (region of interest) was expressed in Figure 3.3 as a white square, with AuNP concentration decreasing from A (highest) to F (lowest). Pixels selected in Figure 3.3(a) for subsequent images and analysis were shown as black squares with purple dots for inside and adjacent pixels selected in a controlled manner and as a white square with a black dot for adjacent pixels selected randomly. Figure 3.3(b) shows the inside and controlled adjacent selection as white boxes and the randomly selected adjacent pixels as red boxes. Similar thermal micrographs for 16 and 76 nm AuNP films irradiated at 25 mW laser power are shown in Figures S2 and S3, respectively.

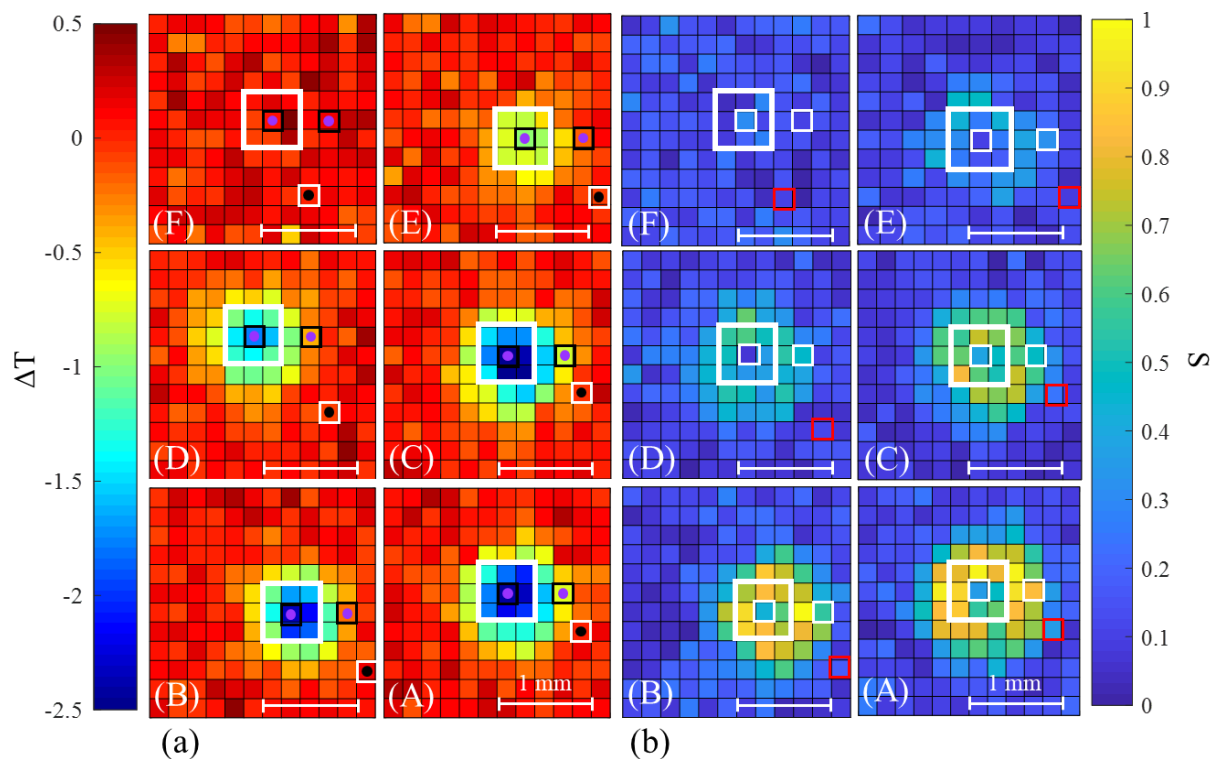


Figure 3.3. Qualitative observation of amplified heat transfer, as shown through the ΔT one second before and after shutoff shown in (a) and the spatial gradient of the change of temperature from (a) shown in (b).

Amplified heat transfer was evident through the increased temperature change shown in Figure 3.3(a) and heat flow away from the heat spot in Figure 3.3(b), which was readily observed in films A-C. The rate of temperature decrease within and adjacent to the irradiated spot once laser irradiation had ceased was significantly larger than in non-irradiated areas of each sample. This was attributable to thermal decay processes beyond bulk heat transfer via bulk conduction through the PDMS film and convective and radiative heat transfer from the film surface to the surrounding environment. The rate of temperature decrease between 16 and 76 nm AuNP films at 25 mW laser power (Figures S2 and S3, respectively) were similarly localized within the heat spot of each respective sample with the 76 nm AuNP films having lower heat loss than 16 nm AuNP films. This observable heat loss shown in Figure 3.3 was attributed to the rapid heating and cooling of

the AuNPs due to the irradiation of the AuNPs with resonant light resulting in heat dissipation propagating through the PDMS matrix as the AuNP plasmons relax. Plasmon relaxation from the AuNPs scatters the absorbed light from the incident wave into embedded PDMS polymer matrix, which allows for heat diffusion to propagate at a greater rate through the material than it would have via bulk PDMS heat transfer. Increased scattering was observed in PDMS films containing 76 nm AuNPs that yielded a lower temperature before and after the laser irradiation had ceased. PDMS films containing 16 nm AuNPs possess no scattering component according to Mie theory simulations, thus heat dissipation was greatest in the laser irradiation spot compared to the surrounding polymer matrix and resulted in a loss of heightened heat dissipation.

Figure 3.3(b) showed that as the concentration increases from films F to A, an increase in the magnitude of change in temperature (heat flow around the heat spot) was also observed through the broadening and increase in the number of yellow pixels in each micrograph. Substantial temperature changes within and adjacent to the heat spot observed in Figure 3.3 infers the impact of an internal force restricting the overall thermal dissipation of the films. Near uniform change in the temperature (Figure 3.3(a)) and gradient (Figure 3.3(b)) magnitude for film F indicated an insubstantial response in nanocomposite film after the laser was shut off and within the dissipation of the thermal energy. The magnitude of the temperature and gradient increased with concentration but were more tightly bound within the heat spot as shown in films A-D.

3.3.2 Dynamic and Equilibrium Thermal Dynamic Modes.

Amplification of the thermal dissipation was observed in initial multimodal thermal dynamic relations for the natural log of theta vs. time that was dependent on the dynamic thermal mode of

the AuNP-PDMS films as shown in Figure 3.4(a). The temperature driving force (θ) was calculated at every pixel via MATLAB and evaluated inside (Figure 3.4(b)), adjacent to (Figure 3.4(c)), and far outside (Figure 3.4(d)) the heat spot for each film. Figure 3.4(b-d) plots the slope of the dynamic thermal mode (0-3 s) and the equilibrium thermal mode (15-40 s) versus the AuNP concentration for films containing 16 and 76 nm AuNPs irradiated at 13.5 and 25 mW laser powers for pixels inside, adjacent to, and outside the heat spot. More obscure multimodal thermal dynamics in 76 nm compared to 16 nm AuNP films was a result of reduced thermal effects from insufficient plasmon resonance due to the 532 nm laser wavelength being ~ 40 nm blue-shifted from the localized surface plasmon resonance (LSPR) peak for the 76 nm AuNP films (~ 570 nm, corresponding spectra for 16 and 76 nm AuNP films shown in Figure S4). Optimal thermal heating of AuNPs occurs at the LSPR wavelength with lower temperature changes observed further from the peak wavelength as a result of lower energy absorption away from the LSPR wavelength. The observed multimodal activity decayed as time progressed before reaching an expected linear relation with time as the system reached the equilibrium thermal dynamic mode. The multimodal activity also decreased as the temperature driving force was evaluated further away from the heat spot.

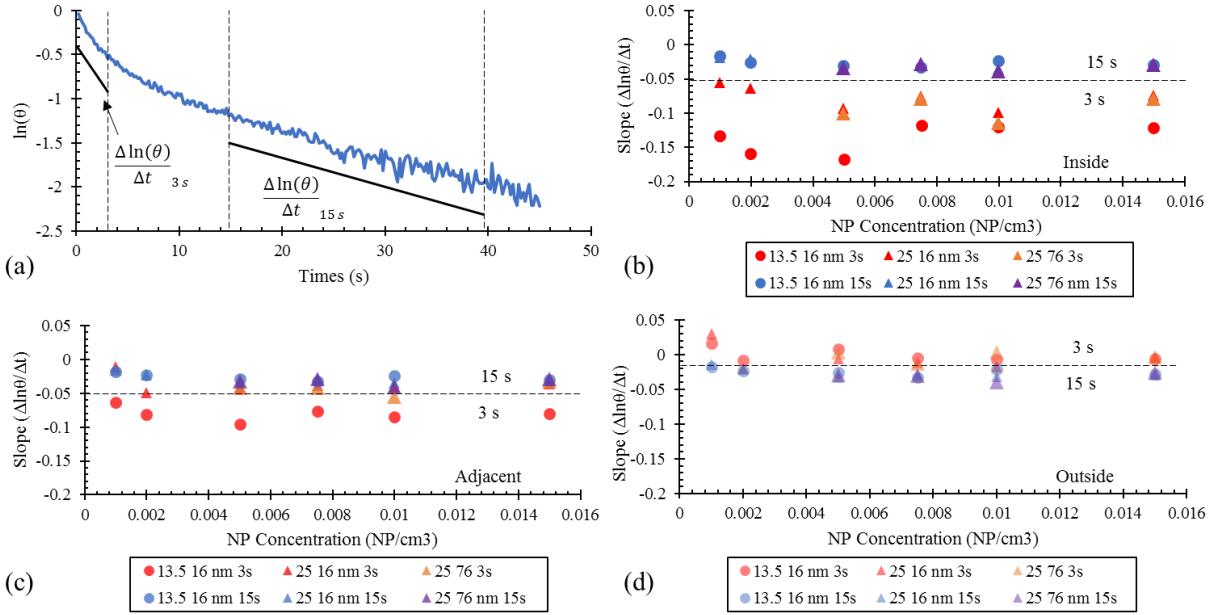


Figure 3.4. Rate of change of $\ln(\theta)$ according to time ($\Delta\ln(\theta)/\Delta t$), with slopes taken at 0-3 s (dynamic thermal mode) and 15-40 s (equilibrium thermal mode). (a) $\ln(\theta)$ versus time with slopes (black lines) plotted below quantitatively showing amplified temperature change. (b) $\Delta\ln(\theta)/\Delta t$ inside the heat spot for 0-3 and 15-40 s plotted against concentration for 16 nm AuNPs at 13.5 mW (red) and 25 mW (blue), and 76 nm AuNP for dynamic and equilibrium thermal modes. (c) $\Delta\ln(\theta)/\Delta t$ for pixels adjacent to the heat spot. (d) $\Delta\ln(\theta)/\Delta t$ for pixel outside the heat spot.

Effects of Pixel Location.

Figure 3.4(a) shows the multimodal activity of the temperature driving force with 0-3 s shown was the dynamic thermal mode, 15-40 s was the equilibrium thermal mode, and 3-15 s was the transition period between the dynamic and equilibrium thermal modes. This transition period was not observed to have significant insight into the thermal dynamics of the system and was not used for analysis. The slopes ($\Delta\ln(\theta)/\Delta t$) of the dynamic and equilibrium thermal modes were determined for inside, adjacent to, and outside of the heat spot for each of the films to determine the impact of the pixel location, AuNP diameter and concentration, and laser power shown in Figure 3.4(b-d). The slopes for pixels within the heat spot ranged from -0.05 to -0.17 for the dynamic thermal modes and -0.01 to -0.05 for the equilibrium thermal modes with a clear divide

between the dynamic and equilibrium modes observed in Figure 3.4(b) distinguished via a dashed line at a slope of -0.05. The slopes for the dynamic thermal mode resulted in ~10-fold increase compared to the slopes observed for the equilibrium thermal mode within the heat spot.

As the pixel selection moved from within the heat spot to adjacent to the heat spot (shown in Figure 3.4(c)), the clear divide observed in Figure 3.4(b) became less clear with several of the dynamic thermal mode slopes crossing the dashed line above -0.05. When a pixel well outside the heat spot was selected (shown in Figure 3.4(d)), the slopes for the dynamic thermal mode was observed above those of the equilibrium thermal mode. Films containing 16 nm AuNPs irradiated at 13.5 mW laser power generally resulted in steeper dynamic thermal mode slopes within and adjacent to the heat spot, while slopes outside the heat spot were similar to films containing 16 and 76 nm AuNPs irradiated at 25 mW. Equilibrium thermal modes within, adjacent to, and outside the heat spot resulted in similar slopes between 0 and -0.05 no matter the pixel selection, AuNP diameter, or AuNP concentration, while the dynamic thermal modes varied between 0.05 and -0.17 depending on whether the pixel selected was within, adjacent to, or outside the heat spot. Higher observable dynamic thermal mode slopes suggested additional heat dissipation beyond that of bulk heat transfer occurred within the film.

Controlled vs. Random Adjacent Pixel Selection.

The impact of the pixels selected within and outside of the heat spot appeared to be minimal, while the selection of the pixel adjacent to the heat spot appeared to have a significant impact on the resulting dynamic thermal modes for each of the films. In order to show the effect of the adjacent pixel selection more clearly, two methods for selecting the pixels were used: (1) a

controlled process where the pixel selected was in a similar location for each film as shown in Figure 3.5 with the black box containing the purple dot to the right of the white box and (2) randomly selecting pixels adjacent to the heat spot where the pixel selected for each film was in a different relative location as shown in Figure 4 with the white box containing a black dot. The selection of these pixels for analysis resulted in significantly different results between the controlled and random selection processes.

The method for determining the controlled pixel selection was by taking a 3 x 3 pixel array next to the white box outlining the heat spot and selecting the center pixel in that 3 x 3 array. This method was used for each film for the controlled pixel selection process resulting in the natural log of theta versus time plots shown in Figure 3.5(a). The purple triangle outlined in black shows the divergence in the data with films A, C, and D below the triangle and films B, E, and F above the triangle. The divergence in Figure 3.5(a) appeared to begin at ~18 s and continued to diverge at a slow rate until the 45 s cutoff was reached with the resulting slopes for the dynamic and equilibrium thermal modes showing greater correlation between data sets. This pixel selection process was used for all data and analysis throughout this work. Pixels chosen randomly did not show the same strong correlation, but instead showed no definitive features or overall discernable trends. Evidence of this was shown in the divergence and overlap of natural log of theta versus time curves shown in Figure 3.5(b). The divergence in Figure 3.5(b) appeared to start at ~30 s and diverged at a faster rate than the controlled selection in Figure 3.5(a). The overall shape of the curves in Figure 3.5(a) are similar as well, while the curves in Figure 3.5(b) vary in shape. The curves generated for the pixels chosen in a controlled manner showed a small, clear distinction between films of varying thicknesses, while pixels chosen randomly showed a large difference and

degree of overlap between films with varying thicknesses. These observations show the importance of selecting pixels in similar locations for performing thermal analysis.

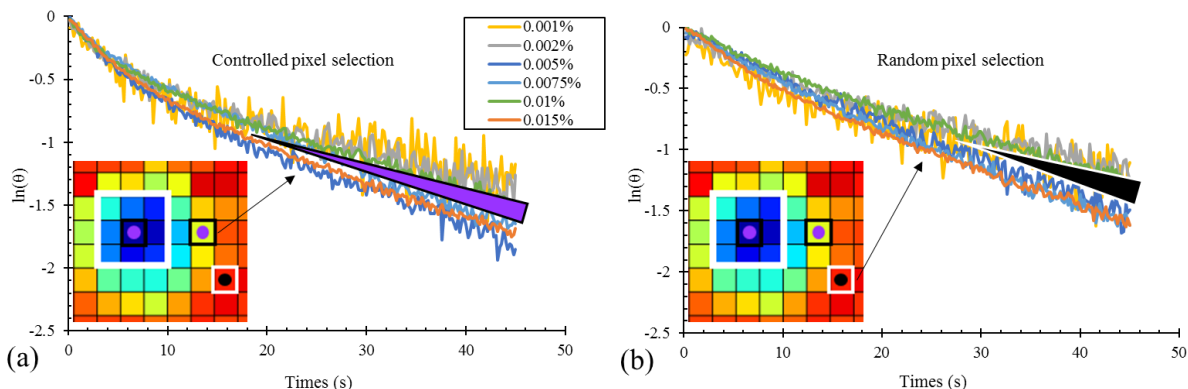


Figure 3.5. $\ln(\theta)$ graphed against time for pixels that were chosen in a controlled manner (a) against pixels chosen randomly (b). Triangle in each figure show divergence or separation in concentration highlighting importance of pixel selection when evaluating thermal effects in nanocomposite samples. (a) $\ln(\theta)$ versus time for controlled adjacent pixels and (b) $\ln(\theta)$ versus time for randomly selected.

Effects of Laser Power.

Increases in power led to a diminished effect observed in the dynamic thermal mode of the AuNP-PDMS films. Analysis of the effects of power on the AuNP-PDMS composites were limited to 16 nm AuNP films. Films containing 16 nm AuNPs were irradiated at 13.5 and 25 mW, with the slopes plotted according to the concentration for films that were approximately 1.05 mm as seen in Figure 3.6(a). Higher powers (25 mW) are shown as triangles, which on average showed a less steep slope compared to films irradiated at 13.5 mW (circles) for the dynamic thermal mode. The equilibrium thermal modes appeared to not be impacted by laser power like the dynamic thermal mode shown in Figure 3.6(a). This trend held for most films even as pixel locations were selected further away from the heat spot.

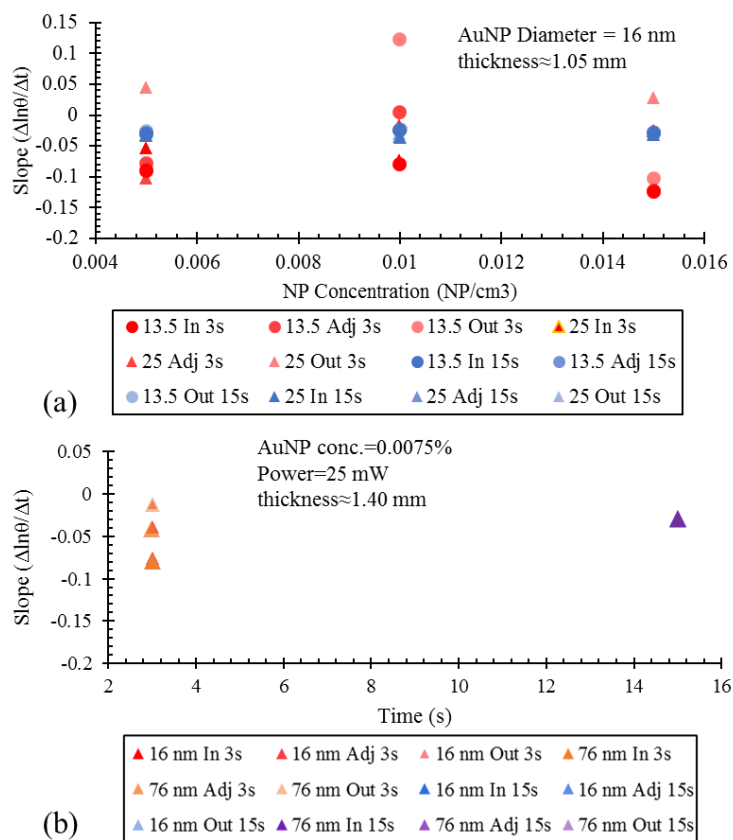


Figure 3.6. $\Delta \ln(\theta)/\Delta t$ for films that have a similar thickness for different concentrations, powers, and AuNP size. (a) Slopes given at 0-3 and 15-40 s with films that are approximately 1.05 mm. Pixels measured away from the heat spot are lighter in color. (b) $\Delta \ln(\theta)/\Delta t$ for films of similar thickness (1.40 mm), power (25 mW), and concentration (0.0075%) according to time of 0-3 and 15-40 s.

Effects of AuNP Concentration.

Concentrations with similar thickness for 16 nm AuNP films included 0.005%, 0.01%, and 0.0015%, with a thickness of around 1.05 mm as shown in Figure 3.6(a). Comparison of the dynamic thermal mode slopes showed an increase in the steepness of the slopes within the heat spot as the concentration increased. When transitioning from the dynamic thermal mode to the

equilibrium thermal mode, the effect diminishes resulting in similar slope values across all concentrations, laser powers, and pixel locations.

Effects of Film Thickness.

Evaluation of impact of thickness on the AuNP-PDMS thermal dynamics followed trends as reported by Roper et al.²⁶ Thicknesses for 16 nm AuNPs ranged from 0.93 to 1.45 mm, with greater thickness resulting in a diminished heat dissipation while in the dynamic mode. Figure 3.6 shows 16 nm AuNPs in films at lower thicknesses (Figure 3.6(a)) and 16 and 76 nm AuNPs in films at larger thicknesses (Figure 3.6(b)) for various concentrations, which shows that at larger thicknesses the distribution of slopes between pixels was much lower (-0.1 to 0) than for films with lower thicknesses (-0.12 to 0.12). While keeping the thickness constant and varying the concentration in Figure 3.6(a) showed an increase in the steepness of the dynamic thermal mode slopes, Figure 3.7 showed that as the thickness was varied the steepness of the dynamic thermal mode slopes decreased. This trend of larger thicknesses reducing thermal dynamics matched results reports by Roper. et al.²⁶ However, as pixels are observed farther away from the heat spot, the effect disappears, with slope values approaching a more consistent value. Thermal dissipation within the dynamic thermal mode occurs primarily within the heat spot due to direct laser irradiation, while outside the heat spot the AuNPs are heated via scattering of the laser light from AuNPs within the heat spot through internal reflection as reported by Dunklin et al.²⁷

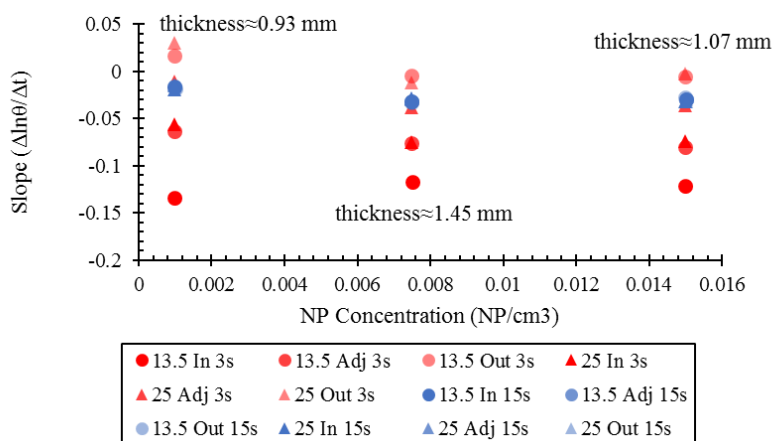


Figure 3.7. $\Delta \ln(\theta)/\Delta t$ for 16 nm AuNP films of varying thickness and concentration. Thicknesses range from 0.93 to 1.45 mm with concentrations varying from 0.001% to 0.015%.

3.3.3 Amplified Thermal Excitation.

Multimodal activity generated from greater change of temperature in time was shown to be influenced by radial distance from heat spot, AuNP size and concentration, and irradiation power. The temperature driving force was expressed through a linear relationship of conduction of the thermal energy in the PDMS film, yet the presence of multimodal activity shows a non-linear relation.¹⁶ Inclusion of non-linear dependence leads to miscalculations in the thermal dissipation rates (i.e., tau values of the AuNP-PDMS films). Multimodal activity observed in the natural log of theta vs. time graphs indicated that the AuNPs were acquiring more thermal energy than assumed through initial equations and purely conductive means. Back calculation of the expected temperature for pixels within the heat spot resulted in measured temperatures greater than calculated values and was dependent on the concentration of AuNPs in the PDMS film. Percent difference values of expected and measured temperatures were calculated as $\% \text{ diff} =$

$$\frac{|T_{est} - T_{meas}|}{T_{est} + T_{meas}} * 200 \text{ where } T_{est} \text{ was the estimated, or calculated, temperature value based on the linear}$$

interpolation of natural log of theta versus time and T_{meas} was the measured temperature from thermal excitation. Visual representation of this process and comparison was shown in Figure 3.8(a). Percent difference values of expected against measured temperatures ranged from 0.36 to 2.16%, 0.13 to 1.20%, and 0.033 to 0.40%, within, adjacent to, and outside the heat spot, respectively, for 16 nm AuNP-PDMS films irradiated at 13.5 mW. A similar trend was observed in the 16 nm AuNPs irradiated at 25 mW and 76 nm. Results are shown in Figure 3.8(b)-(d).

Accuracy between measured and calculated temperature values decreased as pixels were radial observed farther away from the heat spot. Expected and measured temperature values were found to have closer agreement as pixels were analyzed farther from the heat source. Comparison of Figure 3.8(b)-(d) demonstrated this phenomenon as difference values were less than 0.4 % for all AuNP concentrations irradiated at all powers. Percent difference values increased as observed pixels approached the heat spot with maximum values ranging from nearly 1.13 to 2.16 % across all AuNP-PDMS films. Calculated and measured temperature values were influenced by not only AuNP concentrations but also laser power and AuNP diameter. Difference values for pixels within the heat spot increased from 0.36 % to 2.16 % for 16 nm AuNP at 13.5 mW, 0.21 % to 1.69 % for 16 nm AuNP at 25 mW, and 0.49 % to 1.13 % for 76 nm AuNPs. The increasing trend in difference of expected and measured values matched bulk temperatures rising with greater AuNP concentrations, implying that bulk thermal effects of AuNPs contributed to greater inaccuracy of the temperature values.

Saturation of AuNP from incident irradiation was shown to influence relation of agreement between measured and expected temperature values approaching the heat spot. Results from plasmon resonance of 16 nm AuNP at 25 mW showed a nearly linear relation with difference values and AuNP concentrations. Temperature difference values for pixels outside the heat spot

increased from 0.043 % to 0.37 % while pixels adjacent to the heat spot rose from 0.065 % to 0.45 % and pixels inside the heat spot ranged from 0.20 % to 1.27 %. Linear trends observed in all pixel locations suggested that the saturation of AuNPs impacted the thermal behavior of the AuNP-PDMS films. AuNPs irradiated with a continuous laser at 25 mW were believed to have become saturated, or resonance of AuNP plasmon reaches a maximum amplitude, while AuNPs at 13.5 mW were unsaturated. The maximum resonance effects maximum heat generated in the AuNP system leading to only increase in difference and temperatures at greater AuNP concentrations, which was not observed in the 16 nm AuNP at 13.5 mW.

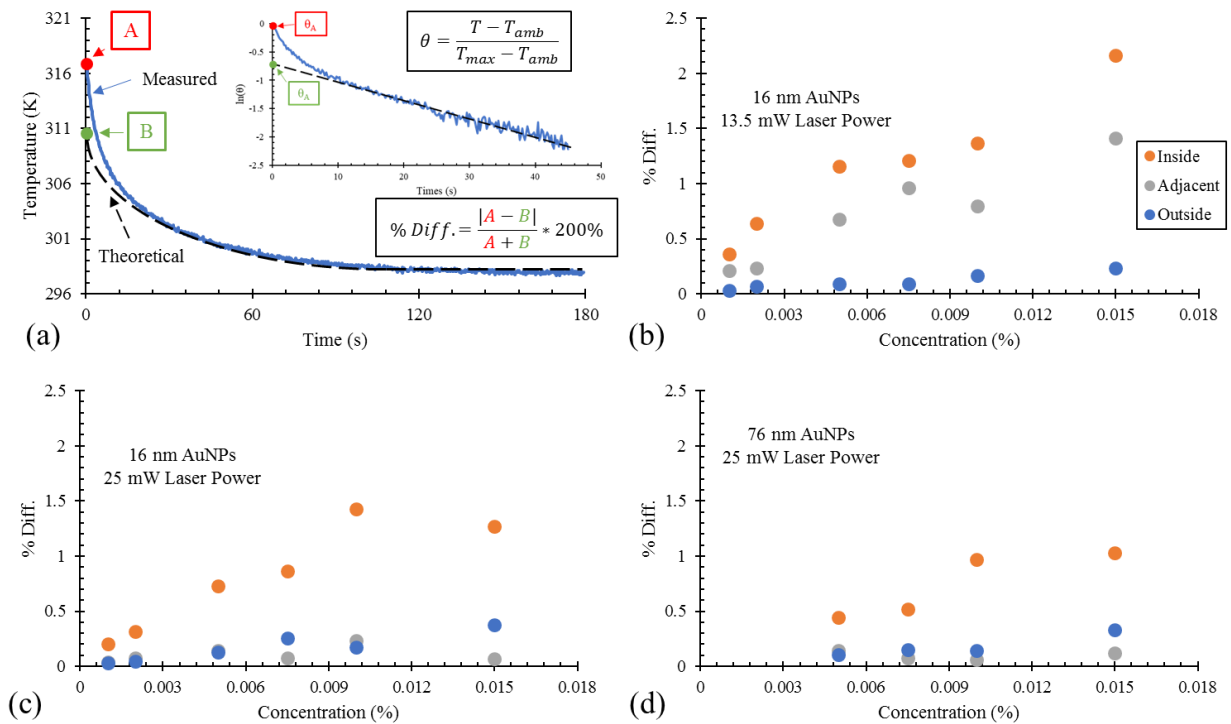


Figure 3.8. Comparison of measured against theoretically back calculated temperatures for analyzed pixels. (a) Temperature curve against time with measured temperature (red) and theoretical (green) with inset of $\ln(\theta)$ graph demonstrating calculation of theoretical value. Percent difference of theoretical and measured temperature values shown with increasing concentrations for 16 nm AuNP films at 13.5 mW (b), 16 nm AuNP at 25 mW (c), and 76 nm AuNP at 25 mW (d).

3.4 Conclusions.

This work shows that the dynamic portion of the material thermal dynamics was impacted by the film geometries, nanoparticle diameters and concentrations, laser irradiation powers, and position within and adjacent to the laser spot. The dynamic cooling response of the films showed an amplified thermal dissipation mechanism greater than bulk heat transfer means was present resulting in multimodal activity observed within the natural log of the temperature driving force versus time plots. This activity was most evident in films of lower thicknesses containing 16 nm gold nanoparticles (AuNPs) irradiated at 13.5 mW laser power within and adjacent to the heat spot. These multimodal cooling thermodynamics derived from the temperature driving force were a result of additional heat dissipation from convective and radiation through the bulk nanocomposite matrix. The multimodal activity observed in the 76 nm AuNPs were from optical scattering, while similar behavior observed in 16 nm AuNPs were due to the enhanced dynamic thermal mode. The response of the dynamic thermal mode was most affected by the film thickness, AuNP concentration, and pixel location.

3.5 Author Information

Corresponding author

* E-mail: Keith.Roper@usu.edu, phone: (801) 891-8921.

Author Contributions

K. Berry Jr. performed data analysis for 25 mW laser power data, refined figures, drafted part of manuscript text, and revised final version of the manuscript text. T. V. Howard performed optothermal measurements and data analysis for 13.5 mW laser power data, drafted figures, and drafted part of manuscript text. D. K. Roper derived the approach, directed the work, and finalized the manuscript text.

3.6 Acknowledgements.

This work was supported in part by NSF CBET-1134222, NSF ECCS-1006927, the University of Arkansas Foundation, and the Walton Family Charitable Foundation. This work was also supported in part by the Center for Advanced Surface Engineering (CASE), under the National Science Foundation (NSF) Grant No. OIA-1457888 and the Arkansas EPSCoR Program. D. K. Roper also acknowledges support from Utah State University. Any opinions, findings, and conclusions or recommendations expressed in this material are those of the authors and do not necessarily reflect the views of the National Science Foundation. The authors would like to thank Caitlyn Chambers for performing initial optothermal measurements for 25 mW laser powers and Dr. Jeremy Dunklin for fabricating films used in this manuscript.

CONFLICTS OF INTEREST.

There are no conflicts of interest to declare.

3.7 References.

- (1) Berry, K. R.; Russell, A. G.; Blake, P. T.; Roper, D. K. Gold Nanoparticles Reduced in Situ and Dispersed in Polymer Thin Films: Optical and Thermal Properties. *Nanotechnology* **2012**, *23* (37), 11. <https://doi.org/10.1088/0957-4484/23/37/375703>.
- (2) Bozlar, M.; He, D.; Bai, J.; Chalopin, Y.; Mingo, N.; Volz, S. Carbon Nanotube Microarchitectures for Enhanced Thermal Conduction at Ultralow Mass Fraction in Polymer Composites. *Adv. Mater.* **2010**, *22* (14), 1654–1658. <https://doi.org/10.1002/adma.200901955>.
- (3) Dunklin, J. R.; Forcherio, G. T.; Berry, K. R.; Roper, D. K. Asymmetric Reduction of Gold Nanoparticles into Polydimethylsiloxane Thin Films. *ACS Appl. Mater. Interfaces* **2013**, *5*, 8457–5466. <https://doi.org/10.1021/am4018785>.
- (4) Li, T.-L.; Hsu, S. L.-C. Enhanced Thermal Conductivity of Polyimide Films via a Hybrid of Micro- and Nano-Sized Boron Nitride. *J. Phys. Chem. B* **2010**, *114* (20), 6825–6829.
- (5) Urban, A. S.; Carretero-Palacios, S.; Lutich, A. A.; Lohmüller, T.; Feldmann, J.; Jäckel, F. Optical Trapping and Manipulation of Plasmonic Nanoparticles: Fundamentals, Applications, and Perspectives. *Nanoscale* **2014**, *6* (9), 4458. <https://doi.org/10.1039/c3nr06617g>.
- (6) Ishii, S.; Sugavaneshwar, R. P.; Nagao, T. Titanium Nitride Nanoparticles as Plasmonic Solar Heat Transducers. *J. Phys. Chem. C* **2016**, *120* (4), 2343–2348. <https://doi.org/10.1021/acs.jpcc.5b09604>.
- (7) Wang, S.; Riedinger, A.; Li, H.; Fu, C.; Liu, H.; Li, L.; Liu, T.; Tan, L.; Barthel, M. J.; Pugliese, G.; et al. Plasmonic Copper Sulfide Nanocrystals Exhibiting Near-Infrared Photothermal and Photodynamic Therapeutic Effects. *ACS Nano* **2015**, *9* (2), 1788–1800. <https://doi.org/10.1021/nn506687t>.
- (8) Thepudom, T.; Lertvachirapaiboon, C.; Shinbo, K.; Kato, K.; Kaneko, F.; Kerdcharoen, T.; Baba, A. Surface Plasmon Resonance-Enhanced Photoelectrochemical Sensor for Detection of an Organophosphate Pesticide Chlorpyrifos. *MRS Commun.* **2018**, *8* (1), 107–112. <https://doi.org/https://doi.org/10.1557/mrc.2017.131>.
- (9) Wang, X.; He, Y.; Liu, X.; Shi, L.; Zhu, J. Investigation of Photothermal Heating Enabled by Plasmonic Nanofluids for Direct Solar Steam Generation. *Sol. Energy* **2017**, *157*, 35–46. <https://doi.org/10.1016/j.solener.2017.08.015>.
- (10) Chen, M.; Wu, Y.; Song, W.; Mo, Y.; Lin, X.; He, Q.; Guo, B. Plasmonic Nanoparticle-Embedded Poly(p-Phenylene Benzobisoxazole) Nanofibrous Composite Films for Solar Steam Generation. *Nanoscale* **2018**, *10* (13), 6186–6193. <https://doi.org/10.1039/c8nr01017j>.

- (11) Dixon, S. C.; Peveler, W. J.; Noor, N.; Bear, J. C.; Parkin, I. P. Superhydrophobic Au/Polymer Nanocomposite Films via AACVD/Swell Encapsulation Tandem Synthesis Procedure. *RSC Adv.* **2016**, *6* (37), 31146–31152.
- (12) Hoepfner, M. P.; Roper, D. K. Describing Temperature Increases in Plasmon-Resonant Nanoparticle Systems. *J. Therm. Anal. Calorim.* **2009**. <https://doi.org/10.1007/s10973-009-0316-9>.
- (13) Lalis, A.; Tessier, G.; Plain, J.; Baffou, G. Plasmonic Efficiencies of Nanoparticles Made of Metal Nitrides (TiN, ZrN) Compared with Gold. *Sci. Rep.* **2016**, *6* (December), 1–11. <https://doi.org/10.1038/srep38647>.
- (14) Ahn, W.; Zhao, X.; Hong, Y.; Reinhard, B. M. Optoplasmonic Networks with Morphology-Dependent near- and Far-Field Responses. *MRS Commun.* **2015**, *5* (4), 579–586. <https://doi.org/10.1557/mrc.2015.78>.
- (15) Chin, C. D.-W.; Akbarian-Tefaghi, S.; Reconco-Ramirez, J.; Wiley, J. B. Rapid Microwave Synthesis and Optical Activity of Highly Crystalline Platinum Nanocubes. *MRS Commun.* **2018**, *8* (1), 71–78. <https://doi.org/10.1557/mrc.2017.137>.
- (16) Roper, D. K.; Ahn, W.; Hoepfner, M. Microscale Heat Transfer Transduced by Surface Plasmon Resonant Gold Nanoparticles. *J. Phys. Chem. C* **2007**, *111* (9), 3636–3641. <https://doi.org/10.1021/jp064341w>.
- (17) Chen, J.; Walther, J. H.; Koumoutsakos, P. Ultrafast Cooling by Covalently Bonded Graphene-Carbon Nanotube Hybrid Immersed in Water. *Nanotechnology* **2016**, *27* (46), 465705. <https://doi.org/10.1088/0957-4484/27/46/465705>.
- (18) Ann, W.; Roper, D. K. Transformed Gold Island Film Improves Light-to-Heat Transduction of Nanoparticles on Silica Capillaries. *J. Phys. Chem. C* **2008**, *112* (32), 12214–12218. <https://doi.org/10.1021/jp802497v>.
- (19) Alawi, O. A.; Mallah, A. R.; Kazi, S. N.; Sidik, N. A. C.; Najafi, G. Thermophysical Properties and Stability of Carbon Nanostructures and Metallic Oxides Nanofluids: Experimental Approach. *J. Therm. Anal. Calorim.* **2019**, *135* (2), 1545–1562. <https://doi.org/10.1007/s10973-018-7713-x>.
- (20) Howard, T. V.; Dunklin, J. R.; Forcherio, G. T.; Roper, D. K. Thermoplasmonic Dissipation in Gold Nanoparticle–polyvinylpyrrolidone Thin Films. *RSC Adv.* **2017**, *7* (89), 56463–56470. <https://doi.org/10.1039/C7RA03892E>.
- (21) Keshavarz Moraveji, M.; Barzegarian, R.; Bahiraei, M.; Barzegarian, M.; Aloueyan, A.; Wongwises, S. Numerical Evaluation on Thermal–hydraulic Characteristics of Dilute Heat-Dissipating Nanofluids Flow in Microchannels: Comparison of Different Models. *J. Therm. Anal. Calorim.* **2019**, *135* (1), 671–683. <https://doi.org/10.1007/s10973-018-7181-3>.

- (22) Berry, K. R.; Dunklin, J. R.; Blake, P. A.; Roper, D. K. Thermal Dynamics of Plasmonic Nanoparticle Composites. *J. Phys. Chem. C* **2015**, *119* (19). <https://doi.org/10.1021/jp512701v>.
- (23) Samsonov, V. M.; Bembel, A. G.; Kartoshkin, A. Y.; Vasilyev, S. A.; Talyzin, I. V. Molecular Dynamics and Thermodynamic Simulations of Segregation Phenomena in Binary Metal Nanoparticles. *J. Therm. Anal. Calorim.* **2018**, *133* (2), 1207–1217.
- (24) Moradi, A.; Toghraie, D.; Isfahani, A. H. M.; Hosseinian, A. An Experimental Study on MWCNT–water Nanofluids Flow and Heat Transfer in Double-Pipe Heat Exchanger Using Porous Media. *J. Therm. Anal. Calorim.* **2019**, 1–11.
- (25) Frivaldsky, M.; Pavelek, M. Development of Temperature Stabilization System for Biological Sample's Microscope. *J. Therm. Anal. Calorim.* **2019**, 1–12.
- (26) Roper, D. K.; Berry, K. R.; Dunklin, J. R.; Chambers, C.; Bejugam, V.; Forcherio, G. T.; Lanier, M. Effects of Geometry and Composition of Soft Polymer Films Embedded with Nanoparticles on Rates for Optothermal Heat Dissipation. *Nanoscale* **2018**. <https://doi.org/10.1039/c8nr00977e>.
- (27) Dunklin, J. R.; Forcherio, G. T.; Keith Roper, D. Gold Nanoparticle-Polydimethylsiloxane Films Reflect Light Internally by Optical Diffraction and Mie Scattering. *Mater. Res. Express* **2015**, *2* (8), 085005. <https://doi.org/10.1088/2053-1591/2/8/085005>.

4. CONTROLLED GOLD NANOPARTICLE PLACEMENT INTO PATTERNED POLYDIMETHYLSILOXANE THIN FILMS VIA DIRECTED SELF-ASSEMBLY

Keith R. Berry Jr.¹, Ricardo L. Romo², Megan Mitchell¹, Vinith Bejugam³, and D. Keith Roper^{4,*}

¹ Ralph E. Martin Department of Chemical Engineering, University of Arkansas, Fayetteville, AR 72701, USA

² Microelectronics-Photonics Graduate Program, University of Arkansas, Fayetteville, AR 72701, USA

³ PacTech, Packaging Technologies, Santa Clara, CA 95090 USA

⁴ Department of Biological Engineering, Utah State University, Logan, UT 84322, USA

* Corresponding Author

ABSTRACT

The scalable and reproducible assembly of nanoparticles (NPs) into organized structures, e.g., ordered arrays, economically and with high fidelity remains a fundamental roadblock. Current methods to fabricate ordered arrays of NPs like directed self-assembly have shown the highest promise with >85% density of filled prepatterned polymer cavities containing NPs. This work refines directed self-assembly by controlling the evaporation rate, substrate velocity (deposition rate), and NP diameter resulting in reproducible fabrication of ordered arrays with areas >2 mm x 2 mm and ~100% density of filled cavities. Localized surface plasmon resonance (LSPR) and surface lattice resonance (SLR) measured extinction peak locations blue shifted, and the peak heights increased as the NP density increased for both 100 and 150 nm gold (Au) NPs. Discrete dipole approximation (DDA), coupled dipole approximation (CDA), rapid semi-analytic CDA

(rsa-CDA), and Mie theory simulations closely matched extinction per nanoparticle (extinction/NP) calculations for measured extinction spectra. An ordered array containing 150 nm AuNPs was spectroscopically characterized, transferred to glass, spectroscopically characterized again, and then compared to rsa-CDA estimates using both polydimethylsiloxane (PDMS) and glass refractive indices (RI). This comparison showed peak location estimates matched within 1.7% and had comparable relative increases in peak heights. Both the measured and simulated SLR peak height was shown to significantly increase when the array was on glass as opposed to within PDMS.

Keywords: nanoparticle arrays, directed self-assembly, lattice resonances, plasmon resonances, gold nanoparticles

4.1 Introduction

Gold (Au) nanoparticles (NPs) exhibit localized surface plasmon resonance (LSPR) through conduction-electron oscillations when an external electromagnetic (EM) field is applied.¹⁻³ When the AuNPs are ordered into a square lattice and exposed to an external EM field, the LSPRs on each individual particle couple with light diffracted from the ordered arrangement resulting in a surface lattice resonance (SLR), i.e. Fano resonance or coupled lattice resonance (CLR), spectral feature corresponding to the lattice spacing.³⁻¹⁰ SLR features can be tuned by varying the lattice spacing, NP geometry, incident EM field intensity, and the refractive index (RI).^{8,9,11-16} Simulations, such as plasmon hybridization, coupled dipole approximation (CDA), rapid semi-analytic CDA (rsa-CDA), finite-difference time-domain (FDTD), and Fano theory, have been used

to estimate both the LSPR and SLR peak locations, peak heights, scattering amplitudes, and scattering cross-sections.^{5,7,10,17-19}

Popular commercial microfabrication techniques, such as electron beam lithography (EBL), nanoimprint lithography (NIL), laser ablation (LA), and focused ion beam (FIB), have been used to produce random and ordered assemblies of AuNPs.^{12,20-24} Recent advances in the fabrication of ordered arrays include thermal evaporation, dip-coating self-assembly, template-assisted self-assembly, and directed self-assembly.^{4,19,25-35} In particular, a variety of self-assembly techniques have been developed and employed to cost-effectively fabricate arrays of AuNPs. These techniques range from receding contact line, i.e. meniscus moving, approaches (the solution is between a fixed glass superstrate and a fixed substrate where evaporation controls the deposition of AuNPs) to fixed glass superstrates with moving substrates (the solution between a fixed glass superstrate and a substrate attached to a linear translation stage where evaporation and the rate of substrate motion controls the deposition).^{26,30,30-32} These advances offer economically scalable approaches to fabricate ordered arrays of AuNPs, but a reproducible approach that can produce high density, millimeter-scale areas with single AuNP per cavity is lacking.

This work introduces a refined directed self-assembly process for fabricating ordered arrays of AuNPs yielding >2 mm x 2 mm areas of ~100% density of filled prepatterned polydimethylsiloxane (PDMS) cavities containing one NP per cavity. Extinction spectra and extinction per NP (extinction/NP) values showed blue-shifting of the LSPR and SLR peaks as the density of AuNPs increased. Mie theory and DDA closely matched measured values for extinction/NP for LSPR peaks of both 100 and 150 nm AuNPs. CDA and rsa-CDA resulted in greater differences between measured extinction/NP values but closely matched the measured peak locations for both LSPR and SLR for 150 nm AuNPs. Discrepancies between these simulated

results for CDA and measured results were likely a function of RI because the measured values were surrounded by air, water, Triton X-100, and PDMS while simulated values assumed only PDMS surrounded the AuNPs. An ordered array containing 150 nm AuNPs was spectroscopically characterized before being transferred onto a glass slide and spectroscopically characterized again. rsa-CDA simulations were performed using PDMS and glass RI and compared to the measured spectra, which showed that peak locations for LSPR, quadrupole, and SLR features matched within 1.7%. Relative increases in peak heights also closely matched for rsa-CDA simulation and measured extinction spectra.

4.2 Materials and Methods

4.2.1 Fabrication of 2-D array stamps.

Silicon (Si) master stamps lithographed with a square lattice of posts at a 600 nm pitch (150 nm post height; 195 nm post diameter) were purchased from Lightsmyth Technologies (Eugene, OR., S2D-24B2-0808-150-P). Polydimethylsiloxane (PDMS) monomer and curing agent (Sylgard 184 silicone elastomer kit; #240 401 9862) were purchased from Dow Corning Corporation (Midland, MI). Monomer and curing agent were mixed at a 10:1 monomer:crosslinker ratio at 3000 rpm for 6 minutes in a speed mixer purchased from FlackTek Inc. (#DAC 150SP/601 0064, Landrum, SC). The mixture was then degassed until observable air bubbles were removed (5-25 minutes) and poured onto a pre-rinsed (acetone + water) Si stamp and cured for 15 min at 180 °C. Cured PDMS templates with 600-nm cavity arrays were peeled away from the Si stamp. PDMS arrayed-cavity stamp thickness averaged 300 μm .

4.2.2 Solution Preparation.

Triton X-100 purchased from Sigma Aldrich (St. Louis, MO) was diluted to 1 weight (wt) % in DI water and nitrogen capped (nitrogen gas was blown into the vessel for ~1 min) to remove air bubbles. 100 and 150 nm citrate-stabilized AuNPs (Stock: 6 and 6.4 mg/mL, respectively) purchased from Nanopartz (Loveland, CO) were diluted to 3 and 3.2 mg/mL, respectively, in 1 wt % Triton X-100. The solution was nitrogen capped to remove air bubbles.

4.2.3 Stage Preparation.

A substrate with a cavity (see Figure 4.1) was built using glass slides (VWR, 16004-430) to support and translocate the stamp and slow evaporative AuNP deposition. The substrate consisted of a 2 in x 3 in single glass slide base (Premiere, 6101) supporting four glass slide walls (VWR, 16004-430) forming a 4 mm x 20 mm cavity with a depth of ~1 mm in the center as shown in Figure 4.1(a-d). The walls were one glass slide thick (1 mm) and were cut using a diamond knife and then attached to the base using epoxy resin (Loctite, heavy duty). The substrate was attached via carbon tape to a motorized syringe pump (KD Scientific, KDS-100) as shown in Figure 4.1(c). A fixed superstrate was built by using superglue (Loctite, Super Glue Gel) to attach a 2 mm x 2 mm glass slide with a thickness of 1 mm (VWR, 16004-430) that was cut with a diamond knife to a second 1 in x 3 in glass slide for high evaporation experiments (Figure 4.1(a)) or a 2 in x 3 in single glass slide for low evaporation experiments (Figure 4.1(b)). The purpose of this 2 mm x 2 mm glass slide was to facilitate contact line pinning of the NP solution on the PDMS arrayed-cavity stamp as shown in Figure 4.1(d). The 2 mm x 2 mm glass slide on the 2 in x 3 in slide for

low evaporation experiments was surrounded by a single layer of glass coverslips (Corning, 2845-18, 0.12-0.16 mm thickness) that were spaced ~5 mm from each side of the 2 mm x 2 mm slide as shown in Figure 4.1(e). The superstrate was then attached to a 3-axis positioner (Line Tools Company, Model A-LH) so that the 2 mm x 2 mm glass slide could be lowered into the 4 mm x 20 mm cavity containing the stamp.

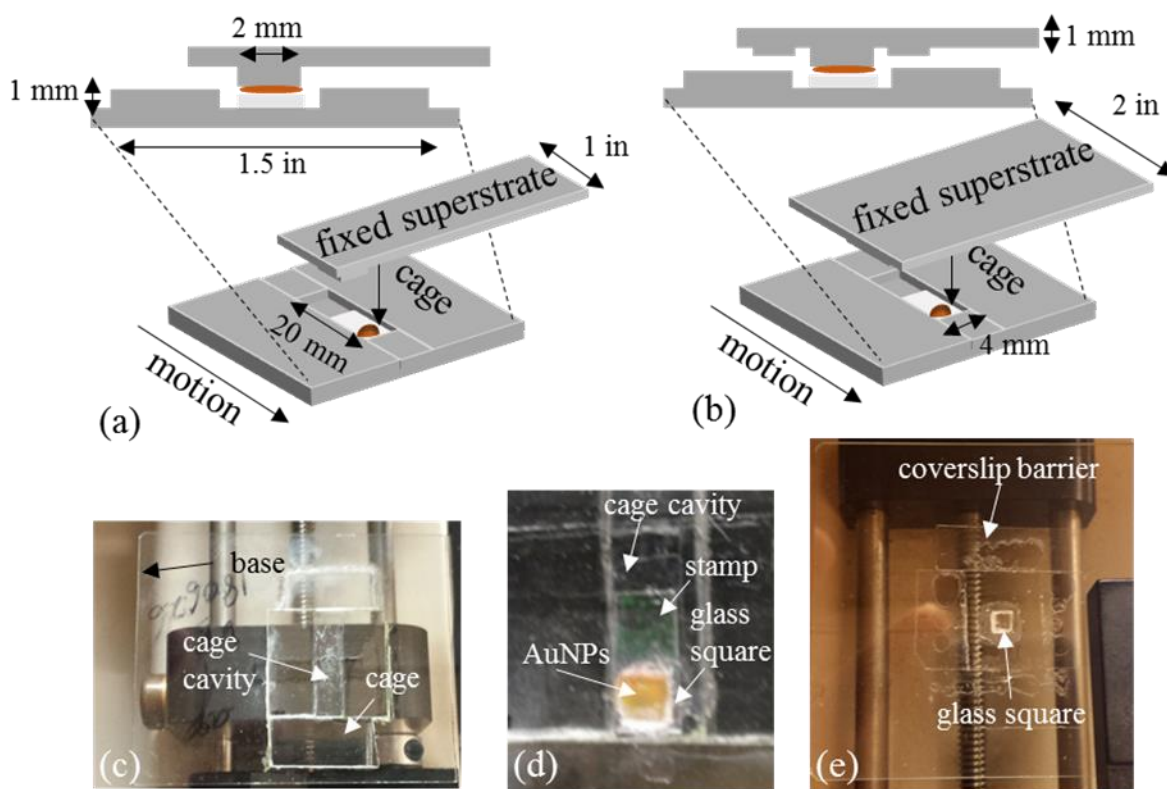


Figure 4.1 Schematic of directed self-assembly stage setup used for (a) high evaporation and (b) low evaporation experiments. (c) Shows the location on the syringe pump where the cage is attached. (d) Shows an example of a drop of AuNPs pinned by the fixed superstrate at the beginning of a high evaporation self-assembly experiment. (e) Shows the superstrate used for the low evaporation self-assembly experiments.

4.2.4 Gold Nanoparticle Deposition.

The PDMS arrayed-cavity stamp was cut in half using a razorblade so that two experiments could be performed with each stamp. A half-stamp was placed inside the substrate cavity and a 2.5 μL drop of 1 wt.% Triton X-100 in DI water was added to the bottom center of the stamp. The superstrate was then lowered into position so that the drop pinned to the 2 mm x 2 mm glass slide and lowered until it spread and pinned to all four sides of the slide (as shown in Figure 4.1(a,d)). The linear stage was then set to 8.0 $\mu\text{m/s}$. A cardboard box was placed over the system to minimize evaporation due to ambient light and convection. This process acted as a pre-coat to increase AuNP deposition. Once the pre-coat was finished (~ 15 min), a 2.5 μL drop of 3 (100 nm AuNPs) or 3.2 mg/mL (150 nm AuNPs) in 1 wt.% Triton X-100 was placed in the same position and the superstrate was lowered until the drop pinned on all four sides of the glass slide. The linear stage was set at rates ranging from 2.1 $\mu\text{m/s}$ to 1.2 $\mu\text{m/s}$.

4.2.5 Optical Characterization.

Transmission spectra of each AuNP ordered array was measured using a light microscope (Eclipse LV100, Nikon Instruments, Melville, New York) integrated with a UV-Vis spectrometer (Shamrock 303, Andor Technology, Belfast, UK). Extinction amplitudes for both LSPR and SLR peaks were taken using a tangent line corresponding to each peak. The extinction was normalized by setting the valley before the SLR peak to 0.01 A.U. for the extinction of each AuNP array. Dark-field microscopic images were captured at 20x and 100x objectives using the same light microscope used for the spectral characterization.

4.2.6 Rapid Semi-Analytical Coupled Dipole Approximation (rsa-CDA) Simulations.

Rapid semi-analytical coupled dipole approximation (rsa-CDA) was performed to determine estimated spectral peak locations for arrays of AuNPs with a diameter of 150 nm using a previously developed method.^{5,36,37} Briefly, this configuration treats each AuNP as a single dipole point with a dipole polarizability of, α . The NPs were arranged in a 2D square lattice with an array dimension of 301 x 301 and a lattice constant, distance from the center of one NP to the adjacent NP, set at 600 nm. The simulation was performed across a wavelength range of 500-950 nm for refractive indices (RI) of PDMS (1.42) and glass (1.52). The simulation outputs extinction efficiencies across the spectral range. The primary observable features were the SLR peak, the LSPR peak, and the quadrupole peak (150 nm only).

4.2.7 Discrete Dipole Approximation (DDA) and CDA Simulations.

Discrete dipole approximation (DDA) simulations were performed in a 12-core supercomputer node with 64 GB memory for 500 to 950 nm PDMS (1.42) wavelengths and a resolution of 5 nm. Target and parameter files for DDSCAT 7.3 were generated, using a custom-made MATLAB tool available on nanoHUB,³⁸ for 100 and 150 nm diameter AuNPs. The generated spectra for a single AuNP was output into Microsoft Excel for further analysis and real and imaginary parts of the polarizability were stored for ordered array simulations. The polarizability data was then imported into MATLAB for CDA to generate a 301 x 301 array of AuNPs with a lattice spacing of 600 nm in PDMS (1.42). The generated spectra for both 100 nm and 150 nm diameter AuNP arrays was output into Microsoft Excel for further analysis.

4.2.8 Extinction per NP Calculations.

Estimates of extinction per NP were calculated previously using Mie solutions to Maxwell's equations, DDA, and CDA by Dunklin *et al.*² Briefly, extinction per NP for single particle Mie theory was determined via $\sigma(\log_{10}e)/n$ where σ was the Mie theory extinction cross section in cm^2 , $\log_{10}e$ was a conversion factor between log-bases, and n was the spectrum-averaged RI of PDMS (1.42). DDA and CDA output extinction efficiency were converted to an extinction cross-section before being converted to extinction per NP. The conversion from extinction efficiency to extinction cross-section was performed by multiplying the extinction efficiency by the NP geometric cross-section, i.e., πr^2 , where r was the radius of the sphere (50 or 75 nm). Extinction per NP for the current work was determined by A/cn where A is the extinction peak height and c is the density of NPs in a square lattice assuming one particle per cavity with an interparticle spacing of 600 nm.

4.3 Results and Discussion

4.3.1 Current Self-Assembly Approaches.

Possible options to fabricate ordered arrays of AuNPs using patterned substrates include self-assembly techniques like template-assisted self-assembly, dip-coating self-assembly, and directed self-assembly. Template-assisted self-assembly is a process that uses a patterned substrate (e.g., templated PDMS, templated silicon wafer, etc.) as a template to facilitate the NPs in solution to arrange in a regular, periodic structure either within the patterned substrate or on a separate substrate.¹⁹ In dip-coating self-assembly, a hydrophilic or hydrophilized patterned substrate is

dipped at controllable rates for various time intervals into a solution of NPs, where the NPs are drawn into the patterned cavities via convective and capillary forces.^{31,32} In directed self-assembly, a patterned substrate is attached to a linear translation stage and a fixed glass slide is used as a superstrate where a droplet of NPs is sandwiched between the fixed superstrate and the patterned substrate that moves at a controllable velocity.^{29,30}

Table 1 shows the various characterization and modeling techniques used to describe the arrays as well as compares four aspects of the aforementioned fabrication techniques with the method introduced in this work: (1) structure and dimensions of the nanostructure, (2) conditions and state for fabrication, (3) the substrate which the nanostructure is assembled, and (4) the fidelity of the fabricated arrays. Matricardi *et al.* introduced a template-assisted self-assembly method to fabricate ordered arrays of close-packed, mesoscopic clusters of AuNPs onto a hydrophilized glass coverslip by sandwiching a drop of AuNPs between a patterned PDMS substrate and a hydrophilized glass coverslip superstrate.¹⁹ V. Bejugam introduced an alternative template-assisted self-assembly method that sandwiched a 1-2 μL droplet of AuNPs between a PDMS-PEO copolymer substrate contained within a walled cage and a glass coverslip that sealed the cage and pinned the droplet to three sides of the substrate, after which the droplet was left to evaporate for >6 hours.⁴ Kinnear *et al.* introduced a dip-coating self-assembly method using a silanized patterned PDMS substrate and Juillerat *et al.* introduced a dip-coating self-assembly method using a hydrophilic patterned PMMA substrate, in which both substrates were dipped into solutions of NPs at various controlled rates.^{31,32} Cerf *et al.* used a directed self-assembly approach with a suspension of citrate-coated AuNPs containing 1 wt% Triton X-100 surfactant to increase the deposition in a hydrophobic patterned PDMS substrate, while Fan *et al.* used a much slower substrate velocity (0.6 $\mu\text{m/s}$), lower controlled temperature (21 $^{\circ}\text{C}$), and a controlled contact angle

(25 °) rather than surfactant or a hydrophilic patterned substrate to deposit silica-gold nanoshells into ordered arrays in PDMS.^{29,30} Based on the approaches described above, directed self-assembly offers the best approach to achieve high fidelity ordering of single AuNPs per cavity in a PDMS substrate across millimeter scale areas with high reproducibility and scalability.

This work introduces a refined directed self-assembly approach that uses a modified fixed glass superstrate and utilizes contact line pinning that conforms the droplet across a small square glass slide for deposition to occur. In conjunction with the modified fixed glass superstrate, the substrate was contained within a walled cage that reduced the evaporation rate of the droplet rather than controlling the temperature. Controlling the evaporation rate with the walled cage and modified superstrate offers a reproducible and scalable method for fabricating ordered arrays at ambient conditions. Varying the substrate velocity (deposition rate), AuNP diameter, and the evaporation rate resulted in densities of filled cavities between 85% and 100% with single AuNPs per cavity in higher density arrays.

Table 4.1 Characteristics and outcomes of current self-assembly processes compared with the self-assembly process introduced in this work.

Structure and Dimensions	Conditions/State	Substrate	Fidelity	Characterization/ Modeling Techniques
Template-Assisted Self-Assembly [4,19]				
Array dimensions: diameter: 230, 270, 330, 440, and 960 nm spacing: 400, 500, 600, 740, 1600 nm AuNP diameter: ~52 nm	AuNP dispersion between the hydrophilized coverslip and patterned PDMS at room temperature	Hydrophilized coverslip ----- Templated PDMS-PEO	Large area arrays with ~17 NPs per cavity, ~100% density of filled cavities, inconsistent size and number of NPs in each cavity	Characterization: UV-vis, FTIR, SEM, TEM, and SERS Modeling: FDTD
Array dimensions: diameter: 195 and 260 nm depth: 150 and 350 nm spacing: 600 and 700 nm AuNP diameter: 76 and 100 nm	Patterned PDMS-PEO contained within a walled cage and AuNP dispersion between the substrate in cage and glass coverslip superstrate		Large area arrays with 1-20 NPs per cavity, 50-90% density, inconsistent number of NPs in each cavity, wave-like deposition	Characterization: UV-vis and dark-field microscopy Modeling: COMSOL, Mie theory, and CDA
Dip-Coating Self-Assembly [31,32]				
Array dimensions: grooves: 40, 50, and 100 nm periods and 50-100 nm depths holes: 70, 85, 100, and 115 nm periods and 50-100 nm depths AuNP diameter: 15 and 50 nm Silica NP diameter: 50 nm	Hydraulic actuation, anti-vibratory system, ultrasonic treatment, sodium hydroxide, and nitric acid required Dip velocity: 0.3-10 mm/min pH: 2, 6, or 10	Si substrate coated with a layer of SiO ₂ /Cr and an additional layer of PMMA ----- Etched PMMA on a hydroxylated silicon wafer	Grooves resulted in 30-90% density with varying NP type and size as well as pH of the solution. Holes also resulted in 30-90% density with varying NP type and with/without ultrasonic treatment.	Characterization: high-resolution SEM (HRSEM) and photon correlation spectrometer (PCS) Modeling: Linear standard approximation (LSA)
Array dimensions: diameter: 160-180, 200, and 220 nm depth: 50 nm spacing: 6 μm NP diameter: 10-100 nm	Polyamine-based silane, piranha, methanol, mercaptoundecanoic acid, and 24 hr incubation period in NP suspension required at room temperature		105 x 105 arrays with 1-6 NPs per cavity resulting in 40-100% filled cavities depending on spacing and time pattern remained in solution	Characterization: Dark-field microscopy, SEM, % of filled cavities vs time, and AFM
Directed Self-Assembly [29,30]				
Array dimensions: diameter: 200, 250, 300, and 370 nm depth: 120 nm spacing: 1500, 2000, and 3000 nm NP diameter: 40, 100, and 250 nm	Linear translation stage, fixed glass superstrate, 25 μL drop of AuNPs, 27 °C set temperature, 1 μm/s substrate velocity, and 1 wt% Triton X-100	Templated PDMS ----- Templated PDMS	100 μm ² array with 1-5 NPs per cavity resulting in ~85% density of filled cavities 1-8 NPs per cavity resulting in ~100% density of filled cavities and ~30% yield of desired heptamers	Characterization: Dark-field microscopy and SEM Characterization: SEM and Scattering spectra Modeling: COMSOL
Array dimensions: diameter: 580 nm depth: 140 nm spacing: 1300-2000 nm NP diameter: ~176 nm	Linear translation stage, fixed glass superstrate, silica-gold nanoshells, 21 °C set temperature, and 0.6 μm/s substrate velocity			
Modified Directed Self-Assembly (this work)				
Array dimensions: diameter: 195 nm depth: 150 nm spacing: 600 nm NP diameter: 100 and 150 nm	Linear translation stage, modified fixed glass superstrate, 3 μL drop of AuNPs, 1 wt% Triton X-100 pre-coat of substrate at 8 μm/s velocity, and 1.2-2.1 μm/s substrate velocity for AuNP deposition	Templated PDMS	2 mm x 2 mm array with 1 NP per cavity resulting in ~100% density of filled cavities at optimal conditions and ~85% density at less optimal conditions	Characterization: Dark-field microscopy, UV-Vis spectroscopy, and extinction per NP calculations Modeling: Mie theory, DDA, CDA, rsa-CDA

4.3.2 Developing Uniform, Large Area AuNP Ordered Arrays.

The development of a scalable, economic, and reproducible approach to fabricating large area ordered arrays with high fidelity, density, and accuracy remains important for the advancement of electronic, sensing, and photonic devices. Directed self-assembly, in particular, offers a scalable, economic approach for fabricating ordered arrays with high fidelity and densities ranging from 70-85% for single particles per cavity and >85% for multiple particles per cavity.^{26,30,30-32} This work refines a directed self-assembly approach yielding densities of ~100% for large area (>2 mm x 2 mm) arrays by manipulating three primary variables: (1) evaporation rate, (2) deposition rate, and (3) NP diameter. The evaporation rate in this work was primarily due to the head-space within the walled cage when the superstrate was in contact with the droplet of AuNPs, the separation distance between the stamp and the superstrate, the separation distance between the cage and the superstrate, and the overall size of the superstrate that affected the airflow potential. It was observed that increasing the size of the superstrate resulted in a lower evaporation rate and higher deposition. Reducing the deposition rate resulted in higher overall densities for both high and low evaporation conditions. Increasing the AuNP diameter resulted in a more viscous solution with relatively similar concentrations of AuNPs, which also improved the densities while reducing evaporation potential due to the increased viscosity of the solution. The variables were used to fabricate the six arrays shown in Figure 1.

Figure 4.2 shows the results for six arrays fabricated using two different evaporation rates (high and low), two different AuNP diameters (100 and 150 nm), and four different deposition rates (2.1, 1.8, 1.5, and 1.2 $\mu\text{m/s}$). A deposition rate of 1.2 $\mu\text{m/s}$ (lower evaporation rate and 150 nm AuNP diameter held constant) was performed resulting in a >2 mm x 2 mm area of ~100% filled cavities

with high uniformity as shown in the bottom right (red filled triangle) images in Figure 4.2. The 20x inset shows a uniform color across the entire image while the 100x image shows the high density of filled cavities. Matricardi *et al.* and Zhang *et al.* report that the uniform color across the entirety of the array suggests that the nanoparticles are aligned and deposited in a uniform and reproducible manner within each cavity.^{19,25} The results for the bottom right image (red filled triangle) differ from many of the reported processes in that the array appears to consist of a uniform area of single AuNPs per cavity while reports by Cerf *et al.*, Zhang *et al.*, Matricardi *et al.*, Fan *et al.*, and Juillerat *et al.* show multiple particles per cavity.^{19,25,29–31} The AuNP diameter of 150 nm and the combination of water and Triton X-100 within a cavity with dimensions of 150 nm x 195 nm (depth x diameter) suggests that only a single AuNP could be within the cavity. Using a slightly faster deposition rate (1.5 $\mu\text{m/s}$) resulted in slightly lower uniformity and a lower density of filled cavities as shown in the middle right (blue filled triangle) 20x inset and 100x image, respectively. A calculable NP density was determined by counting the number of unfilled cavities and the total number of cavities in the 100x image, which showed that 98% of the cavities were filled.

Decreasing the AuNP diameter resulted in lower densities of filled cavities and a higher likelihood of multiple AuNPs per cavity based on lower uniformity in color across the array. The first array (black filled triangle) was fabricated using a high evaporation rate, a deposition rate of 2.1 $\mu\text{m/s}$, and 100 nm AuNP diameter, which resulted in the 20x image (inset) with observable non-uniform multicolored deposition and the 100x image that shows ~85% density of filled cavities. When maintaining the high evaporation rate (smaller superstrate) and 100 nm AuNP diameter while simultaneously decreasing the deposition rate to 1.8 and 1.5 $\mu\text{m/s}$, the uniformity and density increase resulting in the middle left (green filled triangle) and bottom left (gray filled triangle) images, respectively. The 20x images show the improved uniformity at the lower

deposition rate ($1.5 \mu\text{m/s}$) and the 100x images show the improved density of filled cavities ($\sim 90\%$). Decreasing the deposition rate to $1.2 \mu\text{m/s}$ while leaving the AuNP diameter and evaporation rate constant resulted in little deposition due to the droplet of AuNPs disconnecting from the glass slide on the superstrate as a result of the high evaporation rate. Using a low evaporation rate (larger superstrate) and maintaining the AuNP diameter (100 nm) and deposition rate ($1.5 \mu\text{m/s}$), results in the top right (orange filled triangle) images, which show a small improvement in the uniformity (20x inset) and density (100x image).

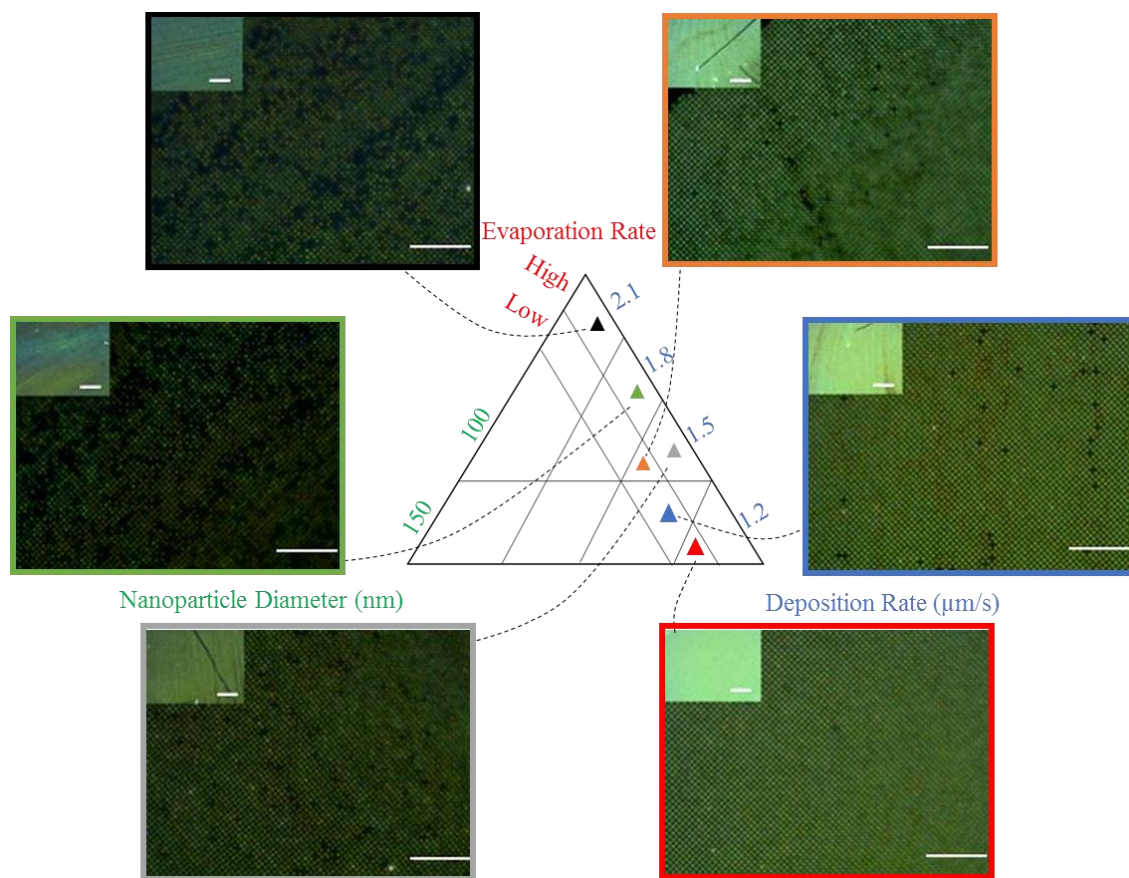


Figure 4.2 Controlled deposition via NP diameter, deposition rate, and evaporation rate resulted in uniform, large-area ($>2 \text{ mm} \times 2 \text{ mm}$) arrays of $\sim 100\%$ ordering. As the evaporation and deposition rates decreased and NP size increased, the uniformity, density, and ordering improved as shown in 100x images (scale bar: $30 \mu\text{m}$) and 20x insets (scale bar: $1000 \mu\text{m}$).

4.3.3 Optical Properties of AuNP Ordered Arrays.

The optical responses of ordered arrays of AuNPs generally determine the sensing efficiencies of ordered AuNPs, where the LSPR and SLR peak locations and peak heights account for a majority of the tunable optical responses for sensing applications.¹⁹ Extinction spectra were performed for the arrays shown in Figure 4.2 and normalized so that the valley just before the SLR feature was set to 0.01 absorbance units (A.U.) and displayed in Figure 4.3. The array images from Figure 4.3 were outlined in the corresponding line color for the extinction spectra and arranged to the right of the plot in Figure 4.3. LSPR and SLR peak location are designated in Figure 4.3 via a filled triangle matching the line color of the normalized extinction spectra. Extinction spectra for 150 nm AuNPs differ from extinction spectra of 100 nm AuNPs in that the 150 nm AuNPs have a third feature called a quadrupole at ~650 nm wavelength.³⁹ High density ordered arrays like those shown in Figure 4.2 resulted in observable blue-shifts in measured extinction spectra and extinction/NP calculations, which corresponds to estimates DeJarnette *et al.* previously reported.^{5,13} The LSPR and SLR peak locations blue-shift as the density increases (see Figure 4.3) for the green, gray, and orange lines. For the LSPR feature, the peak locations were ~555, 550, and 535 nm and the locations for the SLR peaks were ~778, 773, and 765 nm for the green, gray, and orange spectra, respectively. The spectra for the black line (LSPR = 547 nm and SLR = 756 nm) does not follow this trend, which was likely due to multiple layers of particles rather than single layers of particles like the other three spectra. The SLR and quadrupole peaks for the 150 nm AuNP spectra also blue-shifts as the density increases, but the LSPR peak has a slight red-shift (538 nm for blue line and 541 nm for red line).

Matricardi *et al.* showed that as the lattice spacing increases the peak height decreases.¹⁹ This work maintains a lattice spacing of 600 nm and increases the density of filled cavities for 100 nm AuNP arrays resulting in observable increases in peak heights (estimated by subtracting a baseline of 0.01 A.U. from the extinction at the LSPR or SLR peak). The density for the image boxed in gray was significantly higher than the density for the image boxed in green, which resulted in a significant increase in the SLR peak height of 0.011 A.U. (green) to 0.025 A.U. (gray). This 2.3-fold increase in peak height did not hold for the LSPR feature which had an increase from 0.020 A.U. (green) to 0.022 A.U. (gray) or a modest 1.1-fold increase. The difference in density between the gray and orange lines was minor but still resulted in 1.28- and 1.5-fold increases in peak height for the SLR and LSPR features, respectively.

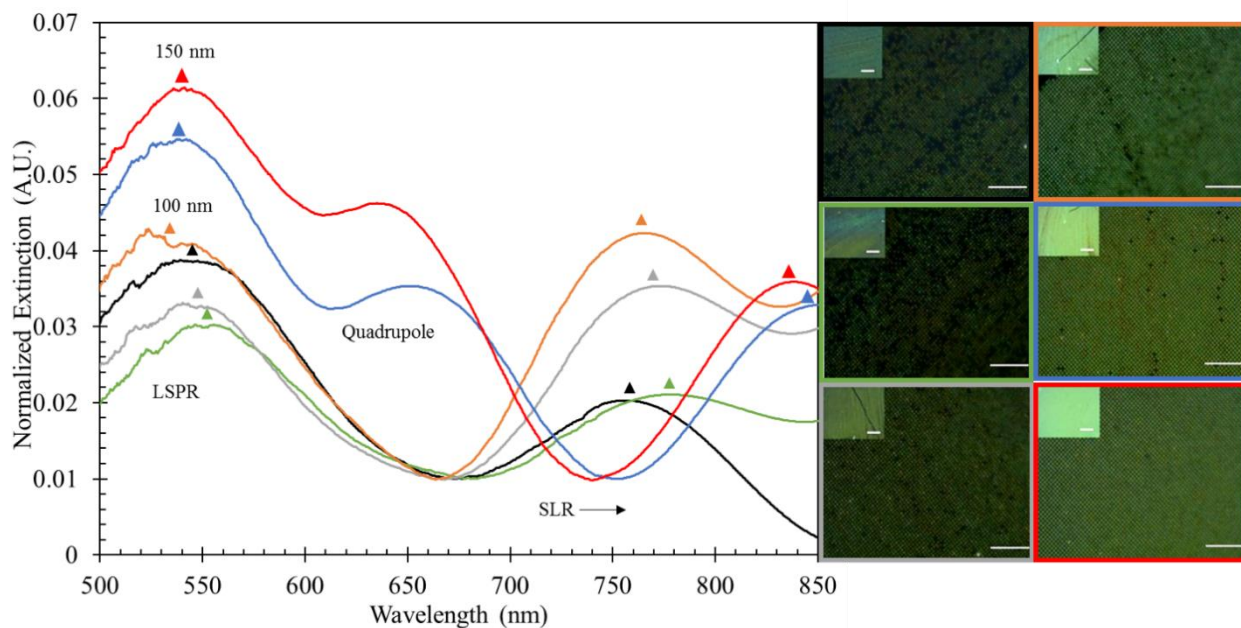


Figure 4.3 Extinction spectra for the six arrays shown in Figure 1 normalizing the valley before the SLR peak to 0.01 A.U. Colored triangles represent the peak locations for both LSPR and SLR features in spectra.

LSPR and SLR peak locations were estimated for Mie theory, DDA, CDA, and rsa-CDA and compared to measured peak locations in Figure 4.4. Peak locations for Mie theory and DDA

estimates (590-595 nm) were red-shifted compared to measured values (530-565 nm) due to differences in the RI values. Since an exact material composition surrounding the AuNPs in the PDMS cavity was lacking, Mie theory and DDA assumed the AuNPs were surrounded by a RI of PDMS (1.42), while the experimental system is surrounded by an unknown composition percentage of components of varying RI including air (1.00), Triton X-100 (1.49), water (1.33), and PDMS (1.42). Each material impacts the overall RI and either blue-shifts (decreasing RI) or red-shifts (increasing RI) the peak locations depending on which material surrounds the AuNPs at a higher fraction. CDA simulations estimated the LSPR peak location (565 nm) and the SLR peak location (642 nm) for 100 nm AuNPs where the LSPR peak showed a slight red-shift and the SLR showed a significant blue-shift compared to measured values ranging between 530-560 nm and 755-780 nm, respectively. SLR peak location estimates were closer for 150 nm AuNPs compared to 100 nm AuNPs, which is likely due to the 150 nm AuNP occupying a larger volume of the cavity compared to the 100 nm AuNP. The diameter of 195 nm and a depth of 150 nm cavity dimensions also reduces the possibility of multiple 150 nm AuNPs occupying the same cavity. Peak locations for rsa-CDA simulations were closer to measured values than those of CDA for 150 nm AuNPs. CDA simulations assign an array size of 301 x 301 like rsa-CDA but CDA uses a series of dipoles with a resolution of 5 nm to form each 100 and 150 nm AuNP while rsa-CDA assigns each AuNP as a single dipole point for faster computation of the results.

Measured and estimated extinction/NP values for 150 nm AuNPs were higher than those for 100 nm AuNPs for LSPR peaks while the SLR peaks were red-shifted >50 nm for the 150 nm AuNPs compared to 100 nm AuNPs. Extinction/NP estimates for 100 and 150 nm AuNP LSPR peaks using single particle simulations (Mie theory and DDA) and array simulations (CDA and rsa-CDA) were compared to measured extinction/NP values calculated from the spectral peaks in

Figure 4.3 (filled triangles), which is shown in Figure 4.4. Mie theory and DDA simulations estimated the extinction/NP ($9-10 \times 10^{-11}$) for the 100 nm AuNPs and were compared to measured values ranging from $5-8 \times 10^{-11}$. The CDA simulations assigned a RI of PDMS (1.42) surrounding the entire AuNP, while the measured values were within 195 nm diameter PDMS cavities and were surrounded by water (1.33), Triton X-100 (1.49), and air (1.00) at varying fractions per cavity.

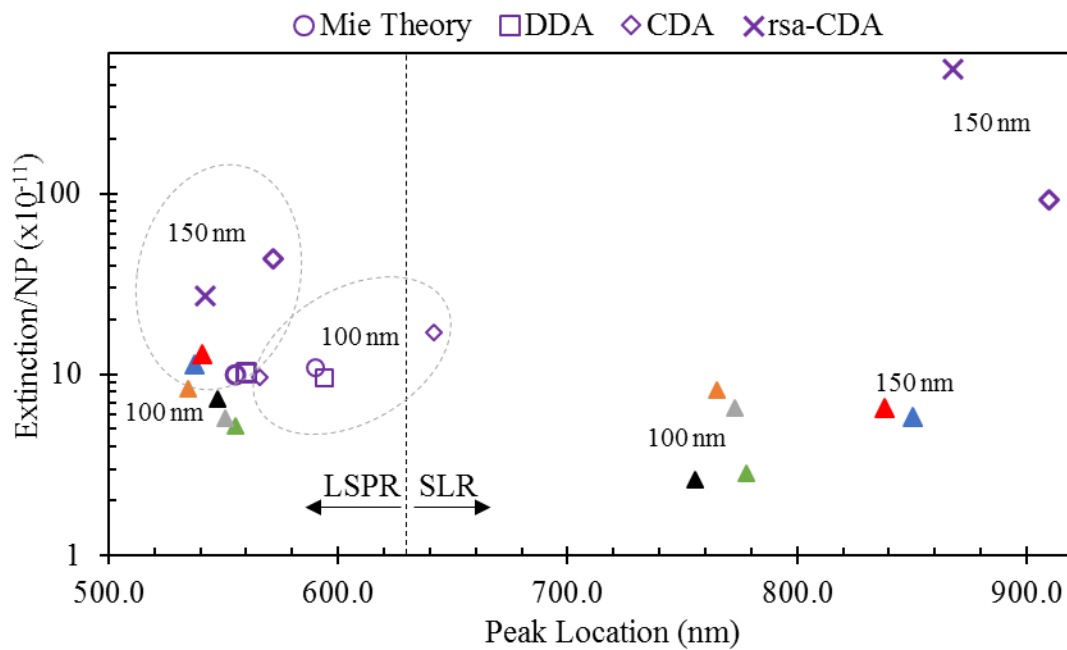


Figure 4.4 Extinction per NP calculations for measured (filled triangles with colors corresponding to spectra in Figure 2) and simulated (hollow symbols) data of 100 and 150 nm AuNP ordered arrays.

4.3.4 Experimental vs. Simulated Optical Properties.

As discussed in §*Optical Properties of AuNP Ordered Arrays*, the rsa-CDA simulations resulted in estimated peak locations comparable to measured peak locations for the 150 nm AuNP arrays and to previous estimated values reported by DeJarnette *et al.*^{5,13} An ordered array

containing 150 nm AuNPs was fabricated using the conditions shown in Figure 4.2 (red triangle, low evaporation rate and 1.2 $\mu\text{m/s}$ deposition rate). Optical spectra for this array was measured before the array was transferred to a glass slide via a process developed by Cerf *et al.*²⁹ The spectral peak locations for rsa-CDA simulations in PDMS (RI = 1.42) matched measured values for LSPR (542 vs. 542 nm), quadrupole (640 vs. 639 nm), and SLR (868 vs. 864 nm) values within 0.46% as shown in Figure 4.5. After performing UV-Vis spectroscopy on the array in PDMS, the array was transferred onto a glass substrate where UV-Vis spectroscopy was again performed to characterize the arrays on glass after the transfer. The spectral peak locations for the simulation versus measured for LSPR (558 vs. 551 nm), quadrupole (678 vs. 667 nm), and SLR (934 vs. 926 nm) on glass (RI = 1.52) matched within 1.7%. The ~ 3.7 -fold increase in the percent difference between the PDMS and glass measured versus simulation data is likely due to the decrease from $\sim 100\%$ density of filled cavities in PDMS to $\sim 85\%$ density on glass.

Not only were the peak locations comparable between experimental and simulation spectra, but the relative increase in peak heights were comparable. The LSPR peak height appeared to slightly increase in the experimental results for glass (~ 0.09 A.U.) compared to PDMS (~ 0.04 A.U.). This relative doubling of the measured peak heights was also observed in the simulation results as the LSPR peak height for the simulation of the array on glass appears to be slightly above the simulation spectra for PDMS. This was also observed for the quadrupole peak in which the experimental and simulation results for both glass and PDMS was the same. The experimental peak height for the array on glass (~ 0.1 A.U.) was nearly double the experimental peak height for the array in PDMS (~ 0.05 A.U.) while the simulation peak heights were also nearly double for the arrays on glass compared to the arrays in PDMS.

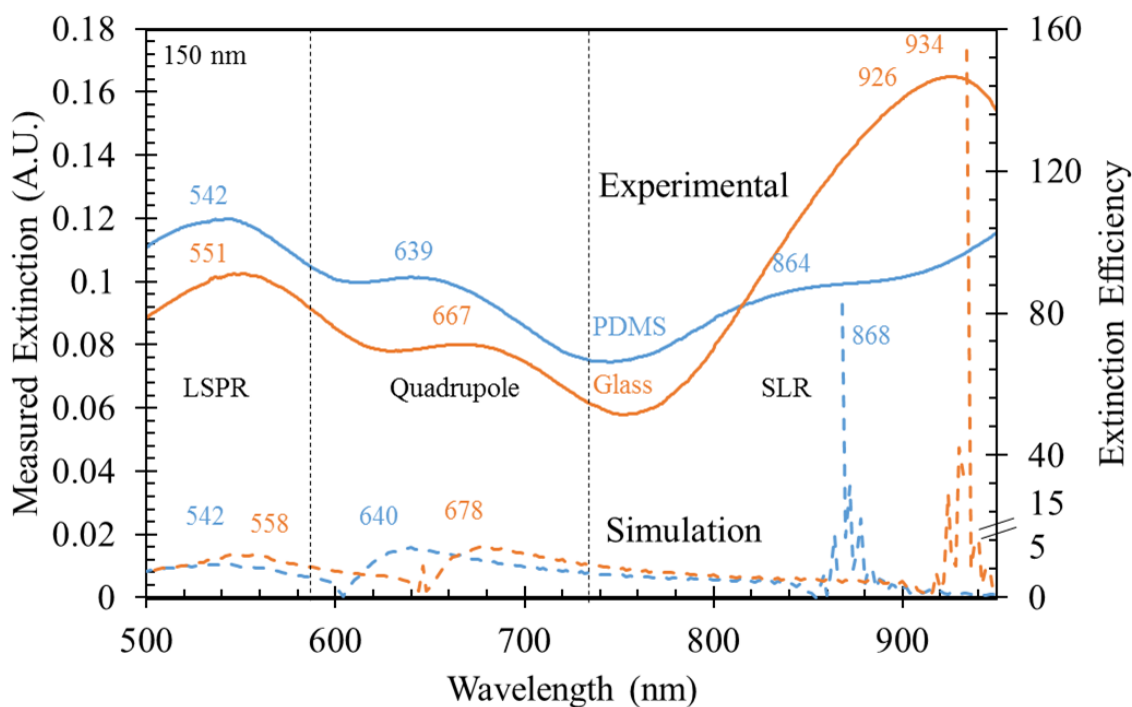


Figure 4.5 Measured extinction and rsa-CDA simulated extinction efficiency for an ordered array of 150 nm AuNPs in PDMS and transferred to glass.

4.4 Conclusions

In summary, directed self-assembly was used to fabricate square arrays of AuNPs resulting in large area arrays with observable optical enhancements as the density of filled cavities increased. Controlling the evaporation rate, deposition rate, and AuNP size resulted in $>2 \text{ mm} \times 2 \text{ mm}$ arrays with $\sim 100\%$ filled cavities containing one AuNP per cavity. Extinction spectra showed that as the density of filled cavities increased both the LSPR and SLR peak locations blue shifted and the peak heights increased. Extinction/NP calculations for measured 100 and 150 nm AuNPs in square arrays were also blue-shifted compared to simulated values for single particles (Mie theory and DDA) and finite arrays (CDA and rsa-CDA). The SLR peak height was shown to significantly increase when transferred from inside PDMS cavities onto a glass substrate. The experimental

peak locations for the arrays both in PDMS and on glass were matched within 0.5 and 1.7%, respectively, compared to rsa-CDA simulations.

4.5 Author Information

AUTHOR CONTRIBUTIONS

K. Berry refined the directed self-assembly process that yielded reproducible, large area, and high density ordered arrays and drafted text and figures. R. Romo performed the simulations and added text discussing the simulations. M. Mitchell assisted in drafting the table of self-assembly references, added text discussing the table, and fabricated blank stamps used for self-assembly experiments. V. Bejugam built the cage and fabricated blank stamps. D. K. Roper directed the work and refined text and figures.

Notes

The authors declare no competing financial interest.

4.6 Acknowledgements

This research work was supported by the Center for Advanced Surface Engineering (CASE), under the National Science Foundation (NSF) Grant No. OIA-1457888 and the Arkansas EPSCoR Program. Dr. Roper also acknowledges support from Utah State University. The authors would like to thank Megan Lanier for fabricating additional blank stamps and Loc Huynh for performing preliminary self-assembly experiments.

4.7 References

- (1) Amendola, V.; Pilot, R.; Frascioni, M.; Maragò, O. M.; Iatì, M. A. Surface Plasmon Resonance in Gold Nanoparticles: A Review. *J. Phys. Condens. Matter* **2017**, *29* (20). <https://doi.org/10.1088/1361-648X/aa60f3>.
- (2) Dunklin, J. R.; Bodinger, C.; Forcherio, G. T.; Roper, D. K. Plasmonic Extinction in Gold Nanoparticle-Polymer Films as Film Thickness and Nanoparticle Separation Decrease below Resonant Wavelength. *J. Nanophotonics* **2017**, *11* (1). <https://doi.org/10.1117/1.JNP.11.016002>.
- (3) Kravets, V. G.; Kabashin, A. V.; Barnes, W. L.; Grigorenko, A. N. Plasmonic Surface Lattice Resonances: A Review of Properties and Applications. *Chem. Rev.* **2018**, *118* (12), 5912–5951. <https://doi.org/10.1021/acs.chemrev.8b00243>.
- (4) Bejugam, V. Opto-Thermal Characterization of Plasmon and Coupled Lattice Resonances in 2-D Metamaterial Arrays. *Theses Diss.* **2018**, 2868.
- (5) DeJarnette, D.; Norman, J.; Roper, D. K. Attribution of Fano Resonant Features to Plasmonic Particle Size, Lattice Constant, and Dielectric Wavenumber in Square Nanoparticle Lattices. *Photonics Res.* **2014**. <https://doi.org/10.1364/PRJ.2.000015>.
- (6) Forcherio, G. T.; Blake, P.; Seeram, M.; DeJarnette, D.; Roper, D. K. Coupled Dipole Plasmonics of Nanoantennas in Discontinuous, Complex Dielectric Environments. *J. Quant. Spectrosc. Radiat. Transf.* **2015**. <https://doi.org/10.1016/j.jqsrt.2015.07.017>.
- (7) Francescato, Y.; Giannini, V.; Maier, S. A. Plasmonic Systems Unveiled by Fano Resonances. *ACS Nano* **2012**. <https://doi.org/10.1021/nn2050533>.
- (8) Guo, R.; Hakala, T. K.; Törmä, P. Geometry Dependence of Surface Lattice Resonances in Plasmonic Nanoparticle Arrays. *Phys. Rev. B* **2017**, *95* (15), 1–11. <https://doi.org/10.1103/PhysRevB.95.155423>.
- (9) Humphrey, A. D.; Barnes, W. L. Plasmonic Surface Lattice Resonances on Arrays of Different Lattice Symmetry. *Phys. Rev. B - Condens. Matter Mater. Phys.* **2014**, *90* (7), 1–8. <https://doi.org/10.1103/PhysRevB.90.075404>.
- (10) Väkeväinen, A. I.; Moerland, R. J.; Rekola, H. T.; Eskelinen, A. P.; Martikainen, J. P.; Kim, D. H.; Törmä, P. Plasmonic Surface Lattice Resonances at the Strong Coupling Regime. *Nano Lett.* **2014**, *14* (4), 1721–1727. <https://doi.org/10.1021/nl4035219>.
- (11) Auguie, B.; Bendaña, X. M.; Barnes, W. L.; García De Abajo, F. J. Diffractive Arrays of Gold Nanoparticles near an Interface: Critical Role of the Substrate. *Phys. Rev. B - Condens. Matter Mater. Phys.* **2010**, *82*, 155447. <https://doi.org/10.1103/PhysRevB.82.155447>.
- (12) Blake, P.; Kühne, S.; Forcherio, G. T.; Roper, D. K. Diffraction in Nanoparticle Lattices Increases Sensitivity of Localized Surface Plasmon Resonance to Refractive Index Changes. *J. Nanophotonics* **2014**, *8* (1), 083084. <https://doi.org/10.1117/1.JNP.8.083084>.

- (13) DeJarnette, D.; Jang, G. G.; Blake, P.; Roper, D. K. Polarization Angle Affects Energy of Plasmonic Features in Fano Resonant Regular Lattices. *J. Opt.* **2014**, *16* (10), 105006. <https://doi.org/10.1088/2040-8978/16/10/105006>.
- (14) Fano, U. Effects of Configuration Interaction on Intensities and Phase Shifts. *Phys. Rev.* **1961**, *124* (6), 1866–1878. <https://doi.org/10.1103/PhysRev.124.1866>.
- (15) Flídj, N.; Laurent, G.; Aubard, J.; Lvi, G.; Hohenau, A.; Krenn, J. R.; Aussenegg, F. R. Grating-Induced Plasmon Mode in Gold Nanoparticle Arrays. *J. Chem. Phys.* **2005**, *123* (22), 221103. <https://doi.org/10.1063/1.2140699>.
- (16) Forcherio, G. T.; Blake, P.; DeJarnette, D.; Roper, D. K. Nanoring Structure, Spacing, and Local Dielectric Sensitivity for Plasmonic Resonances in Fano Resonant Square Lattices. *Opt. Express* **2014**, *22* (15), 17791. <https://doi.org/10.1364/OE.22.017791>.
- (17) Baur, S.; Sanders, S.; Manjavacas, A. Hybridization of Lattice Resonances. *ACS Nano* **2018**, *12* (2), 1618–1629. <https://doi.org/10.1021/acsnano.7b08206>.
- (18) Khlopin, D.; Laux, F.; Wardley, W. P.; Martin, J.; Wurtz, G. A.; Plain, J.; Bonod, N.; Zayats, A. V.; Dickson, W.; Gérard, D. Lattice Modes and Plasmonic Linewidth Engineering in Gold and Aluminum Nanoparticle Arrays. *J. Opt. Soc. Am. B* **2017**, *34* (3), 691. <https://doi.org/10.1364/JOSAB.34.000691>.
- (19) Matricardi, C.; Hanske, C.; Garcia-Pomar, J. L.; Langer, J.; Mihi, A.; Liz-Marzán, L. M. Gold Nanoparticle Plasmonic Superlattices as Surface Enhanced Raman Spectroscopy Substrates. *ACS Nano* **2018**. <https://doi.org/10.1021/acsnano.8b04073>.
- (20) Blake, P.; Obermann, J.; Harbin, B.; Roper, D. K. Enhanced Nanoparticle Response from Coupled Dipole Excitation for Plasmon Sensors. *IEEE Sens. J.* **2011**, *11* (12), 3332–3340. <https://doi.org/10.1109/JSEN.2011.2158417>.
- (21) Komanicky, V.; Lddir, H.; Chang, K. C.; Menzel, A.; Karapetrov, G.; Hennessy, D.; Zapol, P.; You, H. Shape-Dependent Activity of Platinum Array Catalyst. *J. Am. Chem. Soc.* **2009**. <https://doi.org/10.1021/ja900459w>.
- (22) Mårtensson, T.; Carlberg, P.; Borgström, M.; Montelius, L.; Seifert, W.; Samuelson, L. Nanowire Arrays Defined by Nanoimprint Lithography. *Nano Lett.* **2004**. <https://doi.org/10.1021/nl035100s>.
- (23) Nagpal, P.; Lindquist, N. C.; Oh, S. H.; Norris, D. J. Ultrasoother Patterned Metals for Plasmonics and Metamaterials. *Science* (80-.). **2009**. <https://doi.org/10.1126/science.1174655>.
- (24) Tajdidzadeh, M.; Zakaria, A. B.; Talib, Z. A.; Gene, A. S.; Shirzadi, S. Optical Nonlinear Properties of Gold Nanoparticles Synthesized by Laser Ablation in Polymer Solution. *J. Nanomater.* **2017**, *2017*. <https://doi.org/10.1155/2017/4803843>.

- (25) Zhang, H.; Cadusch, J.; Kinnear, C.; James, T.; Roberts, A.; Mulvaney, P. Direct Assembly of Large Area Nanoparticle Arrays. *ACS Nano* **2018**, *12*, 7529–7537. <https://doi.org/10.1021/acsnano.8b02932>.
- (26) Mohd Arif, N. A. A.; Jiun, C. C.; Shaari, S. Effect of Annealing Temperature and Spin Coating Speed on Mn-Doped ZnS Nanocrystals Thin Film by Spin Coating. *J. Nanomater.* **2017**, *2017*, 1–6. <https://doi.org/10.1155/2017/2560436>.
- (27) Wujcik, E. K.; Aceto, S. R.; Narayanan, R.; Bose, A. Lead Selenide Nanostructures Self-Assembled across Multiple Length Scales and Dimensions. *J. Nanomater.* **2016**, *2016*, 1–6. <https://doi.org/10.1155/2016/9575839>.
- (28) Ahn, W.; Roper, D. K. Periodic Nanotemplating by Selective Deposition of Electroless Gold Island Films on Particle-Lithographed Dimethyldichlorosilane Layers. *ACS Nano* **2010**. <https://doi.org/10.1021/nn100338f>.
- (29) Cerf, A.; Vieu, C. Transfer Printing of Sub-100 Nm Nanoparticles by Soft Lithography with Solvent Mediation. *Colloids Surfaces A Physicochem. Eng. Asp.* **2009**, *342* (1–3), 136–140. <https://doi.org/10.1016/j.colsurfa.2009.04.019>.
- (30) Fan, J. A.; Bao, K.; Sun, L.; Bao, J.; Manoharan, V. N.; Nordlander, P.; Capasso, F. Plasmonic Mode Engineering with Templated Self-Assembled Nanoclusters. *Nano Lett.* **2012**, *12* (10), 5318–5324. <https://doi.org/10.1021/nl302650t>.
- (31) Juillerat, F.; Solak, H. H.; Bowen, P.; Hofmann, H. Fabrication of Large-Area Ordered Arrays of Nanoparticles on Patterned Substrates. *Nanotechnology* **2005**, *16* (8), 1311–1316. <https://doi.org/10.1088/0957-4484/16/8/055>.
- (32) Kinnear, C.; Cadusch, J.; Zhang, H.; Lu, J.; James, T. D.; Roberts, A.; Mulvaney, P. Directed Chemical Assembly of Single and Clustered Nanoparticles with Silanized Templates. *Langmuir* **2018**, *34* (25), 7355–7363. <https://doi.org/10.1021/acs.langmuir.8b00775>.
- (33) Lee, D. E.; Ryu, J.; Hong, D.; Park, S.; Lee, D. H.; Russell, T. P. Directed Self-Assembly of Asymmetric Block Copolymers in Thin Films Driven by Uniaxially Aligned Topographic Patterns. *ACS Nano* **2018**, *12* (2), 1642–1649. <https://doi.org/10.1021/acsnano.7b08226>.
- (34) Malaquin, L.; Kraus, T.; Schmid, H.; Delamarche, E.; Wolf, H. Controlled Particle Placement through Convective and Capillary Assembly. *Langmuir* **2007**, *23* (23), 11513–11521. <https://doi.org/10.1021/la700852c>.
- (35) Yin, Y.; Gates, B.; Xia, Y. Template Assisted Assembly: A Practical Route to Complex Aggregates of Monodispersed Colloids with Well-Defined Sizes, Spheres and Structures. *J. Am. Chem. Soc.* **2001**, *123* (36), 8718–8729. <https://doi.org/10.1021/ja011048v>.

- (36) Dejarnette, D.; Blake, P.; Forcherio, G. T.; Keith Roper, D. Far-Field Fano Resonance in Nanoring Lattices Modeled from Extracted, Point Dipole Polarizability. *J. Appl. Phys.* **2014**, *115* (2). <https://doi.org/10.1063/1.4858396>.
- (37) Dejarnette, D.; Roper, D. K. Electron Energy Loss Spectroscopy of Gold Nanoparticles on Graphene. *J. Appl. Phys.* **2014**, *116* (5). <https://doi.org/10.1063/1.4892620>.
- (38) Seeram, M.; Forcherio, G. T.; Roper, D. K. Shape Generator for the DDSCAT Software. 2016. <https://doi.org/10.4231/D3J960B3D>.
- (39) Burrows, C. P.; Barnes, W. L. Large Spectral Extinction Due to Overlap of Dipolar and Quadrupolar Plasmonic Modes of Metallic Nanoparticles in Arrays. *Opt. Express* **2010**, *18* (3), 3187–3198. <https://doi.org/10.1364/OE.18.003187>.

5. TRANSFER PRINTING ORDERED GOLD NANOPARTICLES ONTO A LEAF SURFACE VIA LASER INDUCTION AND RESINOUS ADHESION

Keith R. Berry Jr.¹, Michelle A. Dopp¹, and D. Keith Roper^{2,*}

¹ Ralph E. Martin Department of Chemical Engineering, University of Arkansas, Fayetteville, AR 72701, USA

² Department of Biological Engineering, Utah State University, Logan, UT 84322, USA

* Corresponding Author

ABSTRACT

Nanoparticle (NP) printing can fabricate sensors that conform to various surfaces to enhance and improve sensing applications. Flexible sensors show promise for real-time monitoring and analysis to improve plant growth and crop productivity. Sensors comprised of ordered nanoparticle arrays that couple near- and far-field effects could enhance sensitivity, specificity, and stability relative to other modalities. This would require economic nanoparticle ordering and high-fidelity, biocompatible transfer of arrayed nanoparticles to leaf surfaces. Here we examine two feasible methods to reproducibly transfer nanoparticles evaporatively self-assembled into a square lattice with submicron pitch onto a leaf surface: (1) laser induction and (2) resinous adhesion. Laser induction without cyanoacrylate transferred ordered particles conformal to the leaf surface across areas up to 15 μm x 15 μm ; using cyanoacrylate increased transferable area up to 50 μm x 50 μm but resulted in leaf degradation. Resinous adhesion transferred ordered nanoparticles onto the leaf reproducibly and at high fidelity across areas up to 2 mm x 2 mm without visual discoloration.

Nanoparticle transfer to leaves in each method was facilitated by biochemical functionality of surfactants and adhesives.

Keywords: *Nanoparticle ordered array, nanoparticle printing, array transfer to leaf*

5.1. Introduction.

Demand for higher crop yield amidst variable and extreme weather events increases the need to monitor plant photosynthesis, nutrient intake, resilience to stress, and response to interventions. Non-invasive monitoring by existing sensors across micron to millimeter scales based on transducing electric field effect, surface plasmon resonance, enzyme interaction and/or spectral activity is constrained by intrinsic limits to sensitivity, specificity, throughput, stability, biocompatibility, and portability of these approaches.¹ Two-dimensional (2D) ordered arrays of nanoparticle (NP) could overcome these limits by interacting selective, energetic near-field responses with high-bandwidth adaptive far-field signals to significantly enhance non-invasive monitoring, e.g., of plants.² Coupling of plasmon-enhanced local electromagnetic (EM) field to light diffracted from a grating formed by 2D ordered NPs yields a unique surface lattice resonance, i.e., Fano resonance or coupled lattice resonance, beyond the localized surface plasmon resonance. Spectral features of this resonance are tunable by varying the incident EM field, grating constant, NP geometry, and adjacent refractive index (RI).³⁻⁸ Recent advances in the development of ordered NP structures have been motivated by potential use in flexible electronics.⁹⁻¹⁸ Flexible electronics were introduced in wearable sensors for real-time health monitoring of, e.g., biometrics, muscular stress and strain, and exposure to ultraviolet (UV) radiation.^{10,12,13} More recently, flexible

electronics including arrayed nanomaterials like graphene oxide have been applied toward real-time, *in situ* monitoring of nutrient uptake, utilization and efficiency of a plant or row crop.^{12,19}

Development of wearable electronics for biological, chemical, and physiological sensing has relied on advances in printing ordered nanoparticle structures⁹⁻¹¹ and transferring such structures to surfaces of interest. Top-down electron beam lithography (EBL), nanotribological printing (NTP), aerodynamically focused nanoparticle (AFN) printing, and dip-pen nanolithography (DPN) have been widely used to create high-fidelity, scalable ordered nanostructures with node dimensions less than 20 nm. Extreme conditions required for such methods, e.g., high temperature, high vacuum, and strong solvents, however, are incompatible for direct contact with susceptible plant matter.²⁰⁻²⁴ Therefore ordered structures have been fabricated and/or transferred onto human skin and plant surfaces^{12-14,16,17,25-30} using microcontact printing, direct laser writing, tape nanolithography, and adhesive patches or sprays. Maintaining sub-micron ordering during fabrication and transfer, however, has proved challenging. Moreover, requirements for capital, materials, and procedures limit economic adaptation of reported techniques for printing ordered nanoparticles to monitor plants in plots or fields to support data-driven precision agriculture.

This work compares transfer of NPs evaporatively self-assembled into ordered cavities of a polydimethylsiloxane (PDMS) stamp onto the waxy abaxial (lower) surface of a leaf via two methods, laser induction and resinous adhesion. Laser induction of ordered NP transfer employed continuous low power (50 mW) irradiation with or without cyanoacrylate to reposition AuNPs onto the non-stem-facing surface of an *Apocynum cannabinum* leaf. The resinous adhesion method stamped a thin film of shellac onto the NP-bearing PDMS surface by which ordered NP were then contact-printed onto the abaxial *Apocynum cannabinum* leaf surface. Resulting degree of preserved order, area of high-fidelity transfer, and effect on leaf viability were analyzed visually

and microscopically. Chemical and biochemical functionality of surfactant and adhesive polymers used to facilitate transfer were evaluated. Both laser and resinous methods could cost-effectively transfer ordered arrays onto a leaf surface across $> 100 \mu\text{m}^2$ areas at sub-micron fidelity. Compared to laser induction, resinous adhesion offers reproducible transfer to a leaf in a field setting without using optoelectronic instruments.

5.2. Materials and Methods.

5.2.1 Fabrication of AuNP Array

A previously reported process for evaporative self-assembly of AuNP in cylindrical cavities was modified in order to increase AuNP ordering and nodal density to $>95\%$ in lattice arrays spanning areas $>100 \mu\text{m}^2$.²⁸ Briefly, a silicon master with an area of $8 \times 8.3 \text{ mm}^2$ fabricated with $150 \text{ nm} \times 195 \text{ nm}$ (height \times diameter) cylindrical pillars in a square lattice at a pitch of 600 nm was purchased from Lightsmyth Technologies (Eugene, OR., S2D-24B2-0808-150-P). PDMS was cured onto the silicon master stamp yielding an $8 \text{ mm} \times 8.3 \text{ mm}$ PDMS stamp with a square array of cavities corresponding to the pillar array dimensions. Spherical AuNPs of 100 nm diameter purchased from Nanopartz (Loveland, CO., AC11-100-CIT-DIH-100-1) were diluted to 3 mg/mL in aqueous 1% Triton X-100 (Sigma Aldrich, St. Louis, MO., X100-5ML). The $8 \text{ mm} \times 8.3 \text{ mm}$ stamp was cut in half and one half was placed on the linear stage. A $2.5 \mu\text{L}$ drop of 1% Triton X-100 was added to the edge of the stamp. A superstrate was lowered onto the drop to spread it across the bottom third of the stamp. The stage was then moved horizontal to the stamp surface at a linear velocity of $8 \mu\text{m/s}$ to deposit surfactant on the stamp surface and in cavities as liquid from the drop evaporated. After this 1% Triton X-100 stamp pre-coat, a $2.5 \mu\text{L}$ drop of the AuNPs was added

and spread by lowering the superstrate then evaporated by moving the linear stage at 1.2 $\mu\text{m/s}$. This deposited a single AuNP into each cavity arrayed on the stamp surface, resulting in ordered AuNP lattices across areas up to $\sim 2\text{ mm} \times 2\text{ mm}$. More than 95% of the cavities in the area contained a single AuNP (i.e., >95% nodal density or >95% transfer). The number of AuNP ordered in a cavity rather than deposited randomly on the stamp surface was >95% (i.e., >95% ordering). These AuNPs arrayed into PDMS cavity lattices were subsequently transferred using the laser induction and resinous adhesion methods.

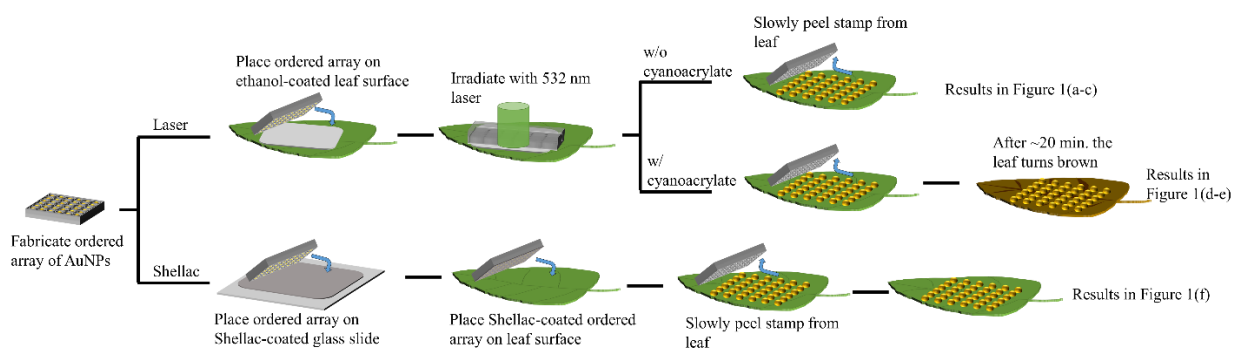


Figure 5.1 Two processes to transfer arrayed nanoparticles onto a leaf surface: (i) laser induction and (ii) resinous adhesion. Laser induction was conducted with and without cyanoacrylate.

5.2.2 Nanoparticle Printing via Laser Induction with and without Cyanoacrylate

A PDMS stamp containing ordered AuNPs was coated with 20% Triton X-100 using a motorized linear stage at 8 $\mu\text{m/s}$. After 20% Triton X-100 post-coat, a 3 μL drop of ethanol (95%, V1101, Decon Labs, Inc., King of Prussia, PA) was placed on the *Apocynum cannabinum* leaf surface. The stamp was inverted onto the ethanol and the system was irradiated continuously with a 532 nm laser at 50 mW for 10 minutes (min). The stamp was then carefully removed from the leaf leaving the AuNPs ordered on its surface. In the absence of the 20% Triton X-100 post-coat, transfer of AuNPs was reduced to <10%. Use of other solvents, i.e., deionized distilled (DI) water,

50:50 DI water:ethanol, 80:20 DI water:ethanol, and 90:10 DI water:ethanol, resulted in no visible transfer of AuNPs from cavities onto the leaf surface.

Variations to this transfer method were tested and adopted to increase its fidelity. Minimal contact between the stamp and the leaf surface was observed initially, resulting in lower transfer fidelity and small areas of ordering as shown in Figure 5.3(a-b). In order to promote improved contact between the leaf and the stamp for all subsequent laser induction transfers with and without cyanoacrylate, light weights (<10 grams) were added on top of the inverted stamp before the laser irradiation began which increased the area and fidelity of ordered transfer as shown in Figure 5.3(c-e). Besides continuous irradiation for 10 min, laser irradiation for 10 s alternated with a 3 s break over 10 min and continuous irradiation through an optical chopper purchased from Thorlabs (Newton, NJ, MC2000B) operating at 6000 Hz were tested. The latter visibly improved the area and fidelity of ordered transfer. The chopper was used in all subsequent laser induction transfer.

Cyanoacrylate deposited on one AuNP array fabricated via directed self-assembly was observed to improve subsequent AuNP transfer to $\geq 95\%$. Consequently, to a PDMS stamp containing AuNPs arrayed in cavities, a post-coat of 20% Triton X-100 containing a drop (~5 mg) of cyanoacrylate was applied to the stamp surface using the motorized linear stage at 8 $\mu\text{m/s}$. A larger mass of cyanoacrylate resulted in a thick layer of glue across the surface of the stamp, preventing effective transfer of AuNPs. After the Triton/cyanoacrylate post-coat, a 2.5 μL drop of ethanol was placed on the *Apocynum cannabinum* leaf surface, the stamp was inverted onto the ethanol, and light weights (<10 grams) were added on top of the inverted stamp. The system was irradiated with a 532 nm laser at 50 mW for 10 min through the chopper at 6000 Hz. Figure 5.1 shows a schematic of the process used for the laser induction transfer method with and without the cyanoacrylate. Corresponding results are shown in Figure 5.3(a-e).

5.2.3 Nanoparticle Printing via Resinous Adhesion

Shellac is a resin secreted by a female lac bug on trees in the forests of India and Thailand. It consists of various biochemical components with polar and non-polar character.³¹ The resinous structure of shellac is due to the association of these components through van der Waals and hydrogen bonding interactions. Secreted resin exhibits a variety of colors but is bleached multiple times in order to render it transparent before it is dissolved in alcohol to liquefy and aerosolize it.³¹ Shellac, C₃₀H₅₀O₁₁, (Zinsser Bulls Eye Shellac Traditional Finish and Sealer aerosol spray) was applied to a clean glass microscope slide by spraying two 1 s passes across the slide at a distance of 250 mm. A 4 mm x 8.3 mm PDMS stamp containing a square array of 100 nm AuNPs deposited 600 nm apart in cavities was immediately inverted onto the shellac-coated glass slide and cured for 1.5 min at ambient conditions. Cure times great than 1.5 min yielded NPs remaining on the glass slide. After the 1.5 min cure, the stamp was removed from the shellac-coated glass slide, placed face-up on a second glass slide, and cured for an additional 1.5 min at ambient conditions. Then the stamp was then inverted on the adaxial (upper or stem-facing) or abaxial (lower) side of an *Apocynum cannabinum* leaf and gently pressed with a finger for 1 min. After the 1 min period, the stamp was slowly peeled from the surface of the leaf, starting at one corner of the stamp, leaving behind a thin layer of shellac to which the ordered array of AuNPs adhered. Figure 5.1 shows a schematic of the process used for this transfer method and the results are shown in Figure 5.3(f).

5.3. Results and Discussion

5.3.1 Comparison of Nanoparticle Printing with Arrayed NP Transfer

Possible options to transfer nanomaterials to biological surfaces include printing techniques like tape nanolithography, direct laser writing, microcontact printing, and stamp-assisted printing. Tape nanolithography is a process that utilizes soft lithography to develop a nanopatterned donor substrate that is deposited with a desired nanomaterial before direct taping and peeling of the nanomaterial is performed.¹⁷ In direct laser writing, a focused femtosecond laser causes localized polymerization of the target polymer allowing three-dimensional (3-D) structures to be directly written on the polymer substrate.^{26,32-34} In microcontact printing, a solvent (i.e. water, ethanol, etc.) and high temperature (>100 °C) facilitates the transfer of ordered NPs contained within a pre-patterned PDMS substrate onto the surface of a second substrate (i.e., 3-Aminopropyl)triethoxysilane- (APTES)-coated glass slide, borosilicate glass slide, etc.).²⁸ Stamp-assisted printing is a process where insulating ink is imprinted onto a conductive glass slide using a patterned stamp, electroplated with a metal before the ink is removed, and transferred onto an adhesive Kapton film.²⁹

Table 5.1 compares four aspects of these printing techniques with the arrayed transfer methods introduced in this work: (1) structure and dimensions of the nanostructure, (2) conditions and state of the transfer, (3) the substrate to which the nanostructure is transferred, and (4) the fidelity of the transfer process for each of the printing techniques. Oren *et al.*, Shi *et al.*, Wang, L. *et al.*, and Wang, Q. *et al.* each presented a different approach to tape nanolithography with varying degrees of success and potential applications.^{12,13,16,17} Bagheri *et al.* introduced a method using direct laser writing to print various sizes of nanoantenna onto a substrate requiring low laser power and

operation at room temperature; its requirement for vacuum operation, however, constrains application to live plants.²⁶ Cerf *et al.* used microcontact printing to transfer ordered AuNPs onto APTES-coated glass using solvent (water or ethanol) as a facilitating media for the transfer; its high heat requirement (100 °C) precludes this process from use on live plants.²⁸ Chen *et al.* introduced a stamp-assisted printing technique for the fabrication of flexible micro-supercapacitors (MSCs) onto an adhesive Kapton film that can be readily transferred to a multitude of surfaces.²⁹ Such an adhesive approach could in principle, but has not been shown to, support biocompatible transfer of ordered structures onto a leaf surface.

This work introduces two new potentially biocompatible approaches for conformal, high-fidelity transfer of ordered arrays onto sensitive biological surfaces (i.e., leaf, mammalian skin, etc.): (1) low-power laser induction and (2) resinous adhesion. The first approach, laser induction transfer, was developed with and without cyanoacrylate. Including cyanoacrylate ‘glued’ the ordered structure in place and maintained NP order on the leaf across areas up to 50 μm x 50 μm . But the leaf turned brown where it contacted the cyanoacrylate within 20 min of the transfer. Laser induction without cyanoacrylate resulted in areas of ordered transfer up to about 15 μm x 15 μm ; NPs outside these areas transferred conformally with varying degrees of disorder. This appeared due to varying topography of the leaf surface, which resulted in a range in degree and area of contact between the stamp containing the ordered array and the leaf surface.

By comparison, the second approach, resinous adhesion, preserved the NP ordering across areas up to 2 mm x 2 mm and did not observably alter the appearance of the leaf surface as with cyanoacrylate. Resinous adhesion was performed using shellac aerosol spray that preserved the AuNP ordering and adhered the arrayed AuNP to the leaf surface. Contacting the stamp containing ordered AuNPs to the shellac-coated glass slide for more than 1.5 min resulted in partial cure of

the shellac film which transferred AuNPs to the shellac-coated glass surface. Using more than two 1-s passes of Shellac spray gave a thicker shellac film on the PDMS stamp and reduced the success of the transfer of the arrayed AuNPs onto the leaf surface. Optimal resinous adhesion used two 1-s passes and a 1.5-min cure between the NP-containing PDMS film and the shellac-coated glass slide to reproducibly transfer arrayed NP to the leaf surface. Resinous adhesion was performed at room temperature without auxiliary instruments. It resulted in nearly complete transfer of the AuNPs ordered into PDMS cavity arrays onto the leaf surface as well as preservation of the 2D lattice pitch.

Table 5.1 Characteristics and outcomes of nanoparticle printing compared with the nanoparticle array transfer methods introduced in this work.

Structure and Dimensions	Conditions/State	Transfer Substrate	Fidelity
Tape Nanolithography ^{12,13,16,17}			
<ul style="list-style-type: none"> • 6 mm x 800 μm x 0.3 μm graphene patterns on tape roll • 600 μm thick patch with 25 μm thick skin adhesive • 200 nm holes with Ag/AuNW on 20 μm thick adhesive • 40 nm thick Au layer on 340 nm deep nanohole arrays 	<ul style="list-style-type: none"> • Adhesive required • Vacuum filtration • UV/O₂ exposure • Ethanol solvent • 70 °C transfer 	<ul style="list-style-type: none"> • Human skin • Glove • Leaf • TiO₂/ SiO₂ glass 	<ul style="list-style-type: none"> • 90-100 % overall pattern transfer • Minor defects in ordered structure after transfer • Adhesive remains on substrate
Direct Laser Writing ²⁶			
<ul style="list-style-type: none"> • Width: 105-335 nm • Length: 1.7-2.8 μm • Height: 75 or 105 nm • 7.6 mm x 7.6 mm array 	<ul style="list-style-type: none"> • Vacuum • Room Temperature • 5 to 9 mW laser power 	<ul style="list-style-type: none"> • CaF₂ 	<ul style="list-style-type: none"> • Minor variations in antenna sizes
Microcontact Printing ²⁸			
<ul style="list-style-type: none"> • 40, 100, and 250 nm AuNPs • 100 μm^2 array 	<ul style="list-style-type: none"> • Ethanol or water solvent • 100 °C evaporation in oven 	<ul style="list-style-type: none"> • APTES-coated glass 	<ul style="list-style-type: none"> • 85-95 % transfer
Stamp-assisted Printing ²⁹			
<ul style="list-style-type: none"> • Width: 1.4 mm • 300 μm gap between strips of electroplated Ni 	<ul style="list-style-type: none"> • Adhesive required 	<ul style="list-style-type: none"> • Kapton polyimide film 	<ul style="list-style-type: none"> • Minor defects upon transfer from FTO glass onto Kapton
Laser Induction with and without Cyanoacrylate (this work)			
<ul style="list-style-type: none"> • 2 mm x 2 mm square arrays of cavities in PDMS. Cavities spaced at a pitch of 600 nm • PDMS cavity dimensions: depth of 150 nm, diameter of 195 nm • 100 nm AuNPs 	<ul style="list-style-type: none"> • Ethanol solvent • 50 mW laser power • with and without cyanoacrylate 	<ul style="list-style-type: none"> • <i>Apocynum cannabinum</i> leaf 	<ul style="list-style-type: none"> • with cyanoacrylate: ~100% transfer and ~100% ordering across moderate areas but discolored leaf • without cyanoacrylate: \geq85% conformal transfer with 10-15% ordering across small areas
Resinous Adhesion (this work)			
<ul style="list-style-type: none"> • 2 mm x 2 mm square arrays of cavities in PDMS. Cavities spaced at a pitch of 600 nm • PDMS cavity dimensions: depth of 150 nm, diameter of 195 nm • 100 nm AuNPs 	<ul style="list-style-type: none"> • Room temperature • Shellac aerosol spray 	<ul style="list-style-type: none"> • <i>Apocynum cannabinum</i> leaf 	<ul style="list-style-type: none"> • ~100% transfer and ~100% ordering across large areas

5.3.2 *Apocynum cannabinum* Leaf Properties

Apocynum cannabinum leaves are simple, undivided leaves that are not separated into leaflets and are positioned opposite from each other having two leaves per node (point of attachment on branch).³⁵ The leaves are toothless and lobeless, oval in shape with a slightly pointed tip, and are generally 2 to 5 inches in length and $\frac{3}{4}$ to $1\frac{3}{4}$ inches wide. They have smooth surfaces with a prominent network of white veins. The thickness of the cuticle (outermost protective layer of leaf surface) on the adaxial (facing toward the stem or upper) and abaxial (facing away from the stem or lower) leaf surface were previously reported as 305 and 458 $\mu\text{g}/\text{cm}^2$. The average thickness of the epicuticular wax (wax found within matrix that imparts most of physicochemical characteristics of cuticle) layer was reported as 85 and 56 $\mu\text{g}/\text{cm}^2$ for the adaxial and abaxial surfaces, respectively. Stomata appeared only on the abaxial surface. There were about 320 stomata/ mm^2 .³⁵

The mass of wax per leaf surface area (commonly shown as $\mu\text{g}/\text{cm}^2$) has been widely characterized to relate it to herbicide absorption. The average thickness of the epicuticular wax layer was previously determined by washing the *Apocynum cannabinum* leaves with chloroform with the wash being filtered through filter paper, dried, and weighed. The upper and lower cuticles were separated via 48 hr immersion in 1g $\text{ZnCl}_2/1.7$ mL concentrated HCl, water immersion in a desiccator, and application of a vacuum. The formation of bubbles between the two cuticles promoted the separation of the cuticles without damage. The mesophyll was removed through water washing before the cuticles were dried and weighed.^{36,37}

5.3.3 Chemical and Biochemical Contributors to NP Transfer

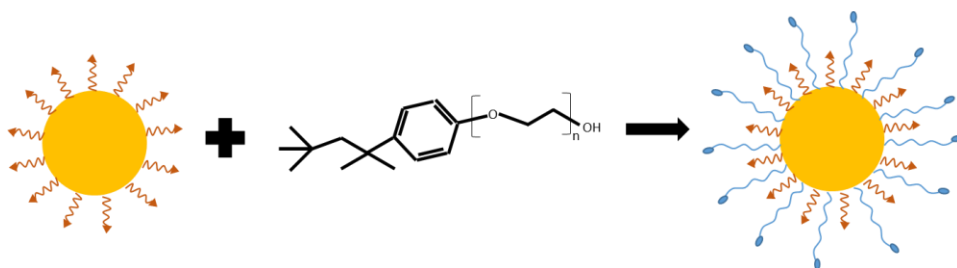
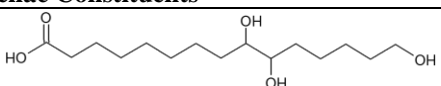
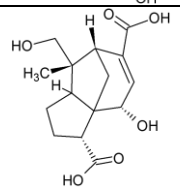


Figure 5.2 Citrate-coated AuNPs dispersed in Triton X-100 exhibited FTIR spectra indicating the hydrophobic alkyl arm of the Triton X-100 approaches the Au surface while the hydrophilic poly(ethylene) glycol arm interspersed in the citrate coat.

Dispersing citrate-coated AuNPs into a mixture of Triton X-100 and DI water resulted in further stabilization and capping of the AuNPs in solution. Gao *et al.* performed FTIR spectroscopy on citrate-coated AuNPs before and after the addition of Triton X-100.³⁸ One noted difference was that the FTIR response for the alkyl chain in Triton X-100 disappeared when in solution with AuNPs. Another difference was a shift in the bending corresponding to the $-\text{CH}_2$ of Triton X-100 when added to the AuNP solution. These differences were attributed to the packaging of the alkyl chain by the citrates wherein the hydrophilic polyethylene oxide chain interspersed in the citrates and the hydrophobic alkyl chain approached the AuNP surface.³⁸ Figure 5.2 shows a representative schematic of the capping of citrate-coated AuNPs with Triton X-100 based on these findings.

Table 5.2 Primary constituents of cutin and epicuticular wax on a leaf surface, superglue, citrate capping agent, surfactant, and shellac that facilitate adhesion of AuNPs to a leaf surface.

Constituent Type	Constituent Formula/Structure
Cutin and Epicuticular Wax Constituents of Leaf Surface	
Hydroxy fatty acid	$\text{HOCH}_2(\text{CH}_2)_{14}\text{COOH}$
Hydroxy fatty acid	$\text{CH}_3(\text{CH}_2)_8\text{HOCH}(\text{CH}_2)_5\text{COOH}$
Straight-chain alkane	$\text{CH}_3(\text{CH}_2)_{27}\text{CH}_3$
Straight-chain alkane	$\text{CH}_3(\text{CH}_2)_{29}\text{CH}_3$
Fatty acid ester	$\text{CH}_3(\text{CH}_2)_{22}\text{COO}(\text{CH}_2)_{25}\text{CH}_3$
Long-chain fatty acid	$\text{CH}_3(\text{CH}_2)_{22}\text{COOH}$
Long-chain alcohol	$\text{CH}_3(\text{CH}_2)_{24}\text{CH}_2\text{OH}$
Superglue Ingredients	
Cyanoacrylate	$\text{CH}_2\text{C}(\text{CN})\text{COOCH}_3$
Hydroquinone	$\text{HO-C}_6\text{H}_4\text{-OH}$
AuNP Capping/Stabilizing Agent	
Citrate	$\text{OOCCH}_2\text{C}(\text{OH})(\text{CH}_2\text{COO})\text{COO}^{-3}$
Surfactant	
Triton X-100*	$\text{CH}_3\text{C}(\text{CH}_3)(\text{CH}_3)\text{CH}_2\text{C}(\text{CH}_3)(\text{CH}_3)\text{C}_6\text{H}_4(\text{OCH}_2\text{CH}_2)_n\text{OH}$
Shellac Constituents	
Aleuritic acid	
Jalaric acid-A	

* n = 9-10

Table 5.2 shows a list of primary constituents of cutin and epicuticular wax on the surface of a leaf, the ingredients of superglue used (cyanoacrylate and hydroquinone), the citrate capping agent, and the Triton X-100 surfactant. Sharma *et al.* reported that shellac contains aleuritic acid ($\text{C}_{16}\text{H}_{32}\text{O}_5$) and jalaric acid-A ($\text{C}_{15}\text{H}_{20}\text{O}_5$) as its primary building blocks. These are connected by lactide and ester linkages.³¹ Esterification between the alcohol of citrate and the carboxylic acid group in the fatty acids could bind the AuNPs to the leaf surface. Shellac has an alcohol group capable of reacting with the fatty acids as well as carboxylic acid group that could react with the alcohols. Esterification between carboxylic acid and an alcohol functional group within the shellac or citrate to yield a covalent bond is unlikely to occur, however, in the absence of an acid catalyst.

Networks of hydrogen and van der Waals bonding are likely to facilitate adherence of AuNPs to the surface of the leaf mediated by citrate, Triton X-100, and Shellac. Fatty acids of leaf surfaces consist of long straight-chain, hydrophobic carbons terminated by a weak acid carboxylic group. Triton X-100 has hydrophobic and poly(ethylene glycol) arms; the latter has a weak base character. Citrate has one weak hydroxyl base and three weak carboxyl acids. Basic hydroxyl groups on Triton X-100 or citrate could accept acidic hydrogens donated by carboxylic ($-\text{COOH}$) fatty acid group due to their relative electro-positivity and -negativity, respectively. Acidic carboxyl citrate groups could interact with the basic Triton poly(ethylene glycol) arm. Shellac has eight hydrogen-donating $-\text{COOH}$ groups and eleven hydrogen accepting $-\text{OH}$ groups that could facilitate hydrogen bonding to leaf-surface fatty acids and alcohols as well as citrate. Furthermore, van der Waals interactions are possible between the hydrophobic Triton X-100 arm and fatty acid chains.

5.3.4 AuNPs Transfer to *Apocynum cannabinum* Leaf Surface

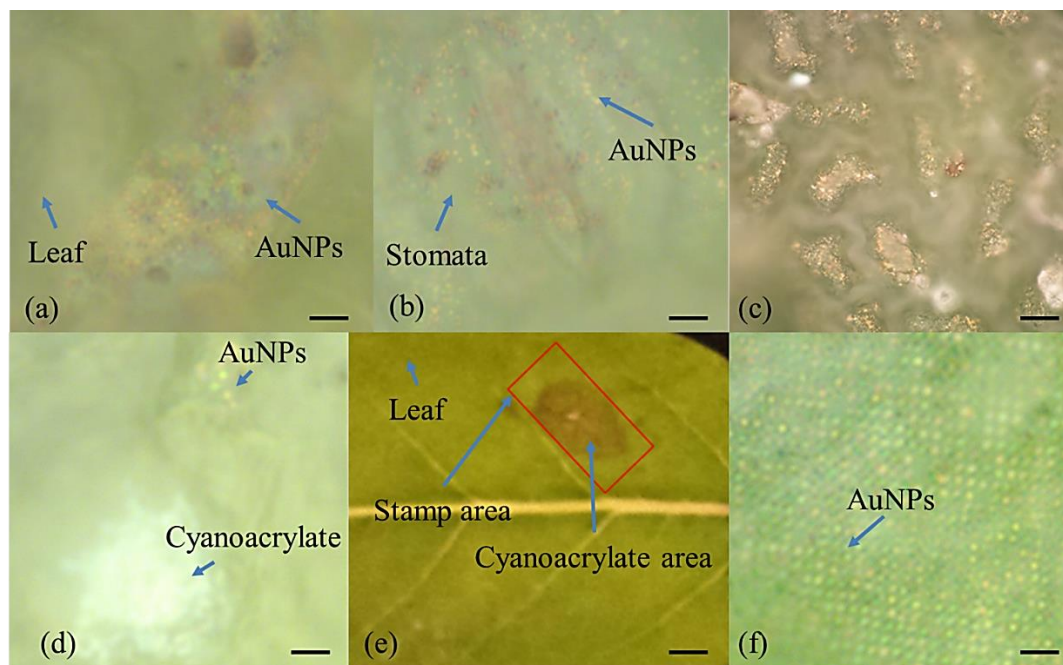


Figure 5.3 AuNPs transferred onto the surfaces of an *Apocynum cannabinum* leaf via (1) laser induction without cyanoacrylate (a-c, scale bars: 3, 3, and 100 μm , respectively) and with cyanoacrylate (d-e, scale bars: 3 μm and 2.5 mm, respectively); and (2) resinous adhesion (f, scale bar: 3 μm). Panel (b) shows sparsely ordered AuNPs on and within the stomata; (d) shows a small area of ordered AuNPs next to a cyanoacrylate cluster; and (e) shows the discoloration of the leaf after the cyanoacrylate-assisted laser induction transfer.

As shown in Figure 5.1, a 50 mW laser irradiated a PDMS film containing AuNPs arrayed in cavities that had been inverted onto an ethanol droplet on a silica-lime microscope slide for 10 min. In comparison with Bagheri *et al.* who used a femtosecond pulsed laser to selectively etch Au coat from a calcium difluoride CaF_2 substrate at high vacuum,²⁶ the present method used a continuous low-power laser at ambient conditions to displace AuNP from one surface to another. Our method transferred approximately 90% of the ordered AuNPs from PDMS cavities to the silica-lime microscope slide without a 20% Triton X-100 post-coat on the PDMS. The resulting extinction spectra and dark-field microscopic images for a PDMS stamp containing 100 nm AuNPs and for the AuNPs transferred onto the microscope slide using laser induction are shown in Figure

5.4. Cerf *et al.* had used ethanol or water to transfer AuNPs from a patterned PDMS stamp to a glass substrate, but in an oven at 100 °C, rather than with a laser,²⁸ which was not feasible to use with plants. We subsequently applied laser induction to transfer AuNP onto both adaxial and abaxial surfaces of a leaf. Initially no transfer occurred from the stamp to the leaf surface (in the absence of a Triton X-100 post-coat, addition of ethanol, or irradiation of the stamp with a laser). So a 20% Triton X-100 post-coat was applied to the stamp before transfer. This resulted in small areas of ordered transfer as shown in Figure 5.3(a-b).

Figure 5.3(b) shows a small area of semi-ordered AuNPs in and around stomata of an *Apocynum cannabinum* leaf. The areas, like those in Figure 5.3(a), varied in size but were no larger than 15 x 15 μm^2 . This appeared due to the uneven topography of the leaf surface which resulted in variable contact between the surface of the leaf and the surface of the PDMS stamp. Consequently, small weights (< 10 g) were added to the top of the PDMS stamp to improve contact with the leaf. This minor modification yielded significant observable transfer of AuNPs conformal to the leaf surface. The configuration of transferred particles, however, appeared disordered. Fidelity of transferring ordered AuNP was low. Successive experiments gave results like that in Figure 5.1(c), with $\geq 85\%$ transfer of AuNPs from the PDMS stamps to the leaf in conformal but unordered fashion across most of the leaf surface in contact with the PDMS.

Cyanoacrylate was observed to improve the transfer of AuNPs from the PDMS stamp to glass slides in terms of percentage of AuNP transferred and the degree of ordering retained upon transfer. Cyanoacrylate was therefore added to the PDMS stamp surface during the 20% Triton X-100 post-coat. The stamp was then transferred to a leaf using the laser induction transfer method. Transferred AuNP were characterized immediately afterward using an optical microscope (Nikon Instruments, Eclipse LV100 D-U). See Figure 5.3(d). In comparison with Chen *et al.* who ink-

patterned fluorine-doped tin oxide (FTO) coated glass, electroplated nickel onto the FTO, then lifted off the structured nickel microsupercapacitors with an adhesive Kapton polyimide film,²⁹ the present work transferred nano- rather than micro-scale structures without using electricity, a chemical bath, or leaving a residual polymer backing.

During microscopic characterization, the area containing the ordered transferred AuNPs began to discolor and stomata on the abaxial leaf surface were observed to close rapidly. After removing the leaf from under the microscope objective, it was visually apparent that the area where the cyanoacrylate had been in contact with the leaf was discolored (see Figure 5.3(e)). While the ordering was maintained as desired, the leaf discoloration indicated an undesirable stress response of the leaf. The dark brown area shown in Figure 5.3(e) shows the area of the leaf that discolored following contact with the cyanoacrylate (bluish white spot in Figure 5.3(d)).

After observing that laser induction with cyanoacrylate yielded high-fidelity transfer but deleteriously affected the leaf, a similar approach was sought to maintain high-fidelity AuNP ordering while preserving leaf viability. The ability of cyanoacrylate to maintain fidelity of the array during transfer suggested use of another optically transparent but biocompatible adhesive. Shellac was selected based on experience preserving leaves with a thin Shellac coat. Its biochemistry suggested it would not adhere to the PDMS. A thin coat of Shellac on a blank PDMS stamp with an ordered cavity array successfully transferred the square cavity pattern to a silica-lime glass coverslip. A thin coat of Shellac on a stamp containing AuNPs ordered in cavities successfully transferred them to a glass coverslip. The extinction spectra and dark-field microscopic images for both the pure ordered Shellac on the glass coverslip and the glass coverslip containing ordered AuNPs transferred via resinous adhesion are shown in Figure 5.4. Use of resinous adhesion process was then adapted to transfer AuNPs ordered in cavities of PDMS to the

abaxial surface of an *Apocynum cannabinum* leaf. The result is in Figure 5.3(f). AuNP ordering was preserved across areas up to 2 mm x 2 mm at high fidelity and no discoloration of the leaf surface was observed.

Previous adhesive approaches to transfer ordered nanostructures to a biologic surface left a residual polymer backing for adhesive at the nanostructure-surface interface. Lee *et al.* used solvent-free aerodynamic focusing and NP excitation to pattern barium titanate (BaTiO₃) and silver (Ag) NP on flexible substrates via cyclic excitation and purging for use in sensing and microelectronics.²³ Ketelsen *et al.* transferred cross-linked gold (Au) nanoparticles (NP) (4 and 7 nm diameter) films onto PDMS sheets equipped with electrodes that were taped on skin above the radial artery to record diagnostic pulse waves with the resultant strain gauge.¹⁰ Wang *et al.* fabricated rapid-response, flexible photodetectors with an ultrashort decay time by depositing cadmium sulfide (CdS) nanowires on poly(3,4-ethylenedioxythiophene) polystyrene sulfonate (PEDOT:PSS) conductive polymer layer with an adhesive backing.¹⁶ Effects of residual polymer backing on the function of adjacent cells and the capital demands of such methods limits their use to monitor activity at plant surfaces, e.g., photosynthesis, in greenhouses or plots.

AuNPs are resistive to chemical oxidation resulting in improved biocompatibility and when irradiated with resonant light, AuNPs absorb and scatter light centered at the resonant frequency of the incident light, which is known as LSPR.^{39,40} This LSPR can be tuned by varying the diameter of the AuNP or the shape, e.g. nanorods instead of nanospheres. When these nanorods or nanospheres are arranged into an ordered structure, the incident light is scattered to adjacent particles in the lattice, producing a second optical feature known as SLR (also called coupled lattice resonance or Fano resonance).^{2,41} This SLR feature can be tuned by varying the spacing between adjacent AuNPs, AuNP diameter, number of AuNPs per lattice point, and by the RI of the substrate

material.^{42,43} Figure 5.4 shows a small sample of the range of tunability of these nanoparticle arrays with respect to the RI for the various transfer processes discussed in this work. Utilization of AuNP arrays as sensors offers readily tunable opportunities compared to other nanostructure sensors that have fixed designs and functions as well as offer a range of tunable options depending on the resonant light wavelength, optical response of chemical desired to be detected, and a highly sensitive detection potential based on the spacing between AuNPs. Photosynthetic properties of the plants can be determined by measuring the rate of opening and closing of the stomata, which can be measured in real-time with an AuNP array through observing the spectral response of an AuNP array placed on the stomata of the plant. The spacing between AuNPs will increase or decrease when the stomata opens or closes, which will change the spectral response of the SLR feature. Matricardi *et al.* showed that as the spacing between clusters of AuNPs increased from 400 to 1600 nm, the SLR feature red shifted into the infrared (IR) region of the spectrum.⁴³

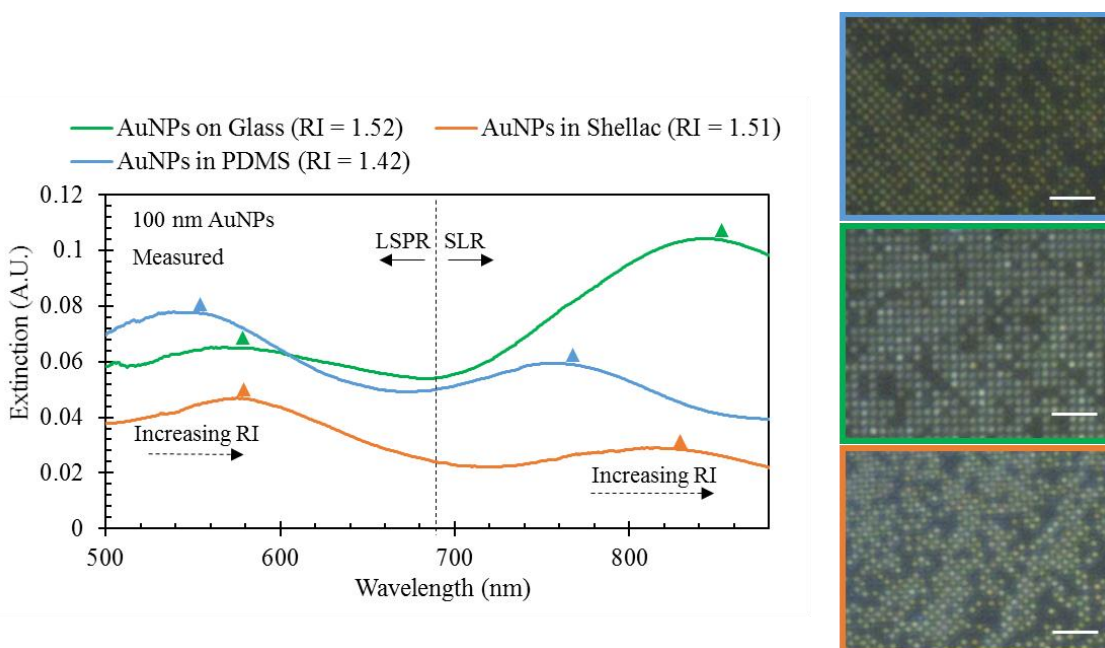


Figure 5.4 Spectral characterization of ordered arrays in PDMS (blue line), transferred on glass with laser (green line), transferred on glass with Shellac (orange line), and ordered Shellac transferred on glass (gray line). 100x dark-field microscope images corresponding to the spectra are shown to the right of the plot (scale bar: 3 μm).

The present work showed conditions under which laser induction and resinous adhesion would transfer AuNPs from a PDMS film onto an adjacent leaf and allow removal of the PDMS substrate onto which the AuNPs had been initially ordered by evaporative self-assembly. Transfer was facilitated hydrogen bonding and van der Waals interactions between Triton X-100 and shellac ingredients and the leaf surface. Triton X-100 and shellac have been used extensively in biological applications with minimal reported consequences. Effects of these components on the functionality of adjacent live plant tissue is under evaluation. Reproducible, field-feasible laser induction and resinous adhesion to transfer self-assembled ordered NPs to the surface of a leaf offer potential for biocompatible, non-invasive, real-time monitoring via the surface lattice resonance feature of plant photosynthesis, nutrient intake, resilience to stress, and response to interventions across micron to millimeter scales.

5.4. Conclusions

Two novel NP printing methods have been examined to for biocompatible transfer of self-assembled, ordered arrays of AuNPs onto the surface of an *Apocynum cannabinum* leaf: (1) laser induction and (2) resinous adhesion. Laser induction without cyanoacrylate transferred NPs to the leaf surface in a largely conformal fashion, yielding up to 15 μm x 15 μm areas of ordered AuNPs. Laser induction with cyanoacrylate transferred ordered NP across areas up to 50 μm x 50 μm . Leaf surface contacted by cyanoacrylate, however, discolored within 20 min post-transfer. Resinous adhesion reproducibly transferred ordered AuNPs across areas up to 2 mm x 2 mm without observable discoloration. Each method offers a tape-free, feasible, way to transfer ordered AuNPs from a substrate onto the surface of a leaf. Resinous adhesion additionally provides capital-free,

straightforward transfer of ordered AuNPs onto biological surfaces in a greenhouse or field environment.

5.5 Author Information

AUTHOR CONTRIBUTIONS

K. Berry drafted text and figures, developed the resinous adhesion transfer method, and fabricated ordered arrays for transfer. M. Dopp performed laser induction transfer experiments with and without cyanoacrylate. D.K. Roper originated the concept, derived the approach, directed the work, and revised and finalized the text.

Notes

The authors declare no competing financial interest

5.6 Acknowledgements

This research work was supported by the Center for Advanced Surface Engineering (CASE), under the National Science Foundation (NSF) Grant No. OIA-1457888 and the Arkansas EPSCoR Program. The authors would like to acknowledge Megan Lanier for the fabrication of the bare PDMS stamps via soft lithography used for making ordered arrays for the transfer processes discussed in this work.

5.7 References

- (1) Roper, D. K.; Ahn, W.; Taylor, B.; D'Asen, Y. Enhanced Spectral Sensing by Electromagnetic Coupling with Localized Surface Plasmons on Subwavelength Structures. *IEEE Sens. J.* **2010**, *10* (3), 531–540.
- (2) Blake, P.; Obermann, J.; Harbin, B.; Roper, D. K. Enhanced Nanoparticle Response from Coupled Dipole Excitation for Plasmon Sensors. *IEEE Sens. J.* **2011**, *11* (12), 3332–3340. <https://doi.org/10.1109/JSEN.2011.2158417>.
- (3) Auguie, B.; Bendaña, X. M.; Barnes, W. L.; García De Abajo, F. J. Diffractive Arrays of Gold Nanoparticles near an Interface: Critical Role of the Substrate. *Phys. Rev. B - Condens. Matter Mater. Phys.* **2010**, *82*, 155447. <https://doi.org/10.1103/PhysRevB.82.155447>.
- (4) Blake, P.; Kühne, S.; Forcherio, G. T.; Roper, D. K. Diffraction in Nanoparticle Lattices Increases Sensitivity of Localized Surface Plasmon Resonance to Refractive Index Changes. *J. Nanophotonics* **2014**, *8* (1), 083084. <https://doi.org/10.1117/1.JNP.8.083084>.
- (5) DeJarnette, D.; Jang, G. G.; Blake, P.; Roper, D. K. Polarization Angle Affects Energy of Plasmonic Features in Fano Resonant Regular Lattices. *J. Opt.* **2014**, *16* (10), 105006. <https://doi.org/10.1088/2040-8978/16/10/105006>.
- (6) Fano, U. Effects of Configuration Interaction on Intensities and Phase Shifts. *Phys. Rev.* **1961**, *124* (6), 1866–1878. <https://doi.org/10.1103/PhysRev.124.1866>.
- (7) Flidj, N.; Laurent, G.; Aubard, J.; Lvi, G.; Hohenau, A.; Krenn, J. R.; Aussenegg, F. R. Grating-Induced Plasmon Mode in Gold Nanoparticle Arrays. *J. Chem. Phys.* **2005**, *123* (22), 221103. <https://doi.org/10.1063/1.2140699>.
- (8) Forcherio, G. T.; Blake, P.; DeJarnette, D.; Roper, D. K. Nanoring Structure, Spacing, and Local Dielectric Sensitivity for Plasmonic Resonances in Fano Resonant Square Lattices. *Opt. Express* **2014**, *22* (15), 17791. <https://doi.org/10.1364/OE.22.017791>.
- (9) Andrich, P.; Li, J.; Liu, X.; Heremans, F. J.; Nealey, P. F.; Awschalom, D. D. Microscale-Resolution Thermal Mapping Using a Flexible Platform of Patterned Quantum Sensors. *Nano Lett.* **2018**, *18* (8), 4684–4690. <https://doi.org/10.1021/acs.nanolett.8b00895>.
- (10) Ketelsen, B.; Yesilmen, M.; Schlicke, H.; Noei, H.; Su, C.-H.; Liao, Y.-C.; Vossmeier, T. Fabrication of Strain Gauges via Contact Printing: A Simple Route to Healthcare Sensors Based on Cross-Linked Gold Nanoparticles. *ACS Appl. Mater. Interfaces* **2018**, *10*, 37374–37385. <https://doi.org/10.1021/acsami.8b12057>.
- (11) Mcalpine, M. C.; Ahmad, H.; Wang, D.; Heath, J. R. Highly Ordered Nanowire Arrays on Plastic Substrates for Ultrasensitive Flexible Chemical Sensors. *Nat. Mater.* **2007**, *6* (5), 379–384. <https://doi.org/10.1038/nmat1891>.

- (12) Oren, S.; Ceylan, H.; Schnable, P. S.; Dong, L. High-Resolution Patterning and Transferring of Graphene-Based Nanomaterials onto Tape toward Roll-to-Roll Production of Tape-Based Wearable Sensors. *Adv. Mater. Technol.* **2017**, *2* (12), 1–14. <https://doi.org/10.1002/admt.201700223>.
- (13) Shi, Y.; Manco, M.; Moyal, D.; Huppert, G.; Araki, H.; Banks, A.; Joshi, H.; McKenzie, R.; Seewald, A.; Griffin, G.; et al. Soft, Stretchable, Epidermal Sensor with Integrated Electronics and Photochemistry for Measuring Personal UV Exposures. *PLoS One* **2018**, *13* (1), 1–15. <https://doi.org/10.1371/journal.pone.0190233>.
- (14) Song, E.; Lee, Y. K.; Li, R.; Li, J.; Jin, X.; Yu, K. J.; Xie, Z.; Fang, H.; Zhong, Y.; Du, H.; et al. Transferred, Ultrathin Oxide Bilayers as Biofluid Barriers for Flexible Electronic Implants. *Adv. Funct. Mater.* **2018**, *28* (12), 1–10. <https://doi.org/10.1002/adfm.201702284>.
- (15) Wang, D.; Zhang, Y.; Lu, X.; Ma, Z.; Xie, C.; Zheng, Z. Chemical Formation of Soft Metal Electrodes for Flexible and Wearable Electronics. *Chem. Soc. Rev.* **2018**, *47* (12), 4611–4641. <https://doi.org/10.1039/c7cs00192d>.
- (16) Wang, L.; Chen, P.; Wang, Y. C.; Liu, G. S.; Liu, C.; Xie, X.; Li, J. Z.; Yang, B. R. Tape-Based Photodetector: Transfer Process and Persistent Photoconductivity. *ACS Appl. Mater. Interfaces* **2018**, *10* (19), 16596–16604. <https://doi.org/10.1021/acsami.8b02233>.
- (17) Wang, Q.; Han, W.; Wang, Y.; Lu, M.; Dong, L. Tape Nanolithography: A Rapid and Simple Method for Fabricating Flexible, Wearable Nanophotonic Devices. *Microsystems Nanoeng.* **2018**, *4* (1), 31. <https://doi.org/10.1038/s41378-018-0031-4>.
- (18) Yu, K. J.; Yan, Z.; Han, M.; Rogers, J. A. Inorganic Semiconducting Materials for Flexible and Stretchable Electronics. *npj Flex. Electron.* **2017**, *1* (1), 4. [https://doi.org/10.1016/S0140-6736\(76\)90345-7](https://doi.org/10.1016/S0140-6736(76)90345-7).
- (19) Zhu, J. X.; Zhou, W. L.; Wang, Z. Q.; Xu, H. Y.; Lin, Y.; Liu, W. Z.; Ma, J. G.; Liu, Y. C. Flexible, Transferable and Conformal Egg Albumen Based Resistive Switching Memory Devices. *RSC Adv.* **2017**, *7* (51), 32114–32119. <https://doi.org/10.1039/c7ra05237e>.
- (20) Bautista, G.; Dreser, C.; Zang, X.; Kern, D. P.; Kauranen, M.; Fleischer, M. Collective Effects in Second-Harmonic Generation from Plasmonic Oligomers. *Nano Lett.* **2018**, *18* (4), 2571–2580. <https://doi.org/10.1021/acs.nanolett.8b00308>.
- (21) Dawood, F.; Wang, J.; Schulze, P. A.; Sheehan, C. J.; Buck, M. R.; Dennis, A. M.; Majumder, S.; Krishnamurthy, S.; Ticknor, M.; Staude, I.; et al. The Role of Liquid Ink Transport in the Direct Placement of Quantum Dot Emitters onto Sub-Micrometer Antennas by Dip-Pen Nanolithography. *Small* **2018**, *14* (31), 1–10. <https://doi.org/10.1002/sml.201801503>.
- (22) Khare, H. S.; Gosvami, N. N.; Lahouij, I.; Milne, Z.; McClimon, J. B.; Carpick, R. W. Nanotribological Printing: A Nanoscale Additive Manufacturing Method. *Nano Lett.* **2018**, *acs.nanolett.8b02505*. <https://doi.org/10.1021/acs.nanolett.8b02505>.

- (23) Lee, G. Y.; Park, J. Il; Kim, C. S.; Yoon, H. S.; Yang, J.; Ahn, S. H. Aerodynamically Focused Nanoparticle (AFN) Printing: Novel Direct Printing Technique of Solvent-Free and Inorganic Nanoparticles. *ACS Appl. Mater. Interfaces* **2014**, *6* (19), 16466–16471. <https://doi.org/10.1021/am504304g>.
- (24) Wu, T.; Lin, Y. W. Surface-Enhanced Raman Scattering Active Gold Nanoparticle/Nanohole Arrays Fabricated through Electron Beam Lithography. *Appl. Surf. Sci.* **2018**, *435*, 1143–1149. <https://doi.org/10.1016/j.apsusc.2017.11.213>.
- (25) Wang, D.; Li, D.; Zhao, M.; Xu, Y.; Wei, Q. Multifunctional Wearable Smart Device Based on Conductive Reduced Graphene Oxide/Polyester Fabric. *Appl. Surf. Sci.* **2018**, *454* (May), 218–226. <https://doi.org/10.1016/j.apsusc.2018.05.127>.
- (26) Bagheri, S.; Weber, K.; Gissibl, T.; Weiss, T.; Neubrech, F.; Giessen, H. Fabrication of Square-Centimeter Plasmonic Nanoantenna Arrays by Femtosecond Direct Laser Writing Lithography: Effects of Collective Excitations on SEIRA Enhancement. *ACS Photonics* **2015**, *2* (6), 779–786. <https://doi.org/10.1021/acsphotonics.5b00141>.
- (27) Braun, A.; Maier, S. A. Versatile Direct Laser Writing Lithography Technique for Surface Enhanced Infrared Spectroscopy Sensors. *ACS Sensors* **2016**, *1* (9), 1155–1162. <https://doi.org/10.1021/acssensors.6b00469>.
- (28) Cerf, A.; Vieu, C. Transfer Printing of Sub-100 Nm Nanoparticles by Soft Lithography with Solvent Mediation. *Colloids Surfaces A Physicochem. Eng. Asp.* **2009**, *342* (1–3), 136–140. <https://doi.org/10.1016/j.colsurfa.2009.04.019>.
- (29) Chen, Y.; Li, X.; Bi, Z.; Li, G.; He, X.; Gao, X. Stamp-Assisted Printing of Nanotextured Electrodes for High-Performance Flexible Planar Micro-Supercapacitors. *Chem. Eng. J.* **2018**, *353* (July), 499–506. <https://doi.org/10.1016/j.cej.2018.07.158>.
- (30) Kang, B. C.; Park, B. S.; Ha, T. J. Highly Sensitive Wearable Glucose Sensor Systems Based on Functionalized Single-Wall Carbon Nanotubes with Glucose Oxidase-Nafion Composites. *Appl. Surf. Sci.* **2019**, *470* (September 2018), 13–18. <https://doi.org/10.1016/j.apsusc.2018.11.101>.
- (31) Sharma, S. K.; Shukla, S. K.; Aid, D. N. V; Centre, D. S.; House, M. Shellac-Structure, Characteristics & Modification. **1983**, 261–271.
- (32) Kudryashov, S.; Pavlov, D.; Kuchmizhak, A.; Syubaev, S.; Gurbatov, S.; Juodkazis, S.; Lapine, M.; Modin, E.; Wang, X.; Vitrik, O. Direct Laser Printing of Tunable IR Resonant Nanoantenna Arrays. *Appl. Surf. Sci.* **2018**, *469* (November 2018), 514–520. <https://doi.org/10.1016/j.apsusc.2018.11.069>.
- (33) Sopena, P.; Fernández-Pradas, J. M.; Serra, P. Laser-Induced Forward Transfer of Low Viscosity Inks. *Appl. Surf. Sci.* **2017**, *418*, 530–535. <https://doi.org/10.1016/j.apsusc.2016.11.179>.

- (34) Sopenña, P.; Serra, P.; Fernández-Pradas, J. M. Transparent and Conductive Silver Nanowires Networks Printed by Laser-Induced Forward Transfer. *Appl. Surf. Sci.* **2019**, *476* (January), 828–833. <https://doi.org/10.1016/j.apsusc.2019.01.179>.
- (35) Ditommaso, A.; Clements, D. R.; Darbyshire, S. J.; Dauer, J. T. The Biology of Canadian Weeds. 143. *Apocynum Cannabinum* L. *Can. J. Plant Sci.* **2009**, *14853*, 977–992.
- (36) Bewick, T. A.; Shilling, D. G.; Querns, R. Evaluation of Epicuticular Wax Removal from Whole Leaves with Chloroform. *Weed Technol.* **1993**, *7*, 706–716.
- (37) J. B. Wyrill, I. I. I.; Burnside, O. C. Absorption, Translocation, and Metabolism of 2,4-D and Glyphosate in Common Milkweed and Hemp Dogbane. *Weed Science*. 1976, pp 557–566. <https://doi.org/10.1017/S0043174500062949>.
- (38) Gao, N.; Huang, P.; Wu, F. Colorimetric Detection of Melamine in Milk Based on Triton X-100 Modified Gold Nanoparticles and Its Paper-Based Application. *Spectrochim. Acta - Part A Mol. Biomol. Spectrosc.* **2018**, *192*, 174–180. <https://doi.org/10.1016/j.saa.2017.11.022>.
- (39) Berry Jr, K. R.; Russell, A. G.; Blake, P. A.; Keith Roper, D. Gold Nanoparticles Reduced *in Situ* and Dispersed in Polymer Thin Films: Optical and Thermal Properties. *Nanotechnology* **2012**, *23* (37), 375703. <https://doi.org/10.1088/0957-4484/23/37/375703>.
- (40) Berry, K. R.; Dunklin, J. R.; Blake, P. A.; Roper, D. K. Thermal Dynamics of Plasmonic Nanoparticle Composites. *J. Phys. Chem. C* **2015**, *119* (19), 10550–10557. <https://doi.org/10.1021/jp512701v>.
- (41) Roper, D. K.; Ahn, W.; Taylor, B.; Asén, A. G. D. Enhanced Spectral Sensing by Electromagnetic Coupling With Localized Surface Plasmons on Subwavelength Structures. *IEEE Sens. J.* **2010**, *10* (3), 531–540. <https://doi.org/10.1109/JSEN.2009.2038451>.
- (42) DeJarnette, D.; Norman, J.; Roper, D. K. Attribution of Fano Resonant Features to Plasmonic Particle Size, Lattice Constant, and Dielectric Wavenumber in Square Nanoparticle Lattices. *Photonics Res.* **2014**. <https://doi.org/10.1364/PRJ.2.000015>.
- (43) Matricardi, C.; Hanske, C.; Garcia-Pomar, J. L.; Langer, J.; Mihi, A.; Liz-Marzán, L. M. Gold Nanoparticle Plasmonic Superlattices as Surface Enhanced Raman Spectroscopy Substrates. *ACS Nano* **2018**. <https://doi.org/10.1021/acsnano.8b04073>.

6. CONCLUSIONS

6.1 Summary

This work advanced several key areas of fabrication, characterization, and analytical modeling of self-assembled nanoantenna in polymer thin films. The analytical approach to estimating the thermal dynamics of AuNPs assembled in random arrangements in colloidal suspensions, deposited on glass, and embedded in polymer thin films outlined in Chapter 2 estimated the thermal dynamics within 30% across a range of geometric parameters, nanoantenna-containing media, and thermal parameters. The thermal dynamics of random dispersions of AuNPs embedded in polymer thin films showed multimodal behavior which was further characterized across a range of variables including film thickness, laser power, NP diameter, respective pixel location, and laser spot size was outlined in Chapter 3. These thermal dynamics showed that the multimodal behavior was dependent primarily on film thickness, pixel location, and laser power. Development of a scalable and reproducible method for fabricating 2D ordered arrays of AuNPs was outlined in Chapter 4 and showed that when the evaporation rate is low, deposition rate is 1.2 $\mu\text{m/s}$, and the AuNP diameter is 150 nm, the array has $\sim 100\%$ density of filled cavities across a $>2\text{ mm} \times 2\text{ mm}$ area and shows distinguishable LSPR and SLR features in the UV-Vis spectra. These arrays were also compared to rsa-CDA simulations and matched within 2% in PDMS (RI = 1.42) and when transferred onto glass (RI = 1.52). The fabrication method developed in Chapter 4 was used to fabricate arrays for transfer onto the surface of a leaf using two different developed transfer techniques (laser induction and resinous adhesion), which are discussed in Chapter 5 showing that the laser induction transfer resulted in $15\ \mu\text{m} \times 15\ \mu\text{m}$ (without cyanoacrylate) to $50\ \mu\text{m} \times 50\ \mu\text{m}$ (with cyanoacrylate) areas of ordered transfer and the resinous adhesion transfer resulted in >2

mm x 2 mm area of ordered transfer. Ordered arrays of AuNPs on the surface of a leaf offers potential advancement for sensing applications for real-time monitoring of vital crop information to increase the avenues of higher crop yield and lower crop loss for increasing the food production to sustain a rising food demand with higher populations.

6.2 Future Work

The utilization of the optical enhancements of self-assembled nanoantenna offer potential for advancements in energy, membrane separation, and food protection and production applications. Materials like those described in Chapters 2-3 have been used for preliminary membrane separation processes for recovering butanol and for water desalination.^{1,2} Transitioning from random arrangements of AuNPs to ordered arrangements as described in Chapter 4 allow for opportunities in food protection and production applications through the development of a biological sensor as discussed in Chapter 5. Coupling the optical properties of these AuNPs with semiconductor materials like tungsten disulfide or molybdenum disulfide have been demonstrated valuable enhancements for catalysis and various other photonic devices.³⁻⁵ Combining these semiconductor materials with ordered arrangements of NPs result in exciton-plasmon coupling, known as plexcitons, allow for engineering light-matter interactions in plasmonic and excitonic systems.⁶

To-date little is known about the thermal dynamics of plexcitons and materials containing plexcitons. Understanding the thermal dynamics of these materials could result in an increase in the viability of these materials being utilized in thermal applications. The optical enhancements observed from these materials show potential for photonic devices, catalytic applications, and various other energy applications. Further development and engineering of these materials offer

opportunities for the fabrication of exotic nanomaterials that have tunable plasmonic and excitonic properties resulting in an increase in viable applications.

In addition to materials containing plexcitons, the utilization of ordered arrangements of AuNPs offer potential for improving food protection through further developments and advances in swab technologies. Currently, polyurethane swabs are used for bacteria collection from surfaces in the food industry for detecting harmful bacteria levels present on the working surfaces. These swabs have remained underdeveloped for decades and the incorporation of plasmonic AuNPs offer opportunities for further advancement of these swab technologies. Work is currently underway to study the mass of water absorption and rate of water evaporation from standard polyurethane swabs that have been doped with surfactant and AuNPs in random and ordered arrangements. Understanding the effects of the surfactant and AuNPs on the water absorption and evaporation in these swabs when exposed to darkness, ambient light conditions, and laser irradiation could provide further insight and offer opportunities for further advancement in swab technologies for food protection. This work is ongoing with collaborators in the Food Science Department at the University of Arkansas.

6.3 References

- (1) Russell, A. Plasmonic Pervaporation via Gold Nanoparticle- Functionalized Nanocomposite Membranes. *Theses Diss.* **2012**, 476, 1–92.
- (2) Dunklin Jeremy. Plasmon-Mediated Energy Conversion in Metal Nanoparticle-Doped Hybrid Nanomaterials. *Theses Diss.* **2017**, 1986, 1–123.
- (3) Dunklin, J. R.; Lafargue, P.; Higgins, T. M.; Forcherio, G. T.; Benamara, M.; McEvoy, N.; Roper, D. K.; Coleman, J. N.; Vaynzof, Y.; Backes, C. Production of Monolayer-Rich Gold-Decorated 2H–WS₂ Nanosheets by Defect Engineering. *npj 2D Mater. Appl.* **2017**, 1 (1), 43. <https://doi.org/10.1038/s41699-017-0045-z>.

- (4) Kim, J.; Byun, S.; Smith, A. J.; Yu, J.; Huang, J. Enhanced Electrocatalytic Properties of Transition-Metal Dichalcogenides Sheets by Spontaneous Gold Nanoparticle Decoration. *J. Phys. Chem. Lett.* **2013**, *4* (8), 1227–1232. <https://doi.org/10.1021/jz400507t>.
- (5) Forcherio, G. T.; Benamara, M.; Roper, D. K. Electron Energy Loss Spectroscopy of Hot Electron Transport between Gold Nanoantennas and Molybdenum Disulfide by Plasmon Excitation. *Adv. Opt. Mater.* **2017**, *5* (3). <https://doi.org/10.1002/adom.201600572>.
- (6) Liu, W.; Wang, Y.; Naylor, C. H.; Lee, B.; Zheng, B.; Liu, G.; Johnson, A. T. C.; Pan, A.; Agarwal, R. Understanding the Different Exciton-Plasmon Coupling Regimes in Two-Dimensional Semiconductors Coupled with Plasmonic Lattices: A Combined Experimental and Unified Equation of Motion Approach. *ACS Photonics* **2018**, *5* (1), 192–204. <https://doi.org/10.1021/acsp Photonics.7b00672>.